ÚSTAV
KONSTRUOVÁNÍ

Vysoké učení technické v Brně
Fakulta strojního inženýrství
Ústav konstruování

Brno University of Technology
Faculty of Mechanical Engineering
Institute of Machine and Industrial Design

PROCESSING OF THE MAGNESIUM ALLOYS BY SELECTIVE LASER MELTING METHOD

Suchý Jan, Ing.
Autor práce
Author

doc. Ing. David Paloušek, Ph.D.
Vedoucí práce
Supervisor

Disertační práce
Dissertation Thesis

Brno 2022

ABSTRAKT

Tématem předložené disertační práce je zpracování hořčíkových slitin technologií selektivního laserového tavení. Práce podrobněji rozpracovává otázku korozní odolnosti takto vyrobeného materiálu, relativní hustoty a mechanických vlastností s důrazem na použití v biomedicínských aplikacích. Hlavním cílem práce je objasnění vlivu procesních a technologických parametrů na korozní rychlost zpracovaného materiálu.

V první fázi práce byla na sériích liniových a objemových vzorků zkoumána relativní hustota vzorků spolu s vnitřní mikrostrukturou a mechanickými vlastnostmi. Druhá fáze se zabývala vlivem mikrostruktury a jakosti povrchu na výslednou korozní rychlost materiálu v simulovaném prostředí lidského těla. Díky tomu se podařilo stanovit korozní rychlost SLM zpracovaného materiálu a určit, jakým způsobem ji lze měnit změnou procesních parametrů. V práci se podařilo opakovaně dosáhnout relativní hustoty materiálu 99.5 % s tvrdostí 85±6 HV, pevností v tlaku 416±40 MPa a tříbodovém ohybu 212±9 MPa, což jsou hodnoty poměrně blízké lidským kostem. Zároveň se podařilo snížit rychlost koroze materiálu o takřka 22 % snížením drsnosti povrchu z původních Ra 57.3 na Ra 34.2. V práci však nebyl zmapován detailní vliv katodických fází během korozního testu.

Uvedená práce podává čtenáři ucelený přehled o problematice 3D tisku hořčíkových slitin spolu s detailním popisem vlivu procesních a technologických parametrů na proces výroby slitiny WE43. Práce definuje korozní vlastnosti 3D tištěného materiálu s relativní hustotou 99.5 % s různými jakostmi povrchu. Výsledky práce posouvají dále poznání v oblasti biodegradabilních implantátů pro využití v medicínském prostředí.

KLÍČOVÁ SLOVA

Selektivní laserové tavení, hořčíkové slitiny, homogenní materiál, mikrostruktura, korozní rychlost

ABSTRACT

The topic of the presented doctoral thesis is the processing of magnesium alloy technologies of selective laser melting. The thesis elaborates in more detail the issue of corrosion resistance of the material produced in this way, relative density, and mechanical properties with emphasis on the use in biomedical applications. The main goal is to clarify the influence of process and technological parameters on the corrosion rate of the processed material.

In the first phase of the work, the relative density of the samples was examined on series of linear and volumetric samples along with the internal microstructure and mechanical properties. The second phase dealt with the influence of microstructure and surface quality on the resulting corrosion rate of the material in the simulated environment of the human body. Thanks to this, it was possible to determine the corrosion rate of the SLM processed material and to determine how it can be changed by setting of the process parameters.

During the research, it was repeatedly achieved a relative density of 99.5% with a hardness of 85 ± 6 HV, compressive strength of 416 ± 40 MPa and three-point bending strength of 212 ± 9 MPa, which are the values relatively close to human bones. At the same time, it was possible to reduce the corrosion rate of the material by almost 22% by reducing the surface roughness from the initial Ra 57.3 to Ra 34.2. However, a detailed influence of cathodic phases during the corrosion test was not tested.

This thesis provides the reader with a comprehensive overview of 3D printing of magnesium alloys along with a detailed description of the influence of process and technological parameters on the WE43 alloy production process. The thesis defines the corrosion properties of 3D printed material with a relative density of 99.5% with different surface qualities. The results further advance the knowledge in the field of biodegradable implants for medical applications.

KEYWORDS

Selective laser melting, Magnesium alloys, Homogeneous material, Microstructure, Corrosion rate

BIBLIOGRAPHIC CITATION

SUCHÝ, Jan. *Processing of magnesium alloys by selective laser melting method.* Brno, 2022, 152 s. PhD thesis. Brno university of technology, Faculty of mechanical engineering, Institute of machine design. Supervisor doc. Ing. David Paloušek, Ph.D.

ACKNOWLEDGEMENT

I wish to express my thanks to my wonderful wife Kateřina for her support and tolerance during the long moments I spent over the work presented. I would also like to thank my family for their support and the opportunity to study the field that fulfils me. Without their support, I would never have made it. My thanks also go to my supervisor doc. Ing. David Paloušek, Ph.D. and specialists doc. Ing. Daniel Koutný, Ph.D. and doc. Ing. Libor Pantelejev, Ph.D. for their valuable advice, optimism and directing my efforts whenever I stuck in place. I would also like to thank my colleagues from the author's team, especially Ing. Lenka Klakurková, Ph.D. for expert advice, excellent cooperation, and her inspiring nature. Many thanks also to Mgr. Zuzana Svobodová for help with professional translation of the work. Last but not least, I would like to thank Ing. Martin Malý for help with assembling an external filtration system used in this work and Ing. Ondřej Vaverka for witty afternoon talks on all-embracing topics over a cup of good tea.

AUTHORS'S DECLARATION OF ORIGINALITY OF DOCTORAL THESIS

I, the undersigned hereby declare that I am the sole author of this doctoral thesis under the supervision of doc. Ing. David Paloušek, Ph.D. At the same time, I declare that all sources of image and text information from which I have drawn are duly cited in the list of sources used.

....

Author signature

OBSAH

1 INTRODUCTION 13

2 STATE OF THE ART 16

2.1 Selective laser melting technology 16

2.2 Processing of magnesium and its alloys by SLM method 19

2.2.1 Processing of pure magnesium by SLM method 19

2.2.2 Processing of Mg-Al (AZ) based alloys by SLM method 20

2.2.3 Processing of Mg-Y-Nd (WE) alloys by SLM method 24

2.3 Oxidation of magnesium and its alloys 28

2.3.1 Principle and behaviour of oxidation at standard temperatures 28

2.3.2 Oxidation of magnesium alloys at elevated temperatures 30

2.3.3 Inert atmosphere when printing magnesium and its alloys 31

2.4 Corrosion behaviour of WE43 alloy processed by SLM 32

3 ANALYSIS OF THE CURRENT STATE OF THE ART 35

3.1 Evaluation of oxidation of magnesium and its alloys 35

3.2 3D printing of magnesium and its alloys 37

3.3 Definition of main problems 41

4 GOALS OF DOCTORAL THESIS 43

4.1 Scientific questions 43

4.2 Hypotheses 44

4.3 Structure of doctoral thesis 44

5 MATERIALS AND METHODS 47

5.1 Achieving the reqired mechanical properties of 3D printed material WE43 47

5.2 Corrosion behaviour of material in simulated human body environment 49

5.2.1 Powder analysis 51

5.2.2 Sample printing 52

5.2.3 Geometry analysis of weld depositions and thin walls 53

5.2.4 Measurement of surface roughness 54

5.2.5 Analysis of chemical composition and microstructural description 55

5.2.6 Hardness measurement 56

5.2.7 Analysis of porosity 56

5.2.8 Determination of compressive and flexural strength 57
5.2.9 Immersion test 57

6 RESULTS 59

6.1 Achieving the required mechanical properties of 3D printed material WE43 59
6.1.1 Analysis of the shape and continuity of weld deposition tracks 59
6.1.2 Influence of parameters on chemical composition and microhardness of weld depositions 62
6.1.3 Comparison of weld deposition tracks and thin walls 63
6.1.4 Printing of the volumetric samples 64
6.1.5 Internal structure of 3D printed material and its mechanical properties 66
6.1.6 Modification of the inert atmosphere circuit 70
6.1.7 Optimization of printing strategy 72

6.2 Corrosion behaviour of material in simulated human body environment 75
6.2.1 Microstructural analysis 75
6.2.2 Measurement of surface roughness of thin walls 77
6.2.3 Immersion test 78

7 DISCUSSION 81

7.1 Achieving the required mechanical properties of 3D printed material WE43 81
7.1.1 Analysis of the shape and continuity of weld deposition tracks 81
7.1.2 Chemical composition and microhardness of weld depositions 82
7.1.3 Defects in volumetric samples 83
7.1.4 Reducting the amount of vapour 84
7.1.5 Modification of the inert atmosphere circuit 85
7.1.6 Optimization of printing strategy 87

7.2 Corrosion behaviour of the material in the simulated human body environment 88
7.2.1 Microstructural analysis 88
7.2.2 Surface quality analysis 89
7.2.3 Immersion test in HBSS 90

8 CONCLUSION 91

9 BIBLIOGRAPHY 99

10 LIST OF FIGURES AND TABLES 107

11 LIST OF SYMBOLS AND UNITS 111

12 ANNEXES 112

1 INTRODUCTION

Along with the development of additive technologies, more and more scientific efforts are focused on the processing of more demanding materials such as low-melting non-ferrous metals. This opens up scientific opportunities in application areas such as biomechanics, genetic engineering or medicine. These areas are inextricably linked to artificial implants in the human body, the purpose of which is to enable the patient to lead an almost full life, even with the loss of key organs or to help in the treatment of extensive injuries. One such injury is an extensive bone defect that current orthopaedic surgery faces [1]. In 2017, 2.7 million extensive bone defects were recorded according to the statistic from the six key-European countries by patients over the age of 50. Their treatment cost countries 37.5 billion euros in summary (reoperation, medical expenses, sick days, etc.). In addition, the prediction for 2030 counts with the next increase of 30 % due to the increased average age of humankind. The use of biodegradable implants seems to be the best solution to deal with this problem due to removing the reoperation and shorter the sick days. Biodegradable implants are also an area that has attracted humankind for more than a century and has had the considerable potential [2].

From among the biodegradable materials, magnesium and its alloys appear to be the most suitable for bone replacements. Magnesium is one of the basic building blocks of the human body and can be found naturally in human bones [3–5]. Its corrosion produces a non-toxic oxide that is excreted in the urine [6]. In addition, due to its function in the bones, it contributes to stimulating the growth of new bone tissue [7–10]. This, in conjunction with its elastic modulus, which is closer to the bone tissue more than other biodegradable materials (bone: 3–20 GPa, Mg: 41–45 GPa, Ti alloys: 110–117 GPa, stainless steels: 189–205 GPa) [6], leads to a delayed or complete prevention of implant reoperation.

However, current procedures applied to non-healing bone defects face a number of problems such as immune system rejection, insufficient space at the defect site, mechanically different properties of bones and implants, reoperations, etc. To solve these problems, bone tissue treatment is increasingly being considered directly at the defect site. However, such a treatment requires implants that take into account the extent of the injury as well as the different body structure of the patient. Applying the implant can also cause a problem with the supply of nutrients to the injured area. This can be solved by using lattice structure, which can be close in shape to the structure of the bone tissue.

The structure of human bone tissue is hierarchical. It contains three cavities and each of them has a different size in the order of tens of micrometres [11]. Each of them has a defined role in bone regeneration and mechanical integrity [12]. They also allow for nutrients to flow to the injured tissue [13]. Hierarchical bone pores can be replaced by a precisely defined lattice structure. The lattice structure can support the injured tissue at the defect site and at the same time serve as a support for cell growth at the injured site. In this way, it is possible to solve problems with the built-up area at the site of injury, cell migration, nutrient and waste exchange [14, 15]. This largely minimizes the production and transmission of pathogens [16]. By designing the shape and dimensions of the structure, the elastic modulus of the material near the bone tissue can be changed, which makes it possible to eliminate the stress effects on the regenerated bone [17]. The structures are also used in other fields, mainly due to weight reduction, its absorption and acoustic properties [18, 19]. Fibre splicing, gas foaming or lyophilisation technology can be used to produce lattice structures. However, these methods provide a limited ability to control the morphology of the it [20–22], which is crucial for custom implant production. In contrast, the use of additive technologies provides the geometry that is controlled by CAD data. The "layer by layer" production method makes it possible to produce parts of complex shapes which cannot be produced by conventional methods [23].

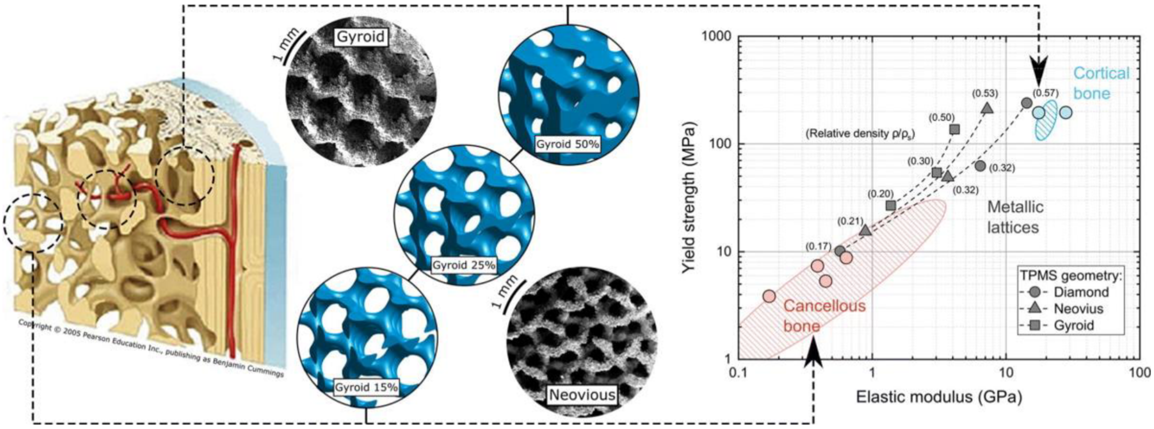

Fig 1.1 Comparison of basic mechanical properties of bone implants designed by additive manufacturing with the structure of real bones.

Selective laser melting (SLM) appears to be a suitable additive method for the processing of magnesium and its alloys. This method can process a wide range of materials such as Al, Ti, CoCr, Au, Cu, Ni [24, 25]. However, the use of the SLM method requires a specific production process setting for a specific application and material. The processability of magnesium and its alloys using SLM has not yet been systematically described, although a number of publications are beginning to deal intensively with this topic. The results so far show that the material can be additively processed, although it is very difficult. The reason for difficult processing is mainly the low melting point (650°C) and evaporation (1091°C) together with high reflectivity (up to 98%). These properties, together with rapid corrosion, are the main reasons for the difficult processability of magnesium and its alloys using 3D printing.

One of the biggest problems faced by parts made of magnesium alloys using the SLM method is low corrosion resistance. This can be influenced, among others, by the quality of the surface. The surface quality can be partly influenced by setting the process parameters. However, this issue has not yet been addressed in 3D-printed magnesium alloys. Therefore, this thesis will focus on describing the influence of process parameters on the surface quality of magnesium alloys and its influence on the corrosion resistance of the printed material.

2 STATE OF THE ART

2.1 Selective laser melting technology

The SLM technology patent was first filed in 1997. This technology was developed in collaboration with Dr. W. Meiners, K. Wissenbach, G. Andres of Franhofer ILT, and Dr. M. Fockele and Dr. D. Schwarze of F&S Stereolithographietechnik GmbH [24].

As an input material, this technology uses atomized metal powder, the fraction of which most often ranges in the order of 10–100 μm. The powder is produced by the melt spatter with a nozzle into an enclosed space, into which inert gases are fed at high speed (Fig 2.1). These are most often Ar, N_2, or He. The spatter droplets of metal naturally try to take on the least energy-intensive spherical shape. Due to the rapid cooling of the metal spatter, asymmetrical shapes and adhered satellites may occur in some droplets.

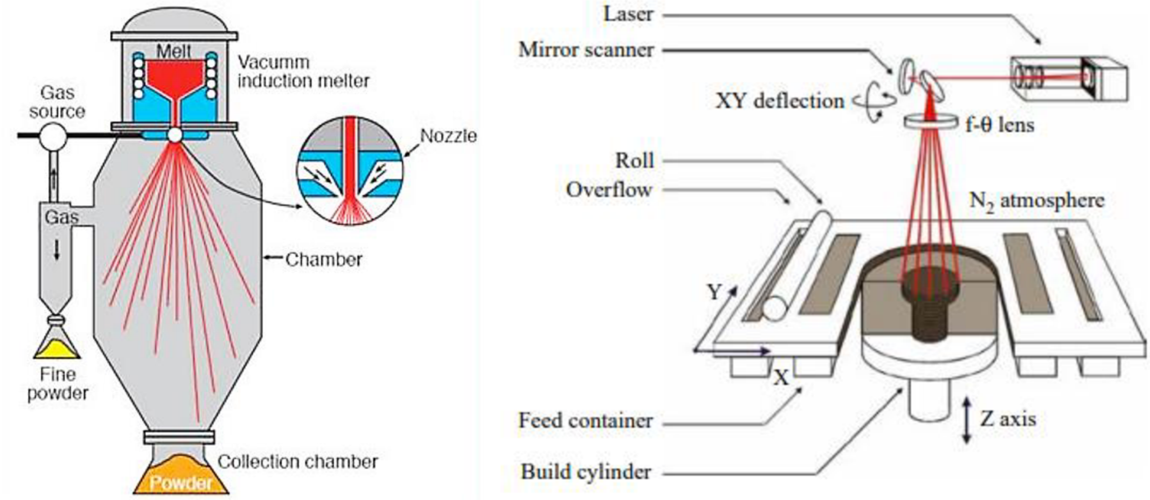

(a) (b)

Fig 2.1 (a) Metal powder atomization scheme [26] and (b) SLM method scheme [27].

The SLM method consists in depositing the layers of metal powder and joining them using thermal energy provided by a laser (Fig 2.1). The geometry of the printed part is controlled by CAD data, from which the laser paths for the individual layers are subsequently created. The printing itself begins with depositing the first layer on a metal plate, which should match the chemical composition of the printed material. The desired shape is hatched on the laser and the powder is welded to the build plate. The build plate with the resulting part decreases by the height of one layer, which is then deposited. By re-hatching with the laser, the molten powder is welded to the previous layer. This process is repeated until the required geometry is reached. The SLM technology is suitable for a wide range of materials such as Al, Cu, Ti, Au, Ni, Zn, Mg etc. [24, 28] and, thanks to the principle of production, it is possible to produce geometry unattainable by conventional methods [23].

The quality of the resulting parts can be controlled by a number of parameters (estimated at several tens). These may include, for example, the quality of the input material, the purity and composition of the inert atmosphere, preheating of the build plate, overpressure in the production chamber, etc. A relative density of manufactured parts close to 100 % can be achieved by a suitable combination of process parameters [29]. The parameters that have the greatest impact on the production process include laser power, scanning speed, hatch distance and the thickness of the deposited layer. These main parameters are expressed in the energy equation (2.1).

$$E = \frac{Lp}{Ls \cdot Hd \cdot Lt}, \qquad (2.1)$$

Where E is the energy density [$J \cdot mm^{-3}$], Lp is the laser power [W], Ls is the laser scanning speed [$mm \cdot s^{-1}$], Hd is the hatch distance [mm] and Lt is the layer thickness [mm].

The calculated energy density can be effectively used to find the areas where the printing process works permanently [30]. Subsequently, suitable ratios between the main parameters are set in the selected process area. Energy density can be expressed as linear and volumetric density. Linear energy is used for the initial considerations dealing with the weld deposition test. It serves as a primary indicator that can be used to evaluate the results of the weld deposition test. However, this value does not provide information on the production behaviour of the volumetric sample [31]. Thus, it may happen that when the same energy but different process parameters are reached, the result will be different. The energy equation associating the process parameters does not take into account the effects of other parameters such as build plate preheating or remelting of the layers. At the same time, the use of preheating and remelting can lead to a significant change in the structure of the material even outside the specified range of used energies [32, 33]. For these reasons, the energy density value is mainly used as a comparison criterion.

The parameter that can directly control the amount of input energy coming to the melting site is the laser power. A laser beam with a Gaussian profile is used as standard. By blurring it, it is possible to spread the input energy over a larger area, which can effectively reduce the depth of the weld deposition tracks if too deep. At the same time, the power of the laser has the most fundamental effect on the resulting properties of the manufactured part in comparison with other parameters [34]. The setting of the laser power, its operating mode and other properties depends on the type of laser, the type of 3D printer used and the material being processed.

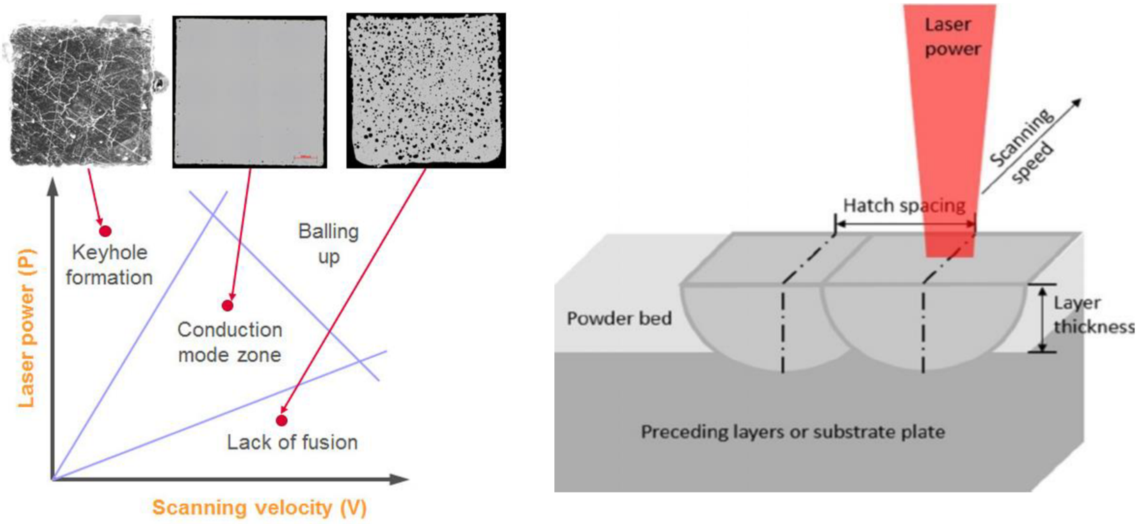

(a) (b)

Fig 2.2 (a) Process window diagram with designation of processable and (b) definition of main process parameters [35].

The choice of scanning speed has a direct effect on the size of the melt pool at the point of impact of the laser beam. The low scanning speed leads to a large accumulation of energy at the point of impact of the beam, which increases the dimensions of the melt pool and its temperature. Since the temperature outside and at the edges of the melt pool is different [36], in this case, the melt may spatter due to unstable conditions in the melt pool [37]. The spatter droplets of melt can sinter the surrounding powder into agglomerations which disrupt the uniformity of the deposited layer and can cause porosity. Low scanning speed can also lead to a balling effect, which reduces the quality of the produced surface.

Along with the laser power, the hatch distance has the greatest effect on the production process. By bringing the weld deposition tracks closer together, they are remelted, which increases the energy densities at the melting site. This ensures stable melting of the powder even with the use of lower laser power. However, a very large hatch overlap significantly increases production time. In addition, high energy density can also lead to the formation of cavities in the material due to gas trapping [38].

The height of the layer is chosen with respect to the powder fraction used. It is most often in the range of 20–100 µm. Although the use of a lower deposited layer lengthens the production time, the benefit is an increase in the relative density of the manufactured part [39]. Increasing the height of the layer also increases the amount of material involved in the melting process. As a result, the formed weld deposition tracks are wider, which must be taken into account when choosing the hatch distances [32].

2.2 Processing of magnesium and its alloys by SLM method

2.2.1 Processing of pure magnesium by SLM method

The first information about attempts to process pure magnesium by the SLM method appeared in the years 2010-2011 [40–42]. The group around Ng assembled its own SLM device with a protective box, where they examined weld deposition tracks made of pure magnesium (Fig 2.3). During the tests, the authors faced a constant increase in oxygen in the process chamber of the machine, which was reflected in the chemical composition of the surface of the weld depositions. Initial tests also showed a high sensitivity of the printing process to the quality of the input powder. Experiments with pulsed and continuous laser modes showed more continuous weld deposition tracks as the laser power increased. However, at the same time, the depth of the weld deposition increased significantly, which would affect a large number of already solidified layers in the case of printing a volumetric part.

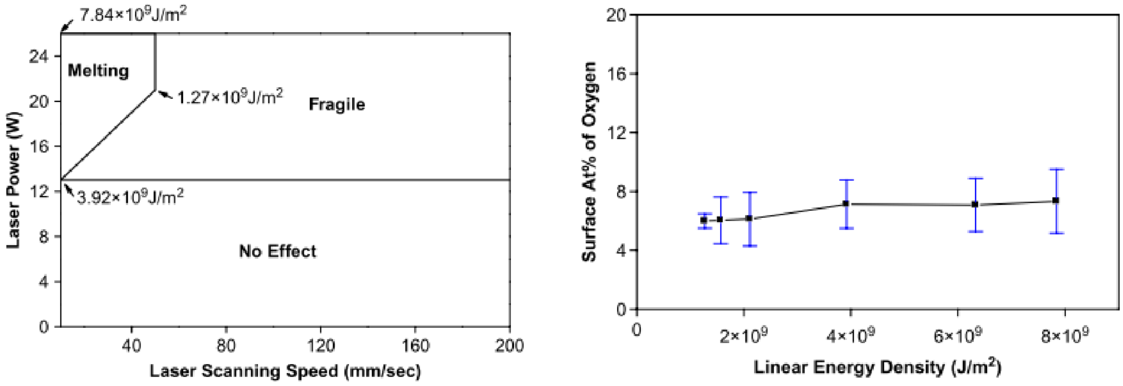

(a) (b)

Fig 2.3 (a) Identification of the minimum amount of energy density for the formation of weld deposits from pure Mg and (b) the effect of energy density on the saturation of the surface of the weld deposit with oxygen [41].

The follow-up test was focused on the validation of the effect of the deposited powder layer and the effect of build plate preheating [32]. By adding of preheating of the build plate, it was possible to reduce the laser power while maintaining the continuous shape of the weld deposition tracks, and thus energy can be supplied to the melting site efficiently from other sources than just from the laser beam. The change in the thickness of the powder layer affected the amount of oxygen found on the surface of the weld depositions. The higher layer thickness reduced the amount of oxygen in the surface layer. The reason for this behaviour was probably a reduction in energy density and thus a reduction in temperature and the number of vapours at the melting site. As a result, the passivation film on the surface did not disrupt so much and oxygen could not diffuse into the material to such an extent.

The next step was a test for the production of volumetric samples, where, based on the findings from previous work, further increase in the laser power was examined (Fig 2.**4**.). Two fractions of magnesium powder were used during these tests. The higher distribution powder (average particle size of 45.32 µm) required a higher laser power than the lower distribution fraction to achieve the same relative sample density. Due to the low density of magnesium powder, the lift of the powder with a lower fraction (average particle size of 25.85 µm) was observed after laser impact. However, the increase in laser power had a negative effect on the reduction in the quality of the surface to which the surrounding powder began to be fused.

(a) (b)

Fig 2.4 Volumetric samples of pure magnesium using powders with a distribution of (a) 26 µm and (b) 43 µm [43].

2.2.2 Processing of Mg-Al (AZ) based alloys by SLM method

The first tests on pure magnesium were quickly followed by a series of tests on selected magnesium alloys. Mg-Al-based alloys were the first, probably due to their industrial use.

The initial tests were focused on the description of the process window diagram, describing the behaviour of the material when printing volumetric parts with different combinations of process parameters [30]. Due to the large scatter in laser power and scanning speed, a relatively wide range of combinations of these parameters was mapped. However, most of the produced samples lacked mechanical integrity. In addition, during the printing of the samples, a large number of process emissions appeared in the production chamber, which blurred the laser beam. Samples designated A, B, C and D appeared to be suitable for further analyses (Fig 2.5).

The microstructure of the material contained pores resembling a bloom. These were probably created by trapping the vaporized gases (Fig 2.6). At the same time, a balling effect was formed on the surface of the samples due to oxidation. The grain size in the material ranged from 10 to 20 µm. It was observed that as the scanning speed increased, the grain size in the material decreased. Intermetallic phases typical of AZ91 alloys ($Mg_{17}Al_{12}$, MgO a Al_2O_3) appeared in the produced samples.

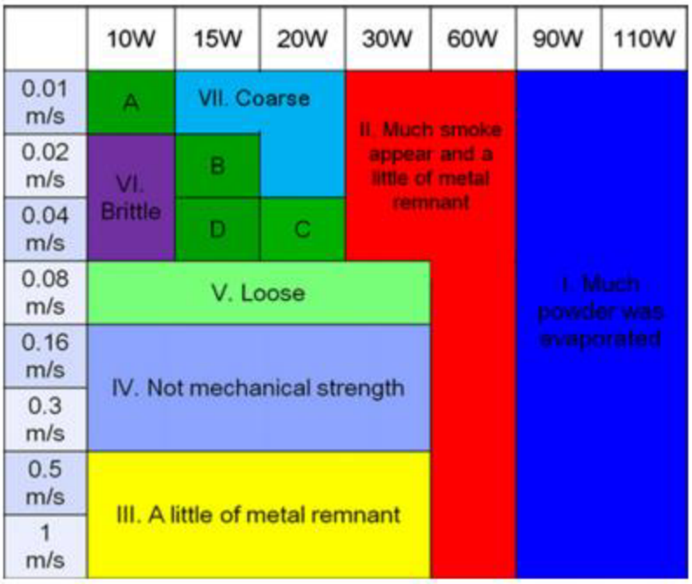

	10W	15W	20W	30W	60W	90W	110W
0.01 m/s	A	VII. Coarse		II. Much smoke appear and a little of metal remnant		I. Much powder was evaporated	
0.02 m/s	VI. Brittle	B					
0.04 m/s		D	C				
0.08 m/s	V. Loose						
0.16 m/s	IV. Not mechanical strength						
0.3 m/s							
0.5 m/s	III. A little of metal remnant						
1 m/s							

Fig 2.5 Process map diagram for printing volumetric samples from Mg-9% Al alloy [30].

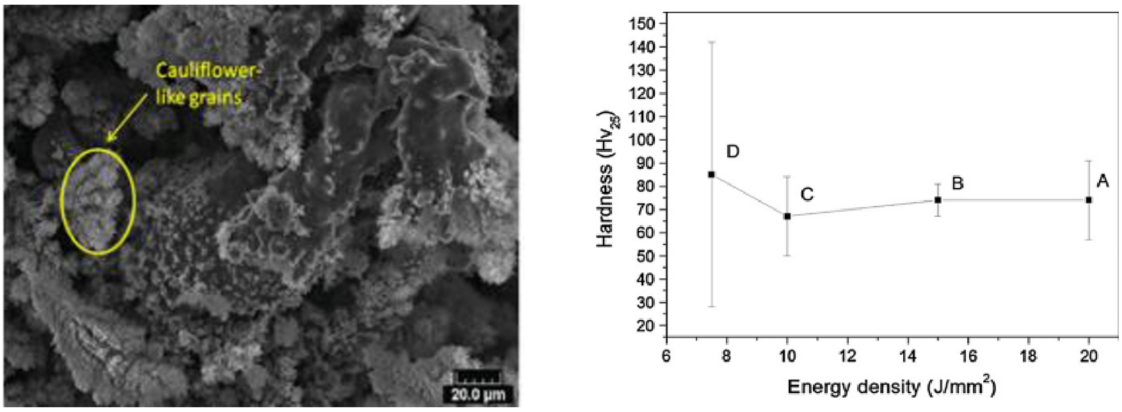

(a) (b)

Fig 2.6 Porous microstructure in material (a) and dependence of sample hardness on energy density (b) [30].

The aim of another test was to describe the behaviour of AZ91D alloy as a function of energy density and gradually increasing hatch distances [44]. To map the behaviour, a process window diagram was created and divided into four areas (Fig 2.7 The first area containing energies higher than 214 J·mm^{-3} was characterized by the occurrence of strong evaporation of the material, which made it impossible to continue the production process. After reducing the energy density to 87–167 J·mm^{-3}, the production process stabilized and the amount of evaporated material decreased. In this area, a sample with a relative density greater than 99.5 % was obtained. Gradually reducing the energy density, a balling effect began to appear during production, which had a negative effect on the stability of the melt pool. Fine grain and the associated increase in hardness compared to conventional material processing methods were detected in the analysed samples. The material also showed the boundaries of the weld deposition tracks and the size of their penetration. It ranged in values even above 300 μm. The low value of porosity in the material was probably caused by multiple remelting of already solidified layers of material.

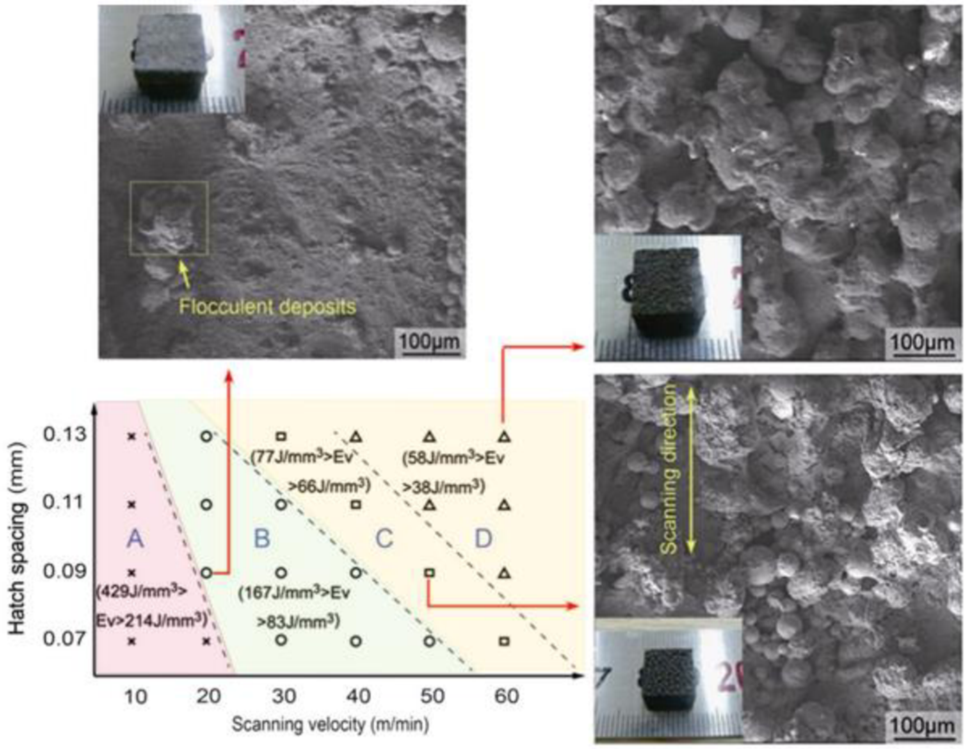

Fig 2.7 Process map describing the behaviour of AZ91D alloy depending on the energy density [44].

The inconsistency of the results between the authors gave rise to further work [34], which aimed to verify the results of the study [44]. In this work, the behaviour of weld deposition tracks was investigated when changing the laser power and the scanning speed. Thus, areas were determined where the weld deposition tracks were stable, did not spatter and their shape was continuous. The behaviour of the weld deposition tracks was recorded on the relevant graphs (Fig 2.8). It has been confirmed that the laser power has a more fundamental effect on the production process than the scanning speed, both in terms of the shape of the weld depositions and the amount of evaporated material.

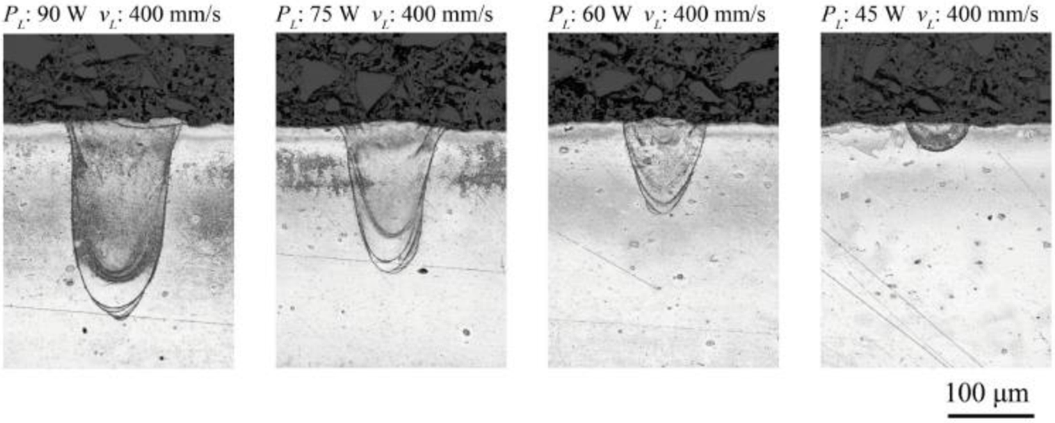

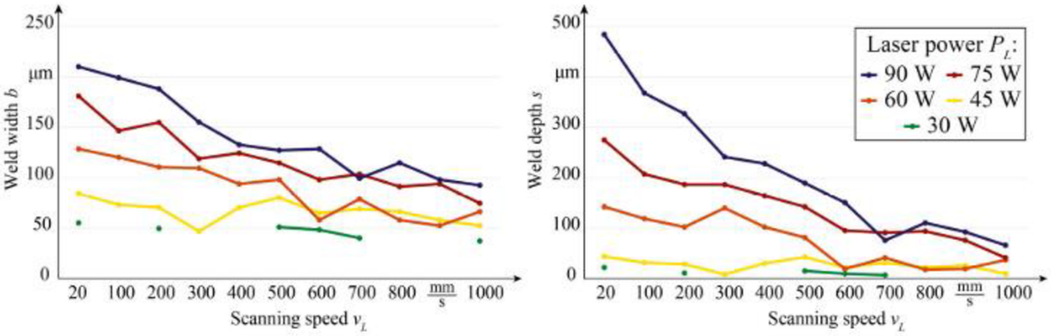

Fig 2.8 Influence of laser power and scanning speed on the shape of weld depositions made of AZ91D alloy [34].

As part of the work, a volumetric sample was also created to serve for the optimal setting of the overlap of the weld deposition hatches so that no defects would occur at the interface of the weld deposition tracks (Fig 2.9). However, this goal was not met and the defects were not completely eliminated. Nevertheless, it has been found that increasing the energy density by increasing the hatch overlap does not increase the evaporation of the material as sharply compared to increasing the laser power. At the same time, it was noted that the change in the height of the deposited powder layer in the range of 15–60 µm does not have a significant effect on the production process for AZ91D alloy. Probably due to the large penetration of the weld deposition tracks.

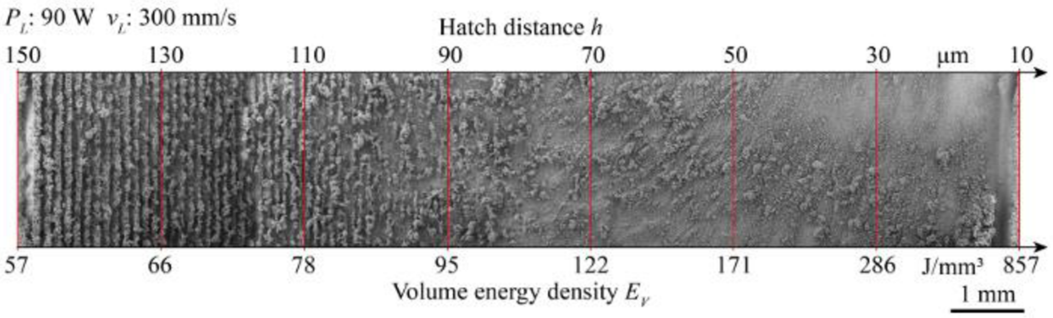

Fig 2.9 Surface of the volumetric sample produced by gradually increasing the overlap of the weld tracks [34].

The results of the studies showed that increasing the laser power leads to a homogeneous material without defects. However, as the laser power increased, so did the amount of vaporized material, which prevented further testing in this direction. This problem began to be solved by designing a new inert atmosphere circuit in order to take the process emissions away from the process chamber (Fig 2.10). This concept opened up the possibility of processing magnesium and its alloys using energy densities higher than 100 $J\cdot m^{-3}$.

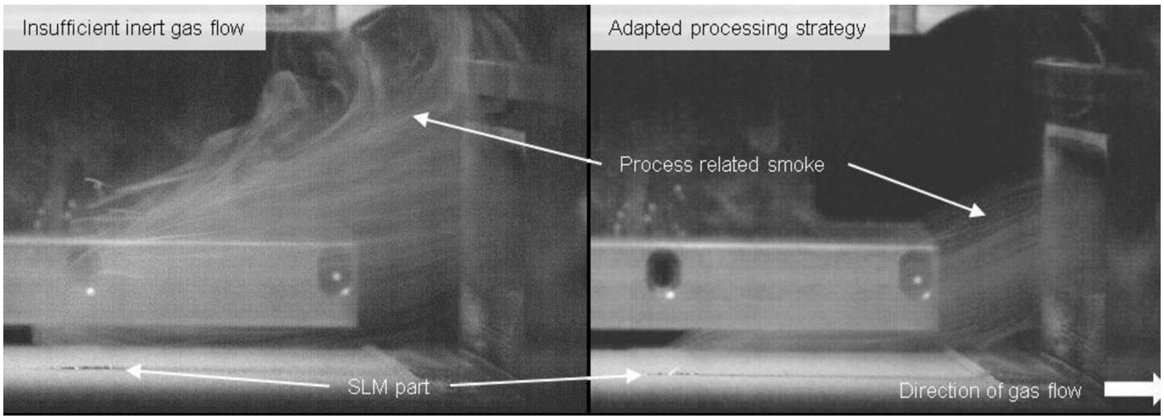

(a) (b)

Fig 2.10 Recording of vapours during the AZ91D alloy printing process: (a) without modification of the inert atmosphere circuit; (b) with a modified inert atmosphere circuit [45].

2.2.3 Processing of Mg-Y-Nd (WE) alloys by SLM method

In addition to gradually increasing the energy density, another different approach was chosen to achieve a high relative density of the samples. This approach has been briefly described here [33]. It was the printing of magnesium alloy WE43 with energy densities lower than those used for the printing of aluminium alloys. The energy was supplied to the melting site mainly via increasing the hatch overlap instead of increasing the laser power. In addition, remelting followed after each layer produced, and the resulting energy density was thus divided into two equal steps. In this way and by increasing the scanning speed to mm$\cdot$s^{-1} the depth of weld depositions in the samples was limited. In this manner, a relative sample density above 99 % would be achieved with mechanical strength comparable to conventional production methods. In addition, the reduction in laser power led to a reduction in the amount of evaporated magnesium. Nevertheless, the samples contained a number of defects that negatively affected their properties (Fig 2.11).

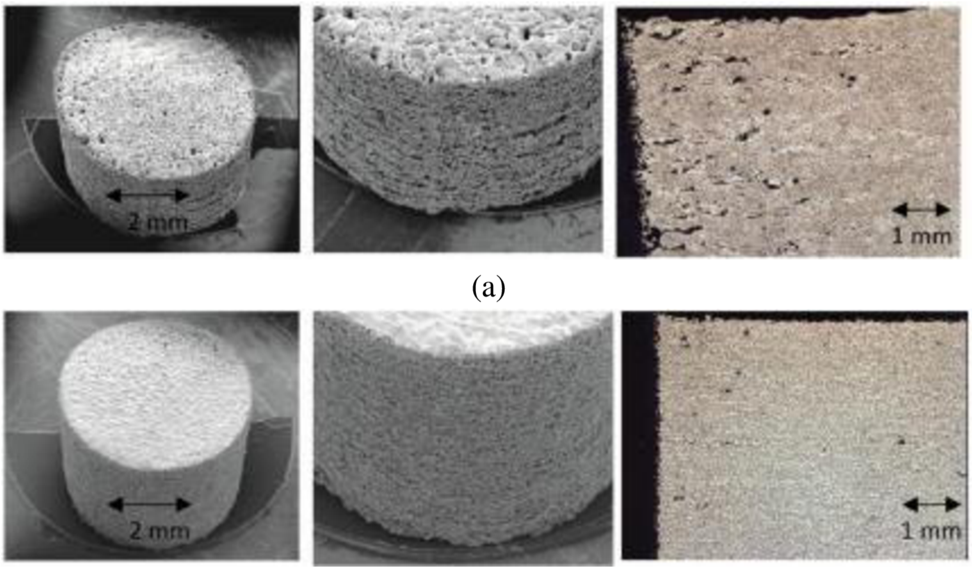

(a)

(b)

Fig 2.11 Comparison of the use of conventional production strategy (a) and remelting of layers (b) [33].

Efforts to reduce the porosity of the produced samples to a minimum have led to testing the effect of hot isostatic pressing (HIP) on the change of defects in the material This had a significant effect on the samples with porosity of 1.75 % or more. The application of HIP to the samples with a porosity below 0.5% had a minimal effect on both the resulting relative density of the sample and its compressive strength. The microstructure of the produced samples contained compounds typical for WE43 alloy (Y_2O_3, $Mg_{24}Y_5$, MgO, $Mg_{41}Nd_5$, etc.), even after HIP application. The highest value of relative density achieved was 99.6 % using the process parameters Lp = 195 W, Ls = 800 mm·s, Hd = 20 μm, Lt = 30 μm.

Increasingly, reaching the relative density of samples above 99 % has led to the novice publishing activity via follow-up analyses. One of them was the description of the ultimate strength of the WE43 alloy created by SLM tensile diagram [38]. The results were related to the cast and extruded material. During the tensile test of SLM samples, a significant yield strength was observed and the SLM processed material achieved comparable properties as the extruded material (Fig 2.12). Only the elongation of the extruded material was about 40 % higher compared to the SLM material. This was mainly due to the fine-grained structure after laser processing. Contour porosity repeatedly appeared in the samples produced by SLM. The reason was probably the choice of a construction strategy where the laser rotated at the sample boundaries. The accumulation of heat at the point of rotation gave rise to spherical pores in which the surrounding gas was trapped.

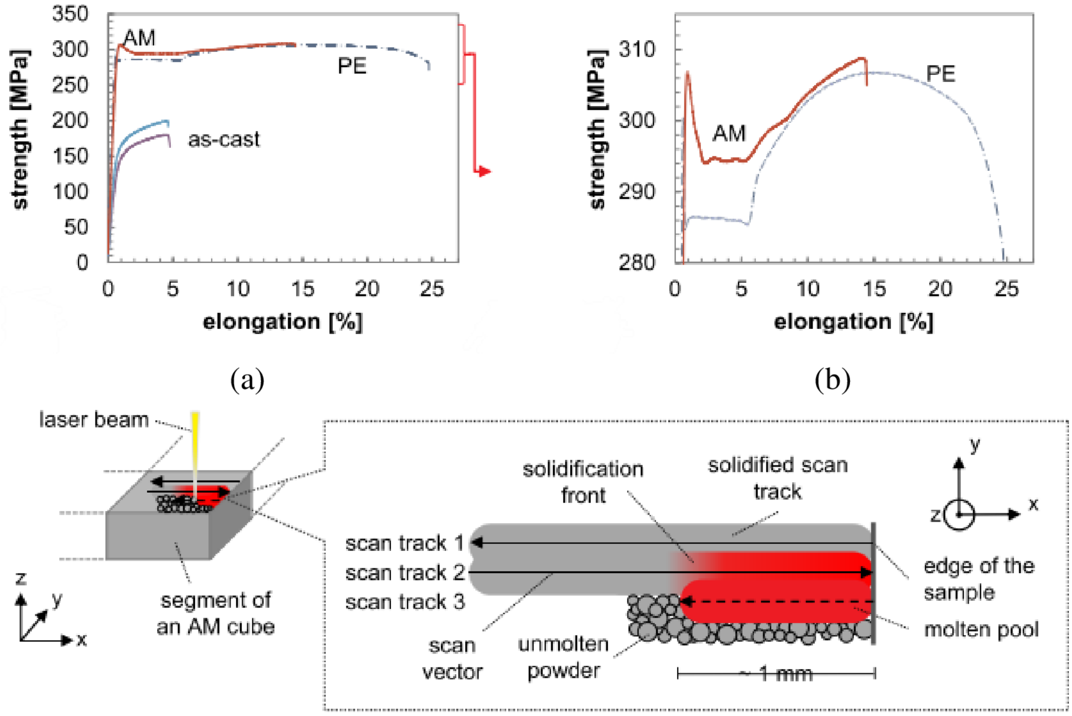

(a)

(b)

(c)

Fig 2.12 Recording of the tensile test at room temperature: (a) the entire course of the test; (b) detail of the transition from yield strength to ultimate strength; and (c) scheme of formation of superheated areas in the sample contour [38].

A more detailed analysis of the microstructure of the WE43 alloy revealed a different distribution of RE secondary phases of rare earth elements [46, 47]. Compared to the cast material, the shape of the particles was similar, but their size was significantly smaller. This was due to the rapid cooling of the melt during the printing process. As a result, large cathodic phases were not formed at the same time, but the Y and Nd elements were homogeneously distributed in the material structure. A solidifying front after the passage of the laser was also observed in the structure of the material. As a result, a significant grain directionality was evident in the material (**Fig 2.13**). The regions found could be designated as a heat-affected zone, a lamellar zone at the boundary of the fusion penetration and, at the surface of the samples, the last track after the passage of the laser. These changes carry different properties of the SLM processed material.

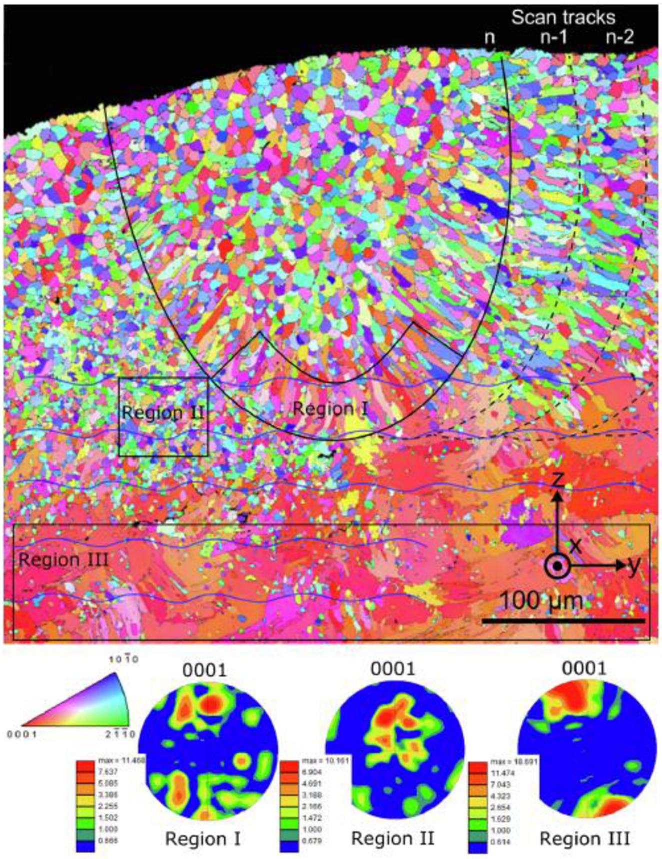

Fig 2.13 EBSD map of the last solidified layer of material around the melt pool [46].

An integral part of the printing of magnesium and its alloys is the occurrence of evaporation of the magnesium matrix. The susceptibility of the process to blurring the laser beam was partially solved by modifying the inert atmosphere circuit of 3D printers. However, evaporation during printing was not completely dealt with. Hyer et al. [48] proved that the printing of WE43magnesium alloy in the range of energy densities of 20–50 J·m^{-3} is possible with the achievement of a relative density of the sample close to 100 %, though due to evaporation of the material, their data have a large variance. At the same time, a higher compressive and tensile strength was achieved than when processing the material by casting. However, it was found in the work that, after printing, a higher concentration of RE elements appears in the material. The reason was the higher susceptibility of magnesium to evaporation than rare earth elements (Fig 2.14). This must be taken into account during printing and possible recycling of the powder.

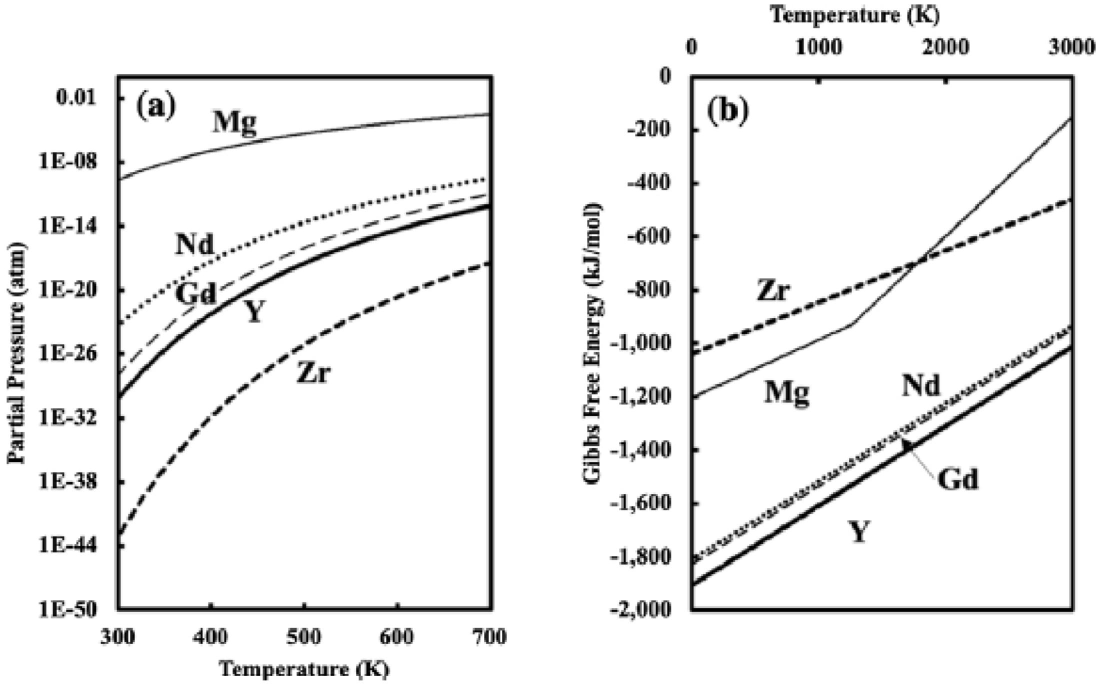

(a) (b)

Fig 2.14 Vapor pressure (a) and Ellingham diagram (b) for the main alloying elements of WE43 alloy [49, 50].

2.3 Oxidation of magnesium and its alloys

2.3.1 Principle and behaviour of oxidation at standard temperatures

Magnesium and its alloys are subject to several types of corrosion. One of them is crystal corrosion, which occurs over a wide range of pH values. The essence of this type of corrosion is the thermodynamic instability of the metal in the environment and its effort to move to a more stable state of corrosion products through oxidation and reduction. This creates an oxide layer which, if it covers the entire metal surface, can have passivating effects. The formation of such a layer is governed by the Pilling-Bedworth molar volume rule. The chemical composition of the passivation layer depends on the chemical composition of the surrounding environment. Intergranular corrosion in magnesium alloys is not dominant, as grain boundaries usually have a higher corrosion resistance than the grains themselves [51, 52]. Magnesium alloys show a relatively good corrosion resistance in airy and dry atmospheres. The presence of joints or shapes in which water and other solutions can be retained allows for the formation of a galvanic cell, which significantly contributes to increasing the local corrosion rate.

The galvanic cell is formed at the interface of metals, which creates a large potential difference to magnesium. Galvanic corrosion can thus occur between joints (typically a magnesium sheet and steel bolts), but also within one material between its individual phases in the microstructure. Corrosion attacks the more electronegative of the pair of metals. Even in the case of galvanic corrosion, a passivation layer can form, which increases the corrosion resistance of the material. The formation of a passivation layer or possible immunity of the metal to galvanic corrosion can be predicted from the Pourbaix diagrams (Fig 2.15). The reaction describing the decomposition of the cathode by dissolving Mg to form hydrogen is given in Equations 2.2 and 2.3.

$$Mg \rightarrow Mg^{2+} + 2e^- \tag{2.2}$$

$$2H_2O + 2e^- \rightarrow H_2 + 2OH^- \tag{2.3}$$

The higher the potential voltage between the cathodic and anodic parts, the higher the reaction rate [53]. At the same time, the corrosion rate also affects environmental conditions such as temperature and solution pH. The flow of the electrolytic solution also has a very negative effect on the corrosion resistance of magnesium. Studies show that the corrosion resistance of a sample can be reduced 3-6 times in such an environment [54]. To improve the corrosion as well as mechanical properties, magnesium alloys are inoculated with alloying elements. One of the common alloying elements of magnesium alloys is aluminium. Aluminium is inexpensive, light, increases strength characteristics and reduces the anodic reaction rate of magnesium. Therefore, Mg – Al alloys do not corrode as much as magnesium alone [55]. Other alloying elements of magnesium alloys are Nd and Y. The use of these alloying elements creates intermetallic phases in the alloy, which serve as local cathodes and thus contribute to increasing the corrosion rate in the alloy [56]. On the other hand, the precipitates significantly refine and homogenize the grain. The fine grain increases the grain boundary density, which aids in the passivation of the alloy [57]. As a result, despite the higher amount of cathodic phase, it can be stated that Mg-Nd-Y alloys have the highest corrosion resistance from among the magnesium alloys [53].

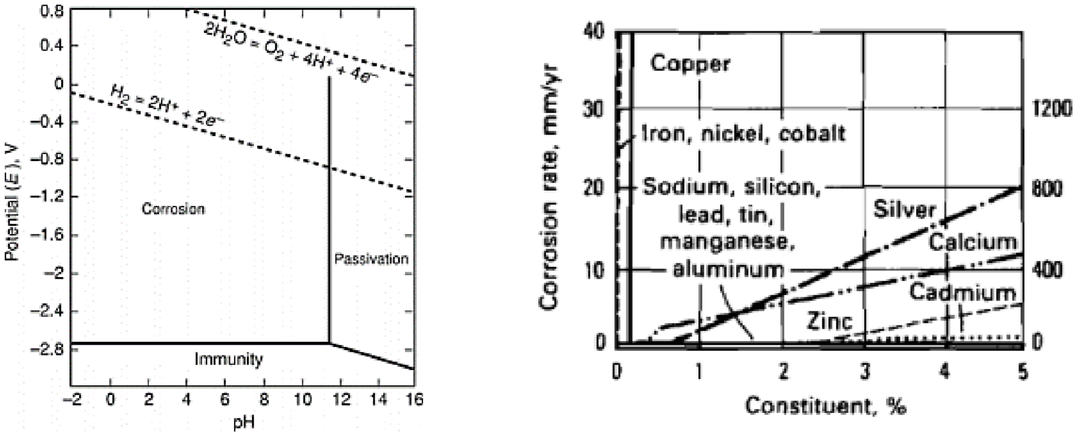

(a) (b)

Fig 2.15 (a) Pourbaix diagram for Mg (H_2O_3, 25 °C) [59] and (b) effect of additive elements on Mg corrosion in 3 % NaCl solution [58].

As mentioned above, a higher corrosion resistance can be achieved by refining the grain. The resulting grain size corresponds to the technology by which the material is processed. By far the best results can be achieved with laser surface melting (LSM) technology[59, 60]. This technology consists in remelting the surface of the material with a laser beam, which creates a fine-grained structure on the surface of the material due to the high temperature gradient. The laser affects the material to a depth of about one millimetre. In addition, in the case of Mg-Nd-Y alloys, intermetallic phases ($Mg_{12}Nd$, $Mg_{14}Nd_2Y$, etc.) dissolve in the α-Mg solution in the area affected by the laser, thus reducing the proportion of cathodic phases and reducing the corrosion rate [61]. Similar fine grain can be achieved by using additive technologies such as selective laser melting (SLM) or electron beam melting (EBM).

2.3.2 Oxidation of magnesium alloys at elevated temperatures

The corrosion behaviour of magnesium and its alloys has been well described in the literature [62]. The corrosion rate is directly-proportionally dependent on the ambient temperature (Fig 2.16). Up to temperatures close to 200 °C, the dependence appears to be linear. Increasing the corrosion rate is related to higher free energy, which is a driving force of oxidation and reduction. Above these temperatures, an ever-stronger exponential trend begins to appear, which is caused by the constant violation of the passivation layer on the surface of the material. This is mainly due to thermal expansion on the surface of the material and subsequent delamination of the already corroded layer. At temperatures above 500 °C (temperatures close to autoignition of magnesium), magnesium and its alloys are subject to catastrophic corrosion. The passivation layer is even more stressed, this time by the stress caused by the pressure of evaporated Mg..

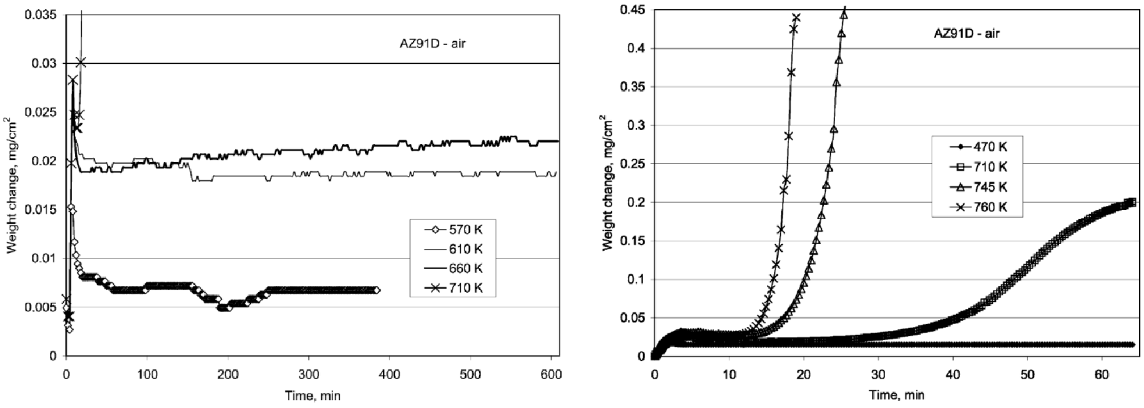

(a) (b)

Fig 2.16 (a) Influence of ambient temperature on the corrosion rate of AZ91magnesium alloys and (b) detail of the first hour of test [62].

The passivation layer of magnesium alloys is usually formed in separate regions and subsequently a continuous film is formed. The reason for this behaviour is usually the anisotropic distribution of intermetallic particles in the alloy. The passivation layer most often contains MgO and intermetallic compounds corresponding to the alloying elements of the given magnesium alloy. Mg_3N_2 compounds also appear in the passivation layer during oxidation at elevated temperatures. The reason is the exothermic reaction occurring between Mg and N at elevated temperatures; this contributes to a very poor extinguishing of the magnesium flame.

At temperatures close to the autoignition of the magnesium alloy, vapours are formed which react strongly with oxygen to form MgO. This reaction is freely expressed by equation 2.4.

$$Mg\text{–}O_{Solution} \rightarrow Mg + MgO \qquad (2.4)$$

2.3.3 Inert atmosphere when printing magnesium and its alloys

Since the temperature at the point of impact of the laser can approach temperatures above 2500 °C during the SLM process, it is necessary to process magnesium alloys under a protective inert atmosphere. As standard, magnesium alloys are printed in an argon protective atmosphere. The input metal powder is usually covered with a passivation layer, which is subsequently broken during the production process. By melting the passivation layer, bound oxygen is released. Even the presence of a flame cannot completely block the access of oxygen to the surface of the molten material [63]. As a result, a passivation film is formed on the surface of the material; however, this film is immediately substantially disturbed by the pressure of the evaporated Mg and thus reveals another melt involved in the oxidation process. If this process lasts long enough (minutes to hours depending on temperature) and has sufficient access to oxygen, the alloy may blaze up [64]. Due to exothermic reactions with oxygen (nitrogen), in practice, the material is on fire until the entire Mg content is burned out. For these reasons, it is necessary to maintain a protective atmosphere in sufficient concentration.

By disrupting the passivation layer, part of the released oxygen is bound to the newly formed passivation film, part of the released oxygen is burned, and the rest is released into the process chamber of the machine. This process cannot be prevented even by an ultra-pure argon atmosphere [65, 66]; therefore, during the production process, it is necessary to keep the oxygen value below 0.2 % by constant argon flow. However, at the same time, the question arises as to whether it is necessary to maintain a pure argon inert atmosphere or to use some other gases. Results from some publications suggest that optimizing the composition of the inert atmosphere can increase production repeatability and a range of results [67].

2.4 Corrosion behaviour of WE43 alloy processed by SLM

Successes in the field of additive processing of magnesium alloys have opened a new issue - corrosion resistance of SLM processed material. This may be different for volumetric samples and for structured material. One of the first studies dealing with the corrosion resistance of lattice structures made using SLM from WE43 magnesium alloy was reported in 2018 [68]. Information on how to prepare the samples is completely missing. However, depending on the machine used, the laser power did not exceed 230 W. Nevertheless, the produced samples show a very poor surface quality caused by fusing of the surrounding powder to the surface of the structures. The relative density of the lattice structure samples was 64 ± 0.2% (expected density was 66.7%). The samples were also found to have a different microstructure than the volumetric samples. The reason was probably a different heat dissipation in both cases. The samples retained basic mechanical pressure integrity even after 28 days in a solution simulating the environment of the human body. During this time, the amount of released hydrogen was recorded as basic information to determine the corrosion rate of the structures (Fig 2.17), and, though the structures contained a number of lacks, there was a significant progress compared to the results to date.

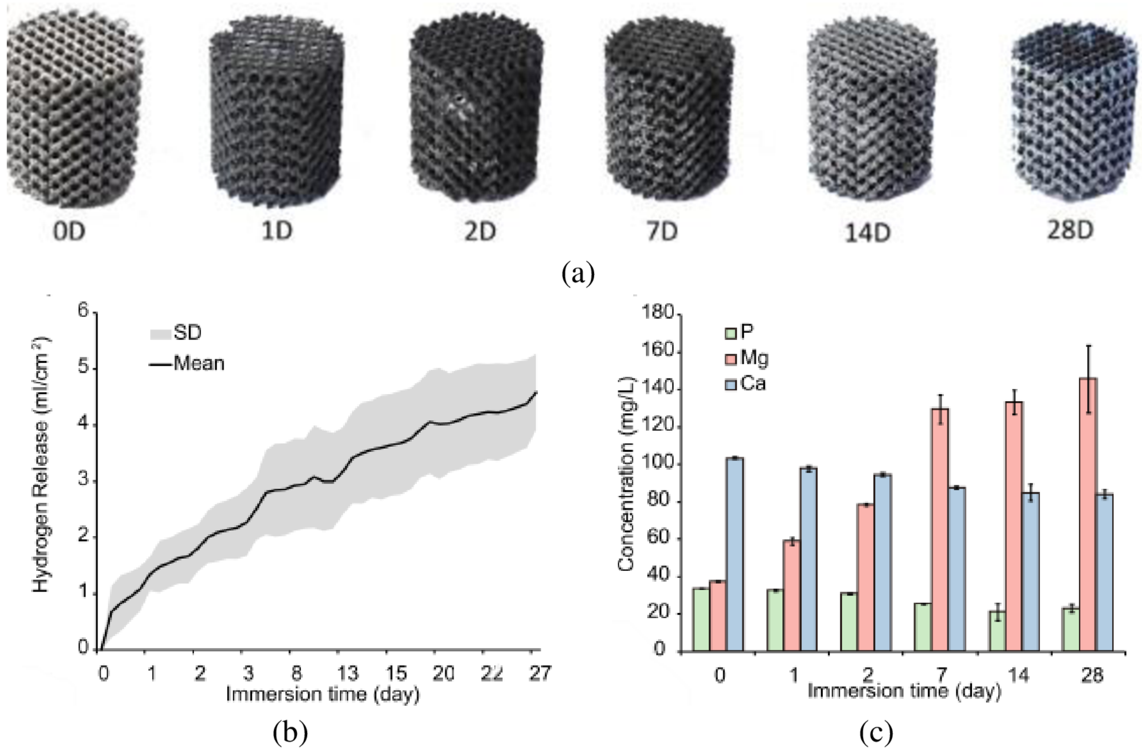

(a)

(b)

(c)

Fig 2.17 (a) Lattice structures exposed to the corrosion solution for 28 days and records of hydrogen release (b) and concentrations of selected elements in the solution during the corrosion test (c) [68].

To increase the corrosion resistance of lattice structures, their surface was modified by plasma electrolytic oxidation (PEO) [69]. In order to modify the surface of the structures, it was first necessary to chemically etch the surface with phosphoric acid to remove the fused powder (Fig 2.18). The passivation capabilities of the layer created by PEO during a corrosion test in a simulated human body environment slightly reduced its corrosion protection. Corrosion tests lasted 21 days in total. Mg $(OH)_2$ hydroxide was formed as the first compound, which gradually reduced the reactivity of the alloy and allowed for the material to degrade only through diffusion. However, the presence of Cl^- ions continued to disrupt the Mg $(OH)_2$ layer, resulting in a more stable $MgCl_2$ phase. The formation of $MgCl_2$ significantly increased the number of cracks in the PEO layer, thus accelerating the corrosion of the material. In these cracks, the corrosion penetrated to a depth below the passivation layer and caused pitting. Heat treatment with a solidus temperature of 530 °C for WE43 accelerated corrosion. The reason was probably the increase in the number of grain boundaries along which the corrosion was mostly propagating. The main cause of corrosion was the formation of micro-galvanic cells between the cathodic phases in the material structure.

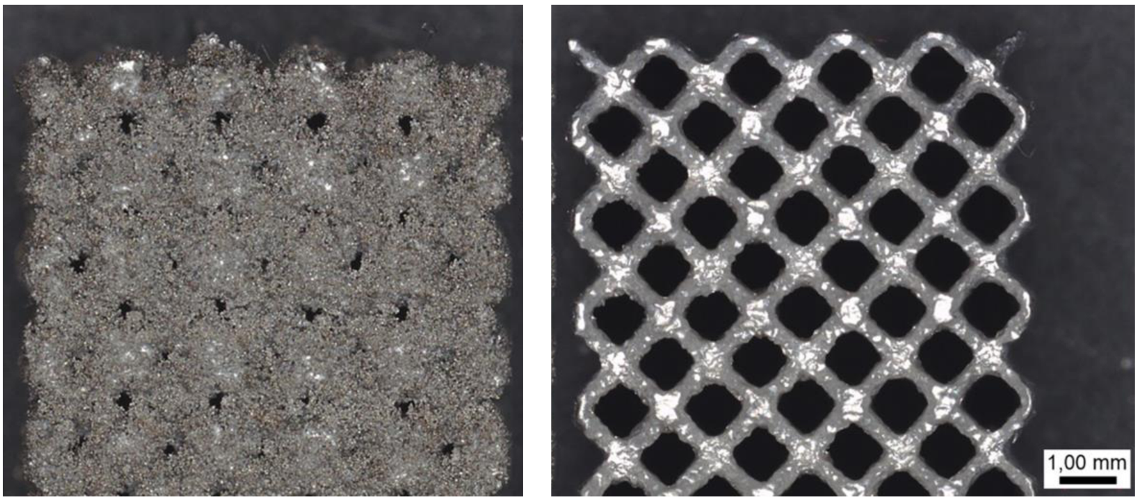

(a) (b)

Fig 2.18 Comparison of the produced lattice structure before chemical etching (a) and after its application (b) [69].

When testing the corrosion rate of WE43 alloy treated by the SLM method, an increase in the degradation of the material was observed during laser processing compared to casting (Fig 2.19). The cause was the kinetics of the cathodic reaction due to the high affinity of Y and Zr for oxygen. Especially Zr formed larger agglomerations, which were the main initiators of the reaction. However, the authors themselves state that this assumption must be subjected to a more detailed test, as it goes against generally accepted claims [53, 70, 71].

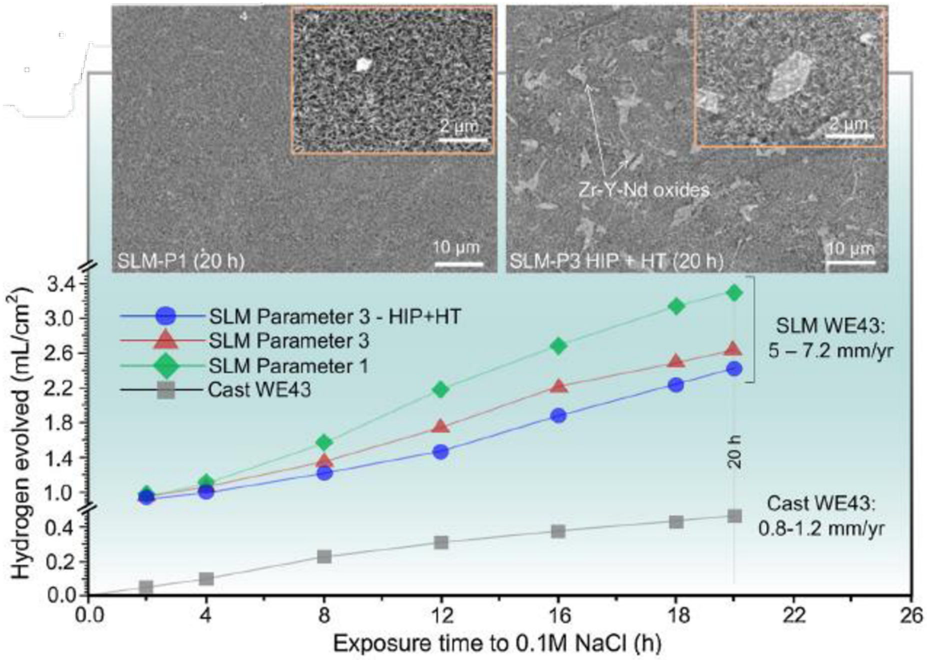

Fig 2.19 Hydrogen evolved during a corrosion test in a salt solution lasting 24 hours for different types of samples [47].

3 ANALYSIS OF THE CURRENT STATE OF THE ART

3.1 Evaluation of oxidation of magnesium and its alloys

Magnesium generally has a high affinity for oxygen. It reacts naturally rapidly with oxygen to form MgO. The thickness of the MgO passivation layer is low and the mechanical properties of its connection with the $\alpha - Mg$ matrix are also generally low. In addition, the layer gradually disintegrates due to electrochemical corrosion, exposing the α-Mg matrix, which reoxidizes [53].

In the case of magnesium alloys, alloying elements also participate in the formation of the passivation layer. In the case of AZ alloys, it is aluminium to form Al_2O_3. This passivation layer is more stable and reduces the proportion of the anodic part in the $\alpha - Mg$ matrix [55], thus reducing the corrosion rate compared to pure magnesium. More corrosion-resistant than AZ alloys are RE alloys, which also include the WE43 alloy. This alloy precipitates in the Mg-Nd-Y equilibrium ternary system to form phases such as $Mg_{12}Nd$, $Mg_{14}Nd_2Y$ etc., which reduce the content of the cathodic phase in α-Mg [53, 61] and thus contribute to reducing the corrosion rate. At the same time, Mg_3Nd a Y_2O_3 phases are formed in the passivation layer; they are more stable than MgO, and the degradation of the passivation layer slows down [72, 73]. In addition, yttrium has a higher affinity for oxygen than magnesium. For this reason, the Y_2O_3 phase is preferably formed instead of MgO.

As a result of the passivation film, the corrosion rate of magnesium slows down and becomes almost constant until the critical temperature is exceeded. The critical temperature is somewhere in the range of 400-450 °C and may vary slightly for magnesium alloys. When the critical temperature is exceeded, the oxidation of magnesium starts to increase sharply [62]. There are several reasons. One of them is to increase the diffusion rate of Mg^{2+} cations. Furthermore, it is the gradual formation of a melt on the surface, which disrupts the passivation layer, creates cavities in the material and is generally more reactive due to the increased energy. Oxygen penetrates the material along grain boundaries and cracks in the passivation film. The formation of oxides below the passivation film leads to the gradual peeling of the passivation film particles and the exposure of other sites for the development of oxidation.

As the temperature rises above the critical limit, magnesium corrosion starts to increase exponentially. The reason is the gradual evaporation of the magnesium matrix. The accumulated vapours expand through the passivation film, which is broken. In the area where the sample surface is exposed to reactive vapours, violent oxidation can begin to form MgO and other compounds, which can lead to the formation of a flame. This is an exothermic reaction that continues to locally increase the temperature above the surface of the material [63, 64].]. The fact that it is necessary to reach at least the melting point of magnesium in order to form a flame proves that the occurrence of magnesium vapours certainly includes the burning of the flame. Evaporation of magnesium is a typical feature of its oxidation at elevated temperatures. An increase in temperature due to oxidation can lead to the self-ignition of magnesium. The flame temperature of magnesium is in the range of 3000-5000 °C. Extinguishing the magnesium material is difficult. Burning usually lasts until all the magnesium has burned out, or until oxygen is present.

Based on these results, it can be stated that magnesium must be processed under an inert atmosphere. The SLM technology commonly uses nitrogen, or argon atmosphere. However, at elevated temperatures, magnesium has been proved to undergo nitriding [66]. Nitriding is an exothermic reaction during which the material is saturated with nitrogen. Nitride formation during the SLM process can lead to delamination of the layers, increase in porosity, inhomogeneity in the structure of the material. Chemical reactions that occur during the construction process can be validated from the powder process emissions [65] and, if necessary, the production conditions can be retrofitted.

In general, it is necessary to produce magnesium and its alloys under an argon inert atmosphere that is more inert than nitrogen. However, the presence of the inert atmosphere does not completely prevent the oxidation of magnesium at elevated temperatures [32, 40–42, 66].]. The oxygen bound to the powder material is released during melting and begins to react violently with the surrounding material and the released vapours. During the SLM process, the material is completely melted and many studies indicate that evaporation of magnesium is a common component of this process [33, 38, 44, 74]. For these reasons, an oxygen mist is constantly generated above the melt pool, which reacts with the vapours to form a black MgO mist. The resulting vapours fill the production space of the 3D printer during production [30]. To ensure the removal of process emissions and released oxygen, the process chamber must be under a constant flow of inert atmosphere. However, the gas flow increases the pressure in the chamber. Even a low value of the partial pressure increase will result in an increase of oxidation, as oxygen is pressed against the surface of the melt [65].

Since the surface of the produced weld depositions is always covered at least in part by a layer of oxides, it is necessary to melt them at each subsequent pass in order to join the individual layers of material. In the case of insufficient energy, cracks and porosity can form at the layer interface The reason for their formation is the high melting point of oxides (2500–3000 °C) in the passivation layer (Mg_3Nd, Y_2O_3, MgO, etc.) compared to the low temperature of 1091 °C, at which pure magnesium is evaporated. As a result, pores appear in the material due to non-melting of oxide layers or intense production of magnesium vapours.

To summarize, magnesium must be produced in the argon inert atmosphere with a constant gas flow. The gas flow and its composition can be optimized to reduce the oxidation in the chamber. During production, the oxidation of magnesium produces vapours which must be removed from the melt pool. These vapours can defocus the laser beam. Oxidation during the production process cannot be prevented in the argon inert atmosphere without affecting the porosity of the manufactured parts. However, it can be partially controlled by selecting process parameters.

3.2 3D printing of magnesium and its alloys

During the processing of pure magnesium, a number of weld deposition tracks were produced. Their geometry and continuity were determined depending on the laser power and scanning speed. Thus, the initial region of linear energy density was determined, where pure magnesium is processable [40, 41]. Due to oxidation, the surface of the weld depositions was covered with molten powder particles, which reduced the surface quality of the weld depositions [40]. The concentration of oxides increased with increasing energy density [42], which corresponds to a higher rate of oxidation at higher temperatures [62]. Reducing the oxidation of weld depositions reduces the balling effect and surface tension. As a result, the weld depositions become wider and smoother [32]. In addition, the higher energy density led to the formation of larger grains, thus reducing their hardness. The use of a pulse laser mode led to the evaporation of magnesium rather than its melting. In contrast, the continuous laser mode melted the powder and the melt pool was stable. By preheating the build plate, a better connection of the weld depositions to the plate was achieved and their tracks were more continuous [32].

After the weld deposition test, a series of cubes were made to determine the porosity of the material [43]. The range of tested process parameters was P = 15–150 W, Vs = 50–100 mm/s Hd = 100 μm, Lt = 30 μm. The best result was achieved with P = 90 W and Vs = 100 mm/s. The relative density of the sample was 95 % and hardness was 46-52 HV. The time delay during the layers printing was also tested. This showed the greatest effect on the surface quality, which improved by up to 10 μm Ra. During the production of samples, the chamber was filled with magnesium vapour, which blurred the laser beam.

Another material processed was AZ91magnesium alloy. Like pure magnesium, this alloy showed sensitivity to evaporation. The production of large series of samples is not possible without sufficient MgO mist extraction. Otherwise, the laser beam is blurred, which reduces the energy density of the melt pool, and porosity appears in the samples [30]. An energy density range (83–167 J/mm^3) was found for AZ91 processing, where the process should operate continuously [30, 44]. Several analyses have been performed to find the correct weld depositions spacing and to adjust the layer height [35, 44]. The best result was obtained with parameters P = 200 W, Hd = 90 μm, Lt = 40 μm, Vs = 333 mm/s with 99.52 % relative density [44]. Cross-sections revealed that the depth of the weld deposition track is 312 μm, which leads to remelting of 6-8 layers. The trend of changing the geometry of AZ91 alloy weld depositions to change the process parameters was the same as in the case of pure magnesium, but the values were different for both materials.

Volumetric samples were produced for the WE43 alloy. The aim was to find a combination of process parameters leading to the highest relative density of samples. Two methods of how to produce low porosity samples were presented. In both cases, the samples reached relative densities higher than 99 % [33, 38, 75]. The first method uses process parameters P = 90 W, Vs = 800 mm/s, Hd = 45 μm, Lt = 50 μm together with the remelting of already produced layer [33]. The second method continues to use higher laser power thus remelting 5–7 layers [38, 75]. In both cases, the layers are remelted, but each time in a different way. The benefit of obtaining a higher relative density by remelting the layers was also observed by Wei et al. [44]. The relative density using the first method resulted in a porosity of more than 99 %. The second method shows a porosity better than 99.6 %. A closure of pores by isostatic hot pressing has also been tested [75]. However, the result was only the closure of large pores, the processing had almost no effect on small cavities.

Tab 3.1 Overview of the ranges of process parameters used.

Material	Powder characteristics	Type of machine	Laser focus [µm]	Laser power [W]	Scanning speed [$mm \cdot s^{-1}$]	Hatch distance [µm]	Layer thickness [µm]
Mg [40, 41]*	Spherical shape, Distribution D_{50}= 25 µm	SLM of own production (Nd: YAG laser)	600	13–36	10–200	–	500
Mg [39]	Spherical shape, Distribution D_{50}= 25 µm; Plate preheating 120°C	SLM of own production (Nd: YAG laser pulse mod)	270	8.9–17.7	10–200	–	150–300
Mg [43]	Spherical shape, Distribution D_{50}= 25.85 µm and D_{50}=43.32 µm	EOS M280 (Nd: YAG laser)	100	15–150	50–100	100	30
Mg-9%Al [30]	Mg non-spherical shape; Distribution D_{50}= 42 µm; Al non-spherical shape; Distribution D_{50}= 17 µm;	Realize 250 (Nd: YAG laser)	34–75	10–110	50	80	10–1000
AZ91D [36]	Spherical shape, Distribution D_{50}= 30 µm	(YRL-200 laser)	100	200	166.6–1000	80	40
WE43 [33]	Spherical shape, Distribution D_{50}= 31 µm	SLM 125 (YRL-100 laser)	70	20–100	100–10000	15–120	50
WE43 [33]	Spherical shape 15–63 µm; Plate preheating 35°C	EOS M270 (Nd: YAG laser)	–	135–195	800–1200	20–25	30
WE43 [38]	Spherical shape 25–63 µm	AconityMini (YRL-200 laser)	90	200	700	40	30
WE43 [49]	Spherical shape 4–40 µm; Plate preheating 100°C	SLM 125 (YRL-100 laser)	70	50–200	100–1600	130	40

*Only weld deposition tracks produced

Tensile samples were always built with the found parameters. In the case of the first production method, yield strength of 194 MPa, ultimate strength of 312 MPa and tensile strength of 14 % were reached [33]. The second method reached E = 45.7 ± 1.5 GPa, Rm = 306.0 ± 0.5 MPa, $RE_{0,2}$ = 296.3 ± 2.5 MPa and A_0 = 11.9 ± 1.3 % [38]. In the second method of production, a significant yield strength was also found. The impact pressure test was also validated for the second production method. Here, a strong dependence of the resulting mechanical properties on the porosity rate was evident [75].

The first structures were also built from WE43 material [74, 76]. The tests of structures were focused on biocompatibility with the human body, corrosion resistance, shape accuracy and mechanical integrity. The surface quality of the structure is poor here. On the contrary, biocompatibility, shape and pressure testing brought the desired results. However, the authors do not provide any details regarding the production of structures.

An analysis of current publications shows that the processing of magnesium and its alloys repeats the same problems caused by the physical nature of magnesium and can be solved in similar ways. An overview of the ranges of process parameters used in individual publications is given in Tab 3.1. However, publications indicate that process parameter settings may not be applicable when being transferred to another production machine [34]. The reason may be a different design of the printers. The setting of the laser power has the greatest effect. When transferring the parameters, it is important to ensure that, in both cases, the laser has the same mode (continuous, pulse), beam profile (Gaussian, linear, etc.), focus and wavelength. The second important factor is the method of distribution of the inert atmosphere. The gas of the inert atmosphere not only removes process emissions from the melt site, but also cools the manufactured part. Therefore, it is important to know its flow profile, direction and intensity. For older machines, the distribution of the inert atmosphere was a problem node. Another parameter that can affect the transfer of process parameters is the way in which the pressure in the process chamber is monitored. Some machines only measure the partial pressure, others can change it by feedback adjusting the inert gas flow. One of the last important parameters is the preheating of the build plate. Some of them allow for the build plate to be heated only up to a certain limit, which can vary significantly.

The type of 3D printer on which the tests will be performed is the SLM 280^{HL} first version. It is an older machine equipped with a 400 W YRL fibre laser (λ = 1.07 μm) with a Gaussian profile, continuous mode, and 82 μm focusing. The machine allows preheating of the plate up to 200 °C and control of the pressure in the production chamber. However, the disadvantage of the machine is the distribution of inert atmosphere. The process emissions discharge is insufficient, the inert gas flow is weak and, in the case of magnesium alloy processing, the machine chamber is rapidly filled with process emissions. In more advanced machines, the glass of laser is also protected by a flow of inert gas so that particles of flying powder do not stick to it. These problems are solved in the second version of the device, which is equipped with a more powerful pump of inert atmosphere and adjustment of its distribution.

Many tests based on the current state of the art have been performed on SLM systems of our own production, where the method of distribution of inert atmosphere is not described, or on more advanced machines from EOS GmbH. These machines provide the solution for the distribution of inert atmosphere and protection of laser glass in a more efficient way. However, the best results were achieved on the AconityMINI device. It is an SLM device that has been developed for laboratory purposes, especially for the processing of magnesium and its alloys. The inert atmosphere distribution was designed specifically for highly reactive materials that produce large amounts of process emissions.

The WE43 alloy was successfully processed on three machines. One is EOS M270 [75], the other is AconityMINI [38, 76]. On these machines, WE43 is processed at increased power, which generates a large amount of process emissions in the machine chamber. Due to the improved distribution of the inert atmosphere, the process emissions are more efficiently removed from the machine chamber and do not blur the laser beam and do not stick to the protective glass. Another machine that has relatively successfully processed the WE43 alloy is the SLM 125^{HL} [33]. However, another processing method using a lower power and layer remelting had to be used here, as mentioned above. Due to the lower laser power, not so many process emissions that adversely affect the production process are generated in the machine chamber.

3.3 Definition of main problems

The requirements for a biodegradable implant are primarily its sufficient mechanical integrity and corrosion resistance.

The presented search shows that most of the produced volumetric samples contained a number of defects and disintegrated under load. Their printing was hindered by the vapour barrier of the magnesium matrix, which is a natural phenomenon of laser processing of magnesium alloys. The printing methods described so far use different combinations of process parameters and approaches, while the question remains: what is the repeatability of printing? Often, a more detailed description of the printing strategy for achieving the stated results of the relative density of the samples is missing. However, these studies show that magnesium alloys can be processed with a relative density close to 100 %. To assess which 3D printer settings achieve the best results, it is necessary to understand the influence of individual process parameters on the production process of a chosen material. With defect-free material, such as porosity, shrinkage, etc., the geometry of the implant can be adjusted to achieve human bone-like properties (compressive strength of 130-180 MPa). At the same time, such material can be used for other types of analyses, such as determination of corrosion resistance, toxicity, mutagenicity, etc.

Magnesium and its alloys face low corrosion resistance. This is due to the inability of the material to maintain a compact passivation layer. However, the results from the studies dealing with the laser processing of magnesium alloys show that corrosion of the material can be significantly slowed down. Nevertheless, information on the corrosion behaviour of magnesium alloys processed by the SLM method is still missing. Magnesium and its alloys are subject to atmospheric corrosion, the rate of which is affected by environmental influences as well as the surface quality of the material. In addition to atmospheric corrosion, galvanic corrosion also takes place in the material between the individual intermetallic phases (cathodes) and the magnesium matrix (anode). Because of this joint action, the corrosion rate of magnesium alloys reaches such high values. However, it is not known which of these corrosion methods has a dominant effect on the overall corrosion rate. The corrosion rate limit for biodegradable implants was set at 0.5 $\text{mm}\cdot\text{year}^{-1}$ [69]. From among the conventional methods of processing of magnesium alloys, extrusion is closest to this value, when the corrosion rate of the material reaches the values around 1.5 $\text{mm}\cdot\text{year}^{-1}$. However, laser processing offers the opportunity to change the microstructure of the material and its surface quality. Volumetric samples produced so far using 3D metal printing are characterized by particularly poor surface quality. However, it should depend on the process parameters during production. Therefore, by their suitable combination, it should be possible to reduce the corrosion rate of the magnesium material and thus substantially improve the corrosion resistance of the material.

4 GOALS OF DOCTORAL THESIS

The main goal of the presented doctoral thesis is to clarify the influence of process parameters and technological conditions on the corrosion behaviour of WE43 magnesium alloy produced by SLM method. The goal of the doctoral thesis was built on two scientific questions, which are based on the findings in Chapters 2 and 3. Working hypotheses to be tested during the work were created for these scientific questions. In order to obtain adequate answers to the scientific questions raised and to meet the main goal, it is necessary to develop the following sub-goals:

- Explain the effect of laser power and scanning speed on the geometry and continuity of weld deposition tracks.
- Explain the effect of laser power and scanning speed on the geometry and continuity of weld deposition tracks.
- Determine the effect of laser power and scanning speed on surface quality.
- Define suitable combinations of process parameters for printing volumetric samples.
- Create samples with basic mechanical strength and relative density higher than 99 %.
- Create a basic microstructural description of SLM processed material.
- Determine the corrosion rate of SLM processed material for different surface qualities.

4.1 Scientific questions

Q1. *What influences most the final value of the relative density of the WE43 magnesium alloy?*

Q2. *Is it possible to control the corrosion rate of the WE43 alloy processed by the SLM method by adjusting the process parameters?*

4.2 Hypotheses

H1. *Achieving a relative density close to 100 % is difficult in terms of the physical properties of magnesium. Its proximity to the melting point (650 °C) and the boiling point (1091 °C) causes massive evaporation of the magnesium matrix during printing, which blurs the laser beam and adversely affects the print repeatability. With a suitable combination of process parameters, the energy that melts the material could be distributed in ways other than just using the laser power* [77], *which should help to reduce vapours and stabilize the process.*

The surface quality is directly dependent on the laser power and scanning speed. A combination of these two parameters affects the energy density used to melt the metal powder. Energy density determines the fact whether the metal powder will be fully or just partially melted. Thus, a suitable value of energy density can, to some extent, prevent the surrounding powder from fusing to the surface of the printed geometry [90].

H2. *The surface of magnesium materials produced by SLM is prone to fusing of the surrounding powder. The fused powder is the main reason for the low surface quality and preventing it from fusing would significantly improve the surface of the material* [69]. *This would reduce the area that can be attacked by corrosion and significantly reduce its speed.*

4.3 Structure of doctoral thesis

The presented doctoral thesis moves the issue of biodegradable implants forward. In order to achieve the required implant, it is necessary, in the first phase, to achieve a defect-free material with sufficient mechanical properties and good corrosion resistance. For this reason, the submitted thesis covers two main topics. The first one deals with the experimental development of a printing strategy to achieve 3D material with mechanical properties close to the human bone and a relative density close to 100 %. To achieve the set goal, linear and volumetric samples produced by different combinations of process parameters were gradually tested. The influence of the change of process parameters could be monitored due to the microstructural analysis of the produced samples. Here, the number and type of defects in the material and its chemical composition and distribution of intermetallic particles were monitored. This feedback allowed for a process mapping to describe the behaviour of the alloy using different combinations of process parameters. In individual phases of the work, the hardness of the material was monitored, which provided basic information on its mechanical properties. The compressive strength and three-point bending strength of the volumetric samples were monitored. These monitored properties were selected with respect to the loading of common bone implants.

After achieving these mechanical qualities, a second topic dealing with the corrosion resistance of 3D printed material was developed. As already mentioned, magnesium material is subject to both atmospheric and galvanic corrosion. By processing the material using the SLM method, the material surface quality and microstructure change, which also changes the corrosion behaviour of the material. The aim of this part of the work was to define the corrosion rate of 3D printed material and to try to reduce it as close as possible to the value required for biodegradable implants. To make the orientation in the topic clearer, the overall corrosion rate was viewed from two perspectives - atmospheric corrosion related to surface quality and galvanic corrosion related to cathodic phases in the microstructure of the material. A microstructural analysis of the volumetric samples provided a closer insight into the behaviour of the 3D printed material and a description of how the material corroded. At the same time, an analysis of the sensitivity of surface quality to changes in laser power and scanning speed was performed. Thus, the basis for improving the corrosion resistance of the material was obtained. Finally, corrosion tests of 3D printed material with different surface qualities in a simulated human body environment were performed to determine the corrosion rate of 3D printed material.

The submitted PhD thesis was linked to the research project FV20232 – Biodegradable structured implants created by 3D metal printing. The project dealt with the basic processing of the WE43 alloy using SLM and the transition from the original volumetric seal of hip joint to its structured variant. The thesis solves several sections of this research project.

During the work on the project, a closer relationship was established with the research group at the Czech Technical University in Prague and CEITEC in Brno, which participated in the project. Due to the multidisciplinary topic of the presented thesis, the results and conclusions were consulted with these colleagues. Within the cooperation, several joint articles were published mapping the main results of the thesise.

Article A

Suchy J, Horynová M, Klakurková L, Palousek D, Koutny D, Celko L. Effect of laser parameters on processing of biodegradable magnesium alloy WE43 via selective laser melting method. Materials (Basel). 2020;13(11).

- *Materials MDPI – IF 3.623, Q2*
- *Autorovo přispění 65 %*

Article B

Krištofová P, Roudnická M, Kubásek J, Paloušek D, Suchý J, Vojtěch D. Influence of Production Parameters on the Properties of 3D Printed Magnesium Alloy Mg-4Y-3RE-Zr (WE43). Manuf Technol. 2019 Oct 24;19:613–8.

- *Manufacturing Technology Elsevier – SJR 0.254, Scopus*
- *Autorovo přispění 20 %*

Article C

Krištofová P, Kubásek J, Vojtěch D, Paloušek D, Suchý J. Microstructure of the Mg-4Y-3RE-Zr (WE43) magnesium alloy produced by 3D Printing. Manuf Technol [Internet]. 2019;19(1):89–94. Available from: https://doi.org/10.21062/ujep/249.2019/a/1213-2489/MT/19/1/89

- *Manufacturing Technology Elsevier – SJR 0.254, Scopus*
- *Autorovo přispění 20 %*

Article D

Krištofová P, Roudnická M, Kubásek J, Michalcová A, Vojtěch D, Suchý J, et al. Magnesium alloy we43 produced by 3d printing (Slm). Defect Diffus Forum. 2020;405 DDF:345–50.

- *Defect and Diffusion Forum Scietific.Net – SJR 0.24, Scopus*
- *Autorovo přispění 20 %*

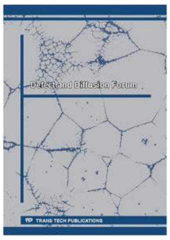

Article E

J. Suchý, L. Klakurková, O. Man, M. Remešová, M. Horynová, D. Vojtěch, D. Palou, D. Koutný, P. Krištofová, L. Čelko, Corrosion behaviour of WE43 magnesium alloy printed using selective laser melting in simulation body fluid solution, 69 (2021) 556–566. https://doi.org/10.1016/j.jmapro.2021.08.006.

- *Journal of Manufacturing Processes Elsevier – IF 5.01, Q2*
- *Autorovo přispění 60 %*

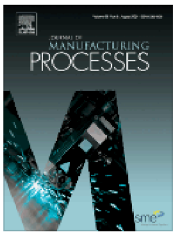

5 MATERIALS AND METHODS

5.1 Achieving the reqired mechanical properties of 3D printed material WE43

As mentioned above, the PhD thesis moves the issue of biodegradable bone implants forward. In practice, these are most often checked for compressive strength and three-point bending strength, and their values should be as close as possible to the values of the bone they are intended to support. The generally stated mechanical strength of bone in compression and three-point bending for an adult reaches the order of 210 MPa and 180 MPa. It is also necessary to mention that the internal structure of the bone is porous and each of the cavities has its purpose, as already mentioned in the introduction. From this point of view, it is important to control the geometric structure in the bone and it is not possible to rely on its uncontrolled distribution. The shape and distribution of the porosity in the bone will be controlled by the shape and density of the structured lattice. Therefore, it is necessary to achieve the material with a relative density higher than 99 %, which can be declared sufficiently homogeneous.

The values against which the quality of the processed WE43 material was assessed are based on the above-mentioned values of strength and relative density. However, before the mechanical testing itself, it was first necessary to create a printing strategy for the volumetric material to achieve. Thus, it was necessary to start with linear samples and gradually switch to a volumetric variant.

In the first phase of the tests, two series of linear samples were created. The first series contained weld deposition tracks created by different combinations of laser power and scanning speeds. The shape and continuity of the tracks were monitored using a profilometer and SEM. The aim of the experiment was to find combinations of process parameters at which the weld deposition traces were stable. This allowed us to create a process map that described the behaviour of weld deposition tracks in the context of linear density of energy, laser power and scanning speed. This provided the basis for combinations of process parameters that were used as input for testing volumetric samples. The effect of laser power on the chemical composition of the weld depositions and their microhardness was also monitored on the weld deposition samples. A chemical composition analysis was performed using EDS, and microhardness was measured by HV. This test served as initial information on the mechanical properties of the processed alloy and tested the sensitivity of the resulting microstructure to a change in the parameter that supplies the energy needed for melting to the material. From the presented hypothesis of SQ1, it follows that it is the high value of laser power that is probably responsible for the formation of Mg vapours and this will have to be reduced.

After the weld depositions tests, thin walls were produced with the same combinations of process parameters. Their width corresponded to the width of one weld deposition track. The continuity and width of the thin walls were monitored and compared with the weld deposition tracks. The width of the thin walls was measured on a cut perpendicular to the build plate using an opto-digital microscope. The recorded change in width should serve as a basis for the choice of weld deposition overlap to print the volumetric samples in future tests. The smallest manufacturable width of a stable thin wall was also identified during the test. This was additional information to help the successful transition from linear samples to volumetric samples.

The next step was the transition from weld deposition to volumetric samples. To do this, several sets of cubes were made with different combinations of laser power and scanning speed from the found process window from the weld deposition test. The overlap of the hatches was based on the width of the thin walls and its value was always at least 50 % to avoid the formation of pockets with unfused powder. The value of relative density determined on selected samples was monitored by the image analysis performed on cross-sections of selected samples. A metallographic analysis also provided the information on the shape and position of defects in the material. Based on this, it was possible to evaluate the effect of changes in process parameters and gradually approach the optimal setting of the printing strategy.

Also, the hardness value was monitored on the samples. Due to its simplicity and direct link to the mechanical strength of the material, it was possible to evaluate a large number of samples and monitor the trend of its change. The value of compressive and three-point bending strength was then monitored on selected samples. This was put into the context of microstructural analysis, where the material in the cast and extruded state was compared with the 3D printed material. It was possible to identify the main differences in the individual states responsible for the different mechanical behaviour.

When processing the material, a new filtration system was gradually developed to ensure a better removal of magnesium vapours from the process chamber. After the construction and connection of the system to the inert atmosphere circuit, it was necessary to readjust the settings of the printing strategy. The reason was to achieve a higher efficiency of the laser beam by the reduction of the amount of vapour in the process chamber. The limit for completing the optimization was to reach a value of relative density close to 100 % with guaranteed repeatability of production. Thanks to these steps (Fig 5.1), it was possible to answer the first scientific question.

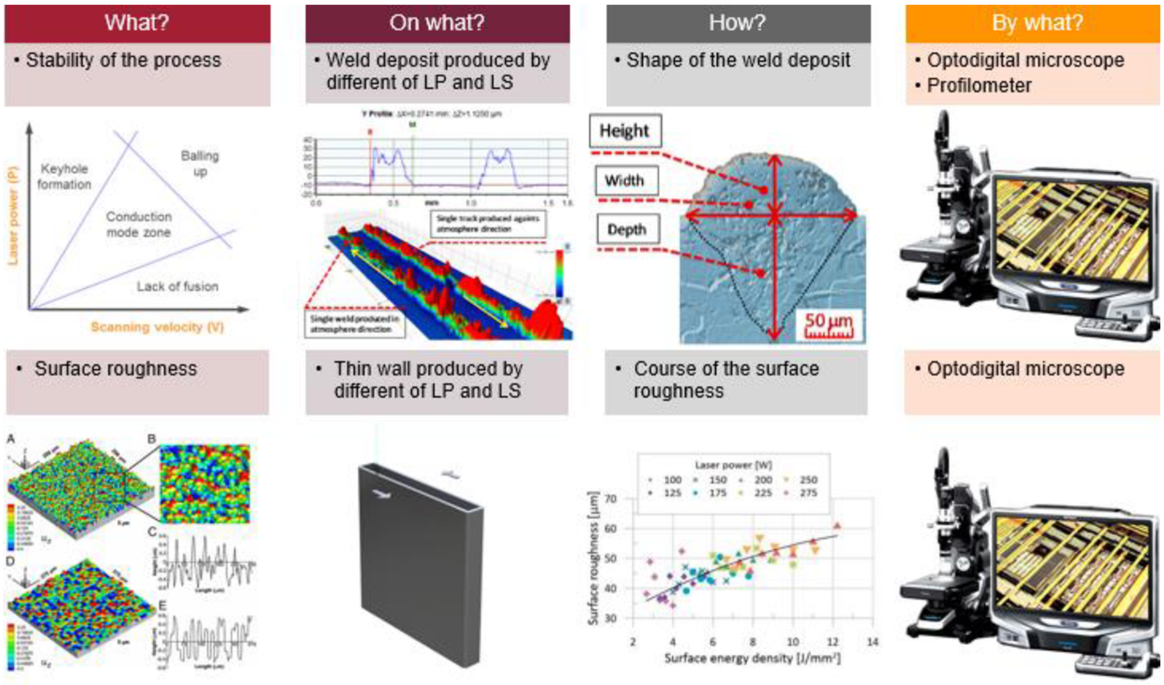

Fig 5.1 The summary of the method diagram for the first scientific question.

5.2 Corrosion behaviour of material in simulated human body environment

Another topic of the present thesis is the increase of corrosion resistance of 3D printed WE43 magnesium alloy. With conventional processing methods, the corrosion rate of the alloy ranges from 1.5 to 3.6 mm·year^{-1}, depending on the technology used. The lowest values are achieved by extrusion and, conversely, the highest ones by gravity casting. For the 3D printed material, the value of the corrosion rate in the salted simulated solution of the human body has not been determined so far. The corrosion rate requirement of biodegradable implants is 0.5 mm·year^{-1} [69]. This value can be achieved by coating the surfaces using the methods such as plasma electron oxidation (PEO), etc.

As mentioned above, there are two types of corrosion of magnesium materials - atmospheric and galvanic. Galvanic corrosion is related to the internal microstructure of the material, the distribution and size of the cathodic phases. These properties are given by the chemical composition of the alloy and its processing. Atmospheric corrosion is significantly affected by the chemical composition of the material, the properties of the corrosive environment and, last but not least, the surface quality. It was the surface quality of the 3D printed material that proved to be critically low, due to the surrounding powder fusing to the surface of the material during printing. However, the amount of fused powder should be affected by the surface temperature; therefore, it should be controllable by changing the process parameters. In this way, the corrosion rate of the 3D printed material should be reduced.

First of all, it was necessary to determine the influence of process parameters on individual types of corrosion. The surface quality of the 3D processed material, the change of which directly affects the corrosion rate, was selected as the monitored value for examining the sensitivity of atmospheric corrosion to the process parameters. For this purpose, a series of thin-walled samples was produced, the surface of which was scanned with an optical profilometer. Thin-walled samples were made by different combinations of laser power and scanning speed in correspondence with the process map dealing with the mechanical properties of the material. It was thus possible to evaluate the change in surface roughness in order to change these two main parameters.

In the following phase of the tests, the microstructure of the 3D printed material was examined and compared with the cast and extruded state. This allowed to identify differences between individual states and establish their links with individual methods of technological processing. The microstructure of the materials was monitored on metallographic cuts using light microscopy. The EDS method was used to identify the intermetallic phases and their chemical composition. By examining the microstructure of volumetric samples produced by different combinations of process parameters, the microstructure sensitivity to grain size change, chemical composition, distribution and particle shape was monitored. Based on this monitoring, it was possible to decide to what extent the galvanic corrosion can be affected by changing the process parameters.

In the last part of the thesis, an immersion test was performed to determine the corrosion rate of 3D printed material in a simulated human body environment. Several sets of samples with modified surface qualities were tested. This allowed us to determine the exact effect of surface quality on the corrosion rate of the material. In the context of the previous test of the surface quality of thin walls, it was possible to determine the effects of changing the laser power and the scanning speed on the resulting corrosion rate of the processed material.

Before and after the corrosion test, the microstructure of the material was monitored to reveal how the material corroded. The size and orientation of the grains in the material structure were monitored by EBSD. The basic chemical composition of the intermetallic phases was determined by EDS, and their distribution and shape were monitored by SEM. The exact chemical composition of the individual phases and the composition of the passivation layer after the corrosion test were determined using the XRD method. The passivation layer was also observed by SEM to determine its width and compactness. The obtained results served as a basis for a discussion over the corrosion behaviour of 3D printed material. The methodology is shown on the scheme diagram (Fig 5.2).

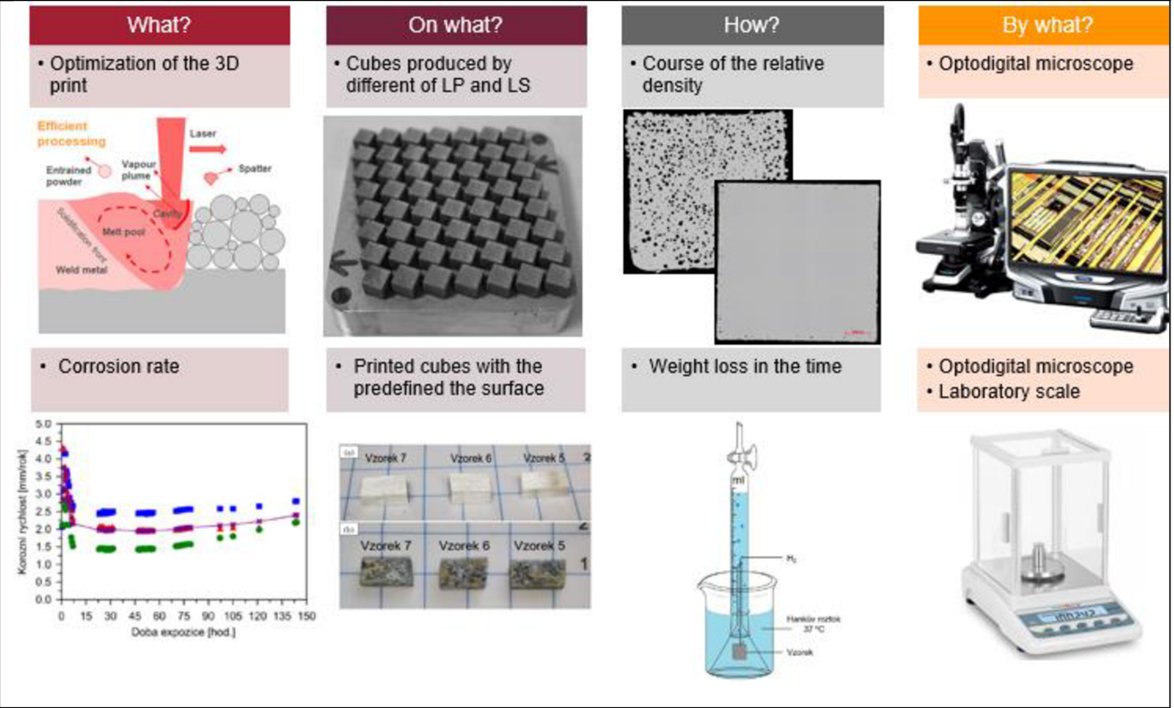

Fig 5.2 The summary of the method diagram for the second scientific question.

5.2.1 Powder analysis

The powder entering the selective laser melting process has a significant effect on the production process itself. Therefore, it was necessary to validate its shape and distribution to determine the minimum thickness of the deposited layer. The particle shape was monitored and evaluated using a DSX510 opto-digital microscope (SEM).

The required particle shape is predominantly spherical to achieve a uniformly deposited layer (Fig 5.3). The powder distribution was validated using a Horiba LA-960 laser analyser.

The powder must contain a fine and coarser fraction to achieve a high density of the deposited layer. If the powder contains too large particles, it passes through a vibrating screen with the required permeability.

The chemical composition of the powder was controlled by ICP-OES method. The chemical composition of the powder could thus be related to the metallographic phases formed during the SLM process. In addition, it was possible to control the quality of the recycled powder, which could be subject to degradation due to evaporation of the magnesium matrix during printing.

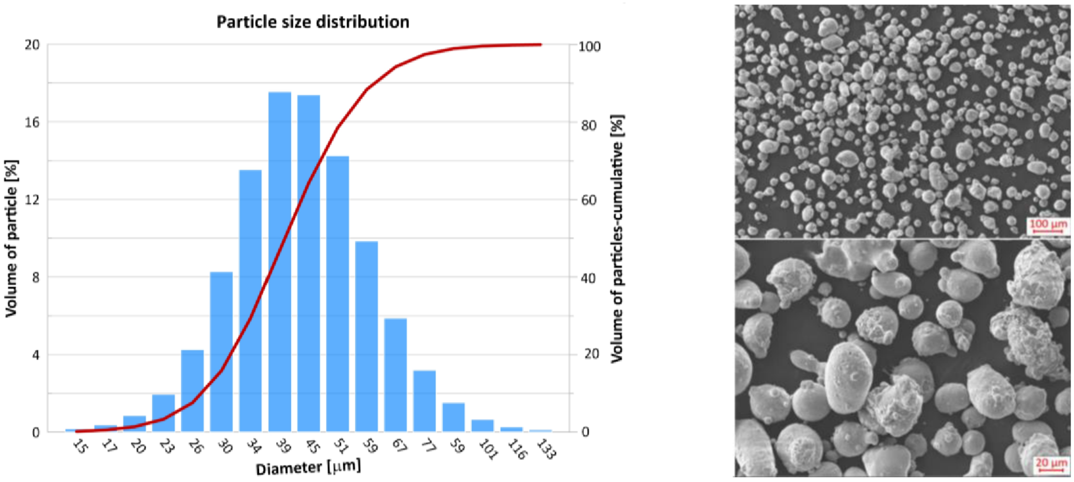

(a) (b)

Fig 5.3 Powder distribution for 3D printing (a) and SEM photographs of particle shape (b).

5.2.2 Sample printing

All samples were produced on a SLM 280^{HL} device equipped with a YRL-400W laser with a Gaussian profile with a focus of 82 µm and a wavelength of 1060 nm. The oxygen value in the production chamber was kept below 0.1 % by a constant flow of argon 5.0. Based on the state of the art, a build plate preheating of 120 ° C was chosen. The build plate was machined from WE43 alloy casting. The samples were produced directly on the build plate. The thickness of the deposited layers was chosen based on the analysis of the distribution of the input powder.

Samples for the weld deposition test were made on magnesium strips attached to the grooves in the build plate using three M4 screws. The strips inserted in this way were removable and after the production of weld deposition samples, their cuts could be analysed without having to disrupt the build plate. The upper surface of the strips was aligned with the plane of the build plate for creating of the uniform powder layer. Weld deposition tracks were printed as contours of a rectangle with a floor plan of 10 x 2 mm. In this way, it was possible to evaluate the weld deposition tracks in and against the flow direction of the inert atmosphere. The thin-walled samples were one weld deposition track wide. Their floor plan was a rectangle measuring 10 x 2 mm and was identical to the floor plan in the weld deposition track test. Thin-walled samples were built to a height of 10 mm directly on the build plate. The volumetric samples were cubes of 8 x 8 x 8 mm.

Thin-walled and volumetric samples were separated from the build plate with a band saw and an isopropyl alcohol-cleaned pad.

5.2.3 Geometry analysis of weld depositions and thin walls

The weld depositions were printed on a build plate with strips made of WE43 alloy (Fig 5.4). The weld depositions were printed in the direction and against the direction of the inert atmosphere flow. The weld deposition pairs were compared to determine the effect of inert atmosphere on the production process. The geometry of the weld deposition tracks was evaluated in two steps. The first step was the use of a ConturGT-X optical profilometer (Bruker Corporation, Billerica, MA, USA) to scan the height and width of the weld deposition track. When evaluating the height of the weld depositions, the data were adjusted with a Gaussian filter to eliminate waviness and inclination. The surface of the strip, on which the weld depositions were printed, was used as a reference plane. The resulting width and height of the weld deposition were determined as the average value from the measured weld deposition profile. The measurement error with an optical profilometer was 3 μm.

The second analysis divided the weld deposition slice into halves. The slice was then embedded in resin and subjected to metallographic wet grinding (wetted in ethanol) and polished with diamond pastes of 3 and 0.07 μm. The resulting metallographic cut was subsequently etched by Nital to highlight the boundaries of the weld depositions. The sample thus prepared was observed with a DSX510 opto-digital microscope (Olympus, Tokyo, Japan) to determine the depth of the weld deposition.

The obtained results were divided according to their similar behaviour into several categories, from which a process window for printing WE43 alloy was created. The linear density of energy (5.1) was used as a comparison value).

$$E_L = \frac{Lp}{Ls \cdot Lt}, \tag{5.1}$$

where Lp is laser power [W], Ls is the scanning speed [$mm \cdot s^{-1}$] and Lt is the thickness of the deposited layer [mm].

The width of the thin walls was determined from metallographic cuts in the same way as the depth of the weld depositions. The difference was in determining the overall width of the thin wall. This was defined as the average of ten measurements.

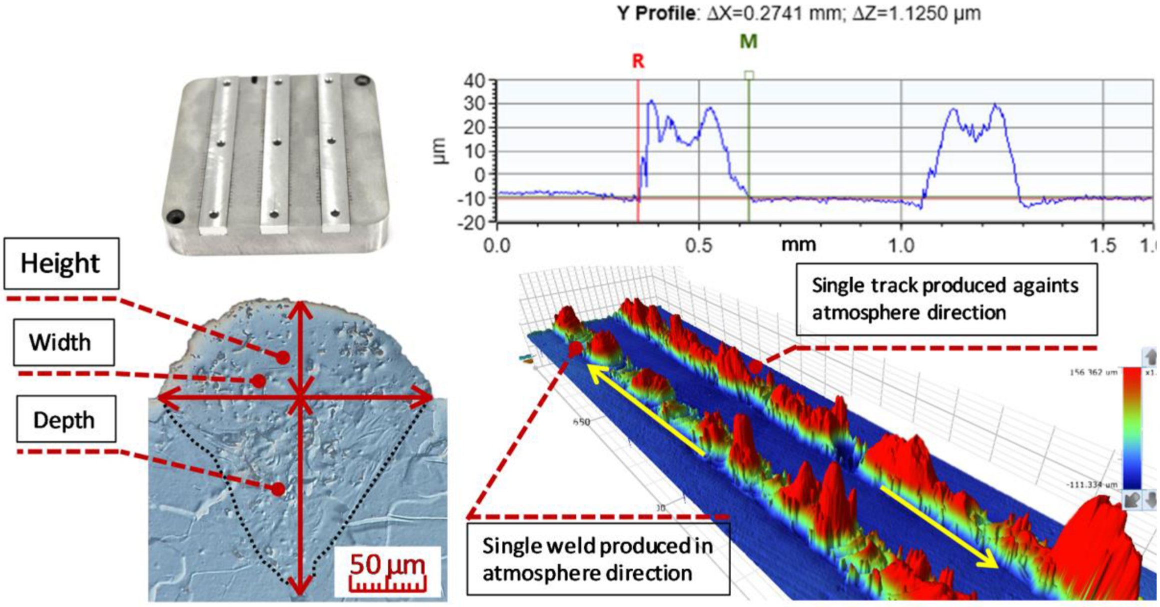

(a) (b)

Fig 5.4 Scheme for determining the depth of the weld deposition from the metallographic cut (a) and a record of the measurement of the width and height of the weld deposition by the profilometer (b). In the upper left corner, see the build plate with inserted slices for printing the weld depositions.

5.2.4 Measurement of surface roughness

The surface roughness of the thin walls was measured on the side of the thin wall (Fig 5.5) with a ContourGT-X optical profilometer (Bruker Corporation, Billerica, MA, USA). The evaluated site had an area of 9x1 mm. Waviness and inclination were removed from the scanned data using Gaussian filters. Due to the amount of powder fused to the surface of the thin walls, part of the data was mathematically reconstructed in Vision6464bit 5.60 (Bruker Corporation, Billerica, MA, USA) with a 5th degree polynomial. The total surface roughness was then evaluated according to Equation 5.2.

$$Ra = \frac{1}{n}\sum_{i=1}^{n}|z_i| = \frac{|z_1|+|z_2|+\cdots+|z_n|}{n} \tag{5.2}$$

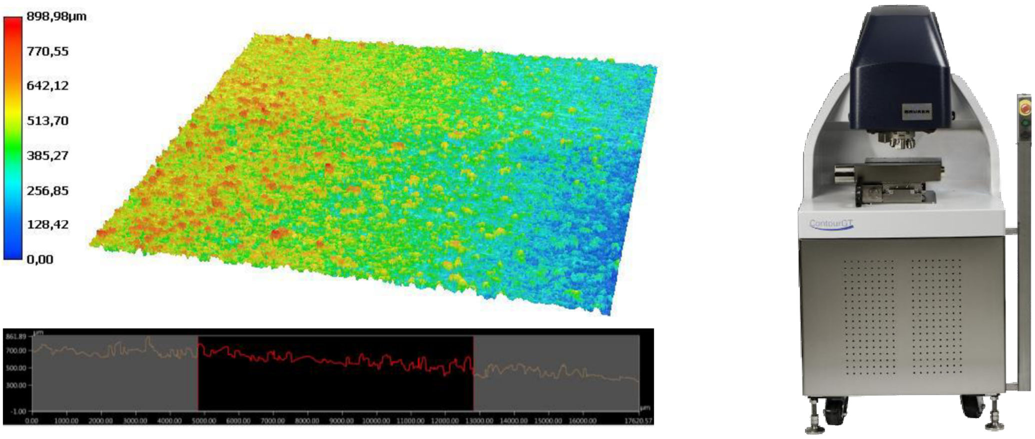

(a) (b)

Fig 5.5 Example of scanned region and its evaluation (a) with ContourGT-X measuring device (b).

5.2.5 Analysis of chemical composition and microstructural description

The aim of the analysis was to clarify the processes that affect 3D printed material. The analysis of the chemical composition of the samples was always performed on metallographic cuts prepared by wet grinding with possible polishing with diamond pastes. The chemical composition of the samples was mapped by local EDS microanalysis (Fig 5.6) using a dispersion spectrometer (Oxford Instruments, Oxford, UK), which was equipped with a TESCAN LYRA3 XMH electron microscope. The voltage used was 20 kV and the beam intensity was set to 14. The measurement error was ± 0.5 at % depending on the atomic number of the analysed element. The analysis was used to identify the main elements that made up the individual phases in the material.

The Rigaku SmartLab 3 kW X-ray diffractometer with a CuKα anode in BraggBrentano beam geometry was used to determine, in more detail, the chemical composition of the phases in the material. Diffractograms were evaluated using PANalytical X'Pert HighScore Plus software using 2012, COD 2011 and PDF 2 databases.

The directionality of the grains in the material and their size were evaluated by electron backscattering diffraction (EBSD). Samples for this analysis were polished in a Leica TIC3X Ar ion polisher to remove any artificial surface deformation. EBSD data were acquired through an EDAX Digiview 5 detector in a 260x282 μm array with a 0.4 μm pitch between pixels in a hexagonal arrangement. No filtering was applied during postprocessing.

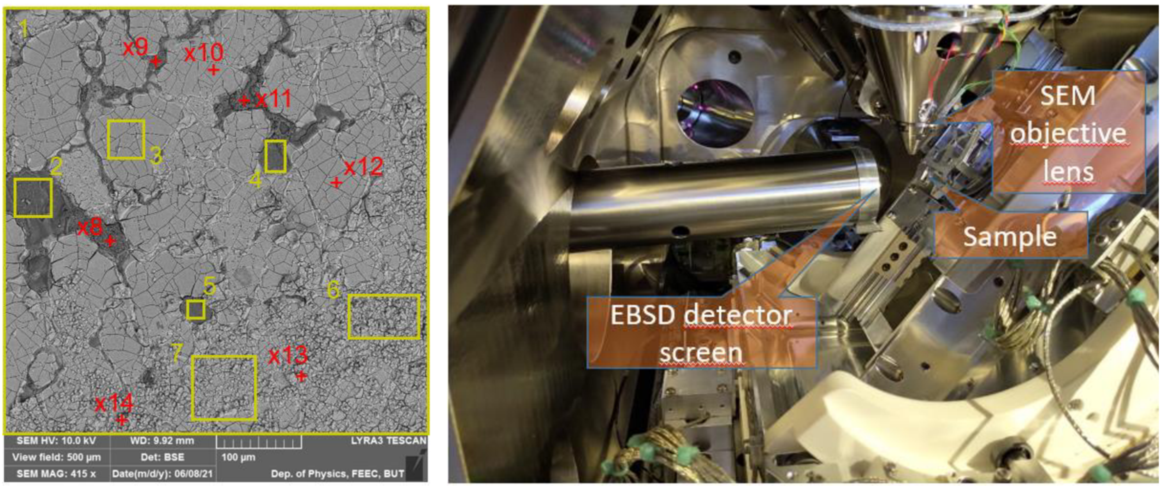

(a) (b)

Fig 5.6 Measurement of local chemical composition using EDS (a) and setting of measuring apparatus for EBSD method (b).

5.2.6 Hardness measurement

Determination of hardness of the 3D printed material served to provide a basic description of its mechanical properties. The Duramin-100 AC3 hardness tester (Struers, Detroit, Cleveland, OH, USA) with fully automatic adjustment and a wide load range was used to classify the hardness of the weld depositions. Microhardness was measured on metallographic cuts in two series. The first one was made in the axis of the weld deposition, perpendicular to the build plate and the other parallel to the build plate just below the surface of the material. The hardness measurement method was chosen according to Vickers HV0.01. The aim of the method was to determine the influence of process parameters on the hardness of the material.

The hardness of the samples for mechanical tests was tested with a Future-Tech FM-700 hardness tester with a load of 100 g and the interval of 10 s. The measurement was again performed on a metallographic cut. The resulting hardness was determined as the average of ten measurements.

5.2.7 Analysis of porosity

Porosity was monitored on metallographic cuts of cubes produced by different combinations of process parameters. The choice of process parameters was made on the basis of previous tests and a critical search. The aim of the test was to find a combination of process parameters allowing to print samples with a relative density close to 100 % (Fig 5.7).

Porosity in the samples was observed with a DSX510 opto-digital microscope (Olympus, Tokyo, Japan) on a cross-section perpendicular to the build plate. The evaluation was performed by image analysis (ImageJ, National Institute of Health) with a resolution of 3 μm. From the evaluated data, a process window was subsequently created describing the relationship of the relative density of the samples to the change of selected process parameters. The volumetric density of energy (5.3) was chosen as a comparison value.

$$E_V = \frac{Lp}{Ls \cdot Hd \cdot Lt}, \tag{5.3}$$

where Lp is the laser power [W], Ls is the scanning speed [$\mathrm{mm \cdot s^{-1}}$], Hd is the hatch distance [μm] and Lt is the layer thickness [mm].

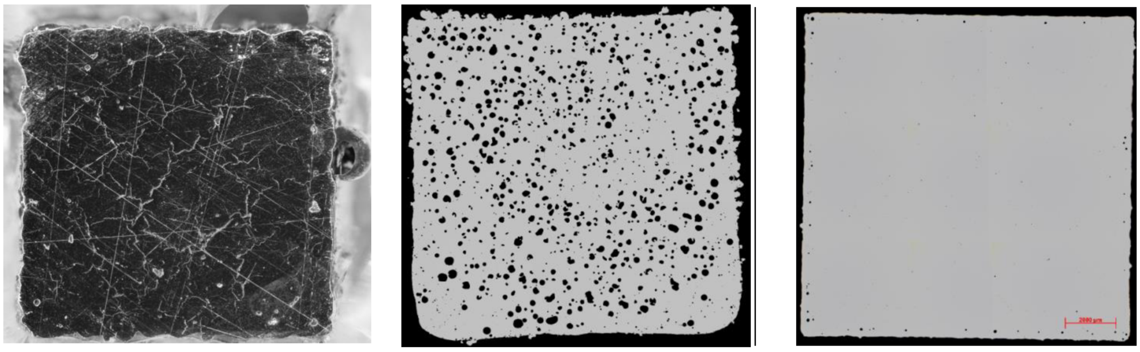

(a) (b) (c)

Fig 5.7 Development of defects in the material depending on the change of process parameters: (a) temperature cracks caused by a high temperature gradient; (b) porosity in the material caused by trapping superheated gas particles; (c) a sample with a relative density of 99.8 %..

5.2.8 Determination of compressive and flexural strength

The aim of the test was to determine the basic mechanical properties of 3D printed material. Compressive strength and three-point bending (flexural) strength tests were performed on a universal loading device LabTest 5.250SP1-VM. The resulting strength curves were generated as the average of three measurements. The samples created for the compressive tests were separated from the printed sample and their size was 7x7x7 mm. The test was performed at room temperature with a strain rate of $0.001 s^{-1}$. The samples created for the three-point bending test were separated from the printed sample and their size was 3x5x18 mm. The bending force was applied at a distance of 10 mm from the sample attachment point. Mechanical tests were also performed on the samples of cast and extruded WE43 material. The obtained results were compared with the results of testing of 3D printed materia.

5.2.9 Immersion test

The purpose of the immersion test was to determine the corrosion rate of the 3D printed material depending on the surface quality of the samples. The immersion test also examined the resulting passivation layer and the main corrosion products. The reason was to clarify the way in which 3D printed material corrodes.

A combination of process parameters was used to produce the samples, which reached the highest value of relative density. The test was performed on 12 samples divided into 4 groups designated as-built, SiC120, SiC500 and SiC4000. The designation of the group corresponded to its processing before the corrosion test. The surface of the SiC120, SiC500 and SiC4000 groups was ground (wetted with ethanol) with a suitable sandpaper, while the as-built group was in the untreated state. The samples were then cleaned in an ethanol-filled ultrasonic cleaner for 10 minutes and stored with silica gel.

During the immersion test, the hydrogen concentration was recorded to determine the corrosion rate according to [78, 79]. Hydrogen release during the test was possible as a result of the chemical reaction (5.4). Therefore, the test consists in collecting the released H_2 and verifying its amount. Based on this measurement, the amount of dissolved alloy can be directly determined.

$$Mg + 2H_2O \rightarrow Mg_2^+ + 2OH^- + H_2 \tag{5.4}$$

The volumetric samples were placed in a corrosion cell filled with a solution simulating the human body environment (HSBF) with the temperature constantly maintained at 37 °C (Fig 5.8). The amount of released H_2 was directly deducted from the values designated on the burette. The chemical composition of the solution was not changed during the test. However, to compensate for the evaporation, the volume of the solution was kept at 400 ml. At the end of the test, the samples were rinsed in ethanol, dried, and weighed.

The chemical composition of HSBF was prepared with chemicals of analytical purity (Lachner, Neratovice, Czech Republic) according to the ISO 11845 standard without the addition of glucose. The pH of the solution was measured before and at the end of the test. The corrosion rate was calculated according to the following relationship [79, 80]:

$$i_g = \frac{H_2 \cdot \frac{Mr_{Mg}}{Mr_{H_2}}}{D \cdot A \cdot t}, \qquad (5.5)$$

where H_2 is the amount of hydrogen released [ml], $MrMg$ and MrH_2 are the molar masses of magnesium and hydrogen [$g \cdot mol^{-1}$], D is the density of WE43 alloy [$g \cdot mm^{-3}$], A is the total sample area [mm^2] and t is the time of issue [year].

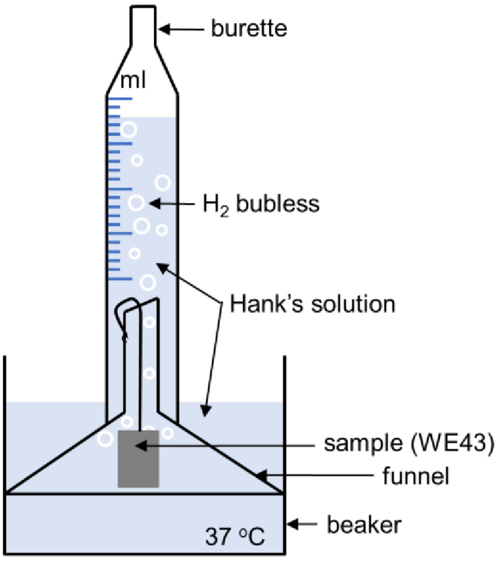

(a)

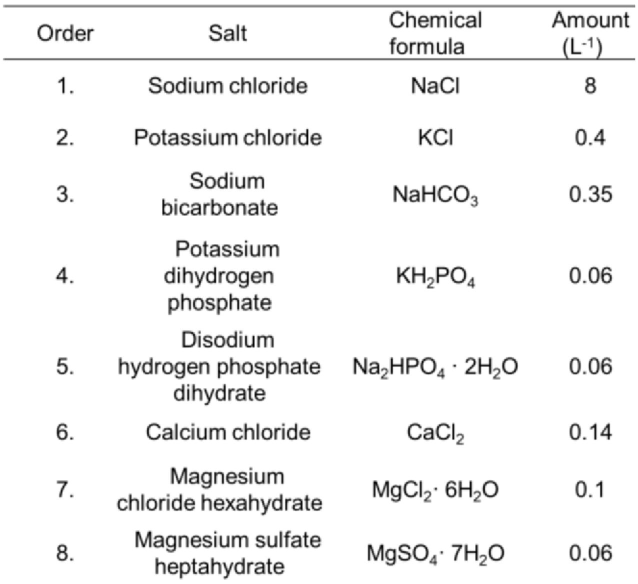

Order	Salt	Chemical formula	Amount (L^{-1})
1.	Sodium chloride	$NaCl$	8
2.	Potassium chloride	KCl	0.4
3.	Sodium bicarbonate	$NaHCO_3$	0.35
4.	Potassium dihydrogen phosphate	KH_2PO_4	0.06
5.	Disodium hydrogen phosphate dihydrate	$Na_2HPO_4 \cdot 2H_2O$	0.06
6.	Calcium chloride	$CaCl_2$	0.14
7.	Magnesium chloride hexahydrate	$MgCl_2 \cdot 6H_2O$	0.1
8.	Magnesium sulfate heptahydrate	$MgSO_4 \cdot 7H_2O$	0.06

(b)

Fig 5.8 HSBF (b) Schematic representation of the capture of released hydrogen during the immersion test (a) and HSBF chemical composition table (b).

6 RESULTS

Only the main results are referred to in the chapter. The full text of the results is summarized in the attached publications.

6.1 Achieving the required mechanical properties of 3D printed material WE43

6.1.1 Analysis of the shape and continuity of weld deposition tracks

The first test focused on linear samples, which served as a basis for creating a strategy for printing volumetric samples. The weld depositions were produced in a wide range of laser power and scanning speeds. The range of laser powers and scanning speeds was 100-400 W and 100–800 $mm \cdot s^{-1}$ and 25 W and 50 $mm \cdot s^{-1}$ respectively. By comparing the results from the measurement of the geometry of the weld depositions in the direction and against the flow direction of the inert atmosphere, no significant deviations in the shape and continuity of the weld depositions were found. For this reason, the work only considered the weld depositions formed in the direction of flow of the inert atmosphere. The results of this chapter are incorporated in Article A.

The measurement results were gradually divided according to several criteria. One of them was the classification according to the value of linear energy with which the weld depositions were produced. This created three areas whose boundaries, however, partially intersected precisely because of the calculated values of linear energy density of (Fig 6.1). The first defined area (2.5–8 $J \cdot mm^{-2}$) did not have sufficient energy density to form stable weld deposition tracks. The powder was only partially melted, and this often resulted in agglomerations of material that were not even fused to the build plate. In the case of fusing the powder to the build plate, a balling effect with a discontinuous weld deposition track occurred very often. The second area (13–80 $J \cdot mm^{-2}$) was characterized by wide and deep weld depositions. The melt pool was wide and unstable, which was reflected in the shape of the weld deposition tracks. The reason for this behaviour was probably the high value of linear energy. The third area (7–13 $J \cdot mm^{2}$) contained continuous weld deposition tracks with a stable shape. This was also reflected in the smaller range of the dimensions of the weld deposition tracks.

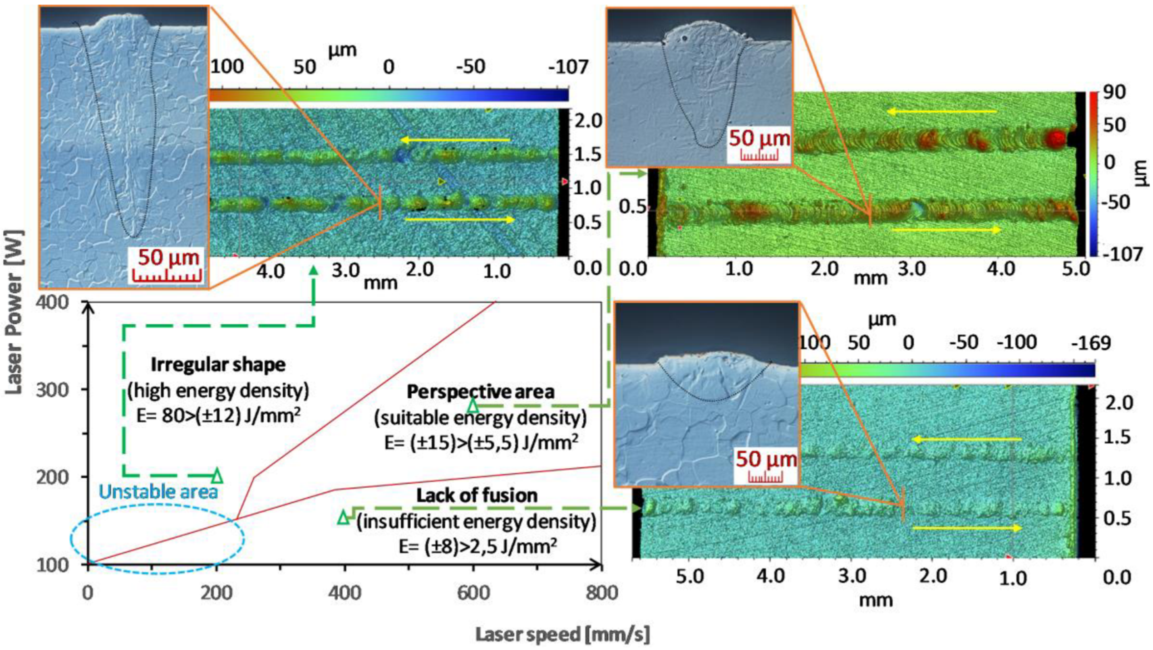

Fig 6.1 WE43 magnesium alloy process window diagram based on the behaviour of weld deposition tracks.

For complete knowledge of the geometry of the weld depositions, the depth of the weld deposition tracks was determined from the metallographic cuts. The width and depth of the weld depositions gradually decreased with decreasing value of linear energy density. From among the monitored process parameters, the laser power had a greater effect on the resulting shape of the weld deposition tracks (Fig 6.2). The behaviour of the depth of weld depositions from metallographic cuts corresponded to the observations on the optical profilometer.

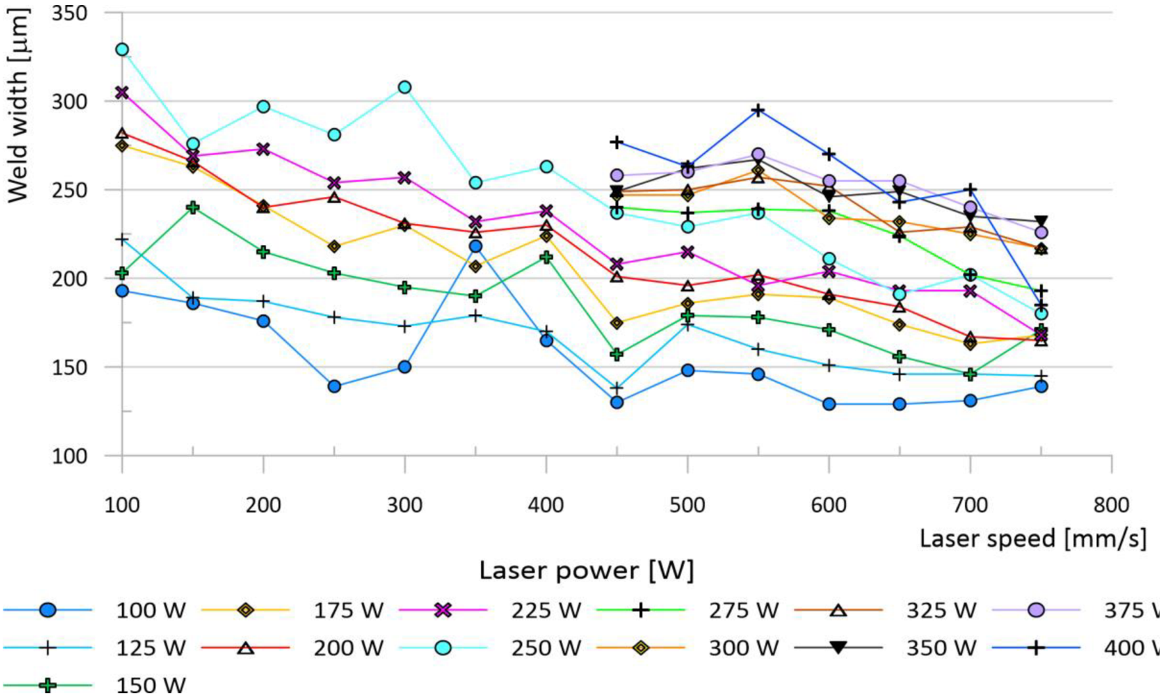

Fig 6.2 Dependence of the width of the weld depositions on the change of laser power and scanning speed.

The unstable area in Fig 6.1 deserves special attention. This area was more sensitive to changes in process parameters than other areas. Even a change of process parameters by one step significantly changed the behaviour of the weld deposition. The results from areas with high and insufficient value of linear energy mixed here. The melt pool behaved unstable. Many weld depositions showed melt spattering and subsequent solidification on the surface of the weld depositions (Fig 6.3). The height of the weld depositions was the least affected being changed only in the order of micrometres.

The area with a high value of linear density of energy contained weld depositions with penetration even above 600 μm and the largest widths of all areas. Several weld depositions in their root contained several pores, which reached a size between 50-75 μm. Smaller pores appeared in weld depositions from the high-energy area quite often along the weld deposition boundaries. The spherical shape of the pores proves that it is probably a tapped gas (vapours). The area with laser powers of 300–400 W and 100–400 mm·s^{-1} contained such irregular and deep weld depositions that it was no longer analysed in detail.

The weld depositions from the perspective area reached a width of 200–250 μm, a depth of 200–300 μm and a height of 20–40 μm.

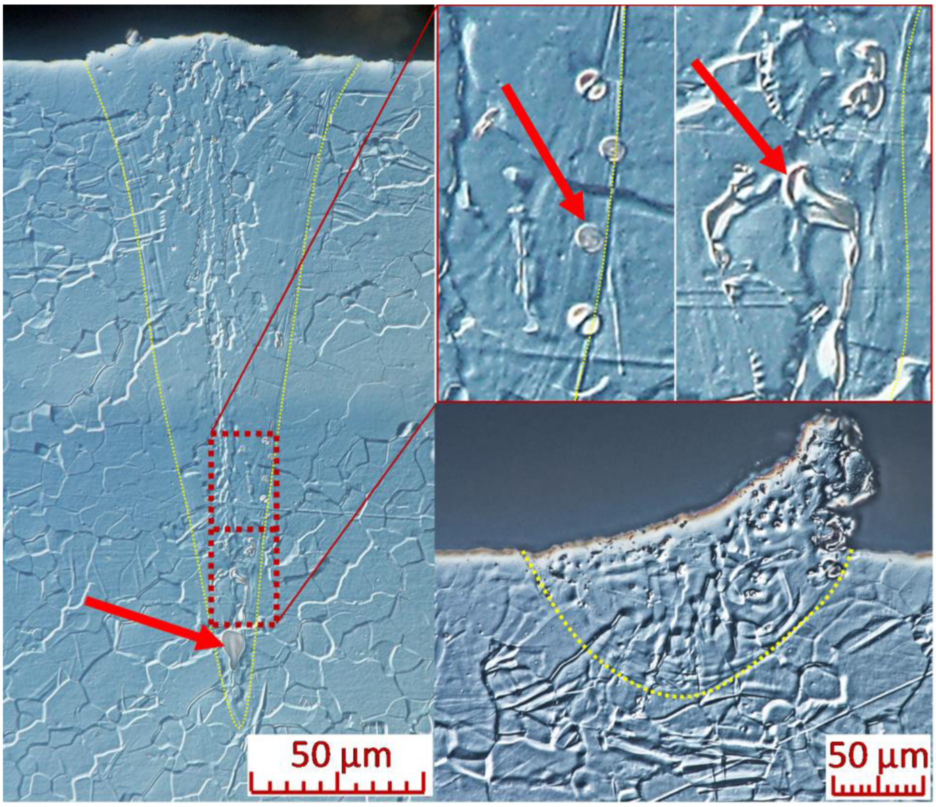

(a) (b)

Fig 6.3 Key-hole porosity at the root of the weld deposition and smaller spherical pores along the weld deposition boundary (Lp 200 W, Ls 100 mm·s^{-1}) (a) and unstable weld deposition (Lp 125 W, Ls 150 150 mm·s^{-1}) caused by melt spraying and its subsequent solidification.

6.1.2 Influence of parameters on chemical composition and microhardness of weld depositions

Due to the initial estimation of mechanical properties, the microhardness of the weld depositions was checked. It was obtained as the average of all measurements on a given sample. The results were plotted against the linear density of energy and laser power (Fig 6.**4**). The power of the laser was chosen because, from among the monitored process parameters, it showed the greatest influence on the behaviour of weld depositions and, at the same time, from the first scientific question it follows that it will have to be manipulated to reduce the amount of vapour generated during printing.

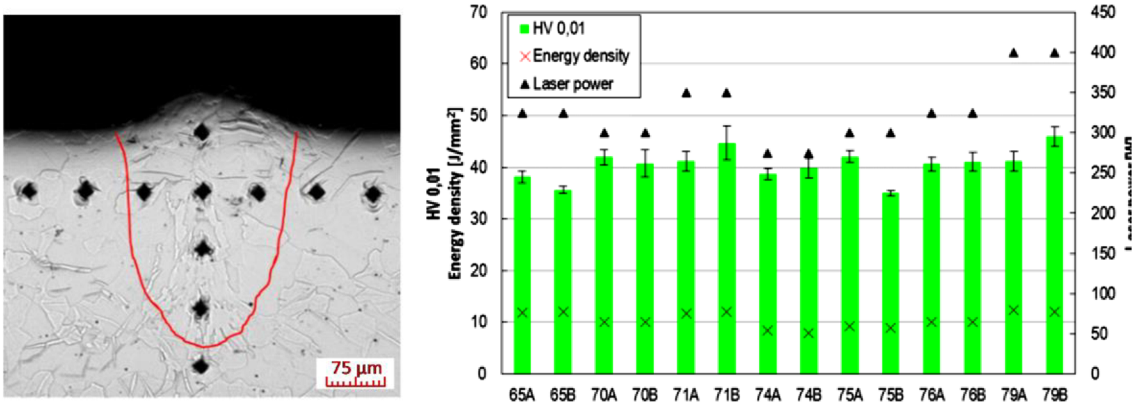

(a) (b)

Fig 6.4 Example of measurement of microhardness of weld depositions with highlighted weld deposition boundary (a) and plotted dependence of average value of microhardness on selected process parameters.

At the same time, a metallographic cut of selected weld depositions was observed in order to find possible deviations in the microstructure. Therefore, the local chemical composition of the weld depositions was monitored (Fig 6.5**Chyba! Nenalezen zdroj odkazů.**). The microstructure of the weld depositions consisted mainly of coarse dendrites of the solidified solution. In the local areas, mostly in the corners of the weld deposition, it was possible to observe precipitated fine grains of eutectic based on Mg–Y–Nd alloy WE43. The weld depositions also occasionally contained Si compounds. The intermetallic phases found contained a large amount of trapped oxygen. By comparing the results obtained from different weld depositions, it was not possible to find any influence of the process parameters on the distribution, shape or merger of the phases arising in the material. Although WE43 contains a relatively high Zr content, its chemical compounds have not been found in the weld depositions. The results of this chapter are incorporated in Article A.

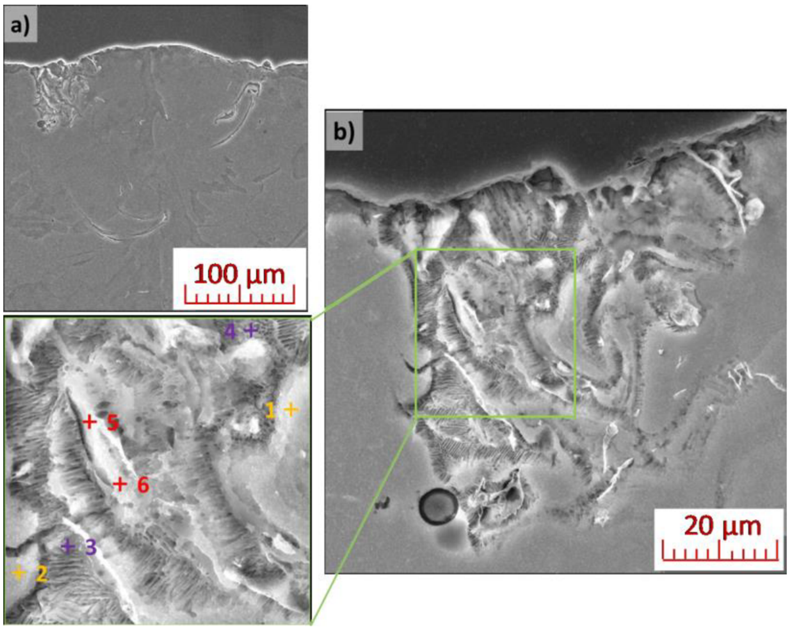

Fig 6.5 Internal structure of the weld deposition (Lp = 325 W, Ls = 650 mm·s^{-1}): (a) macro view and (b) agglomeration detail in the upper left corner of the sample.

6.1.3 Comparison of weld deposition tracks and thin walls

To obtain a more realistic idea of the weld deposition width when printing a volumetric sample, thin-walled samples were created in the area where the weld deposition tracks appeared to be stable. The thin walls were one weld deposition wide. However, this weld deposition was layered on top of each previous layer, thus achieving at least a partial remelting effect. This led to an increase in width. The values of the thin wall widths were subject to a large range of values due to the amount of powder fused to their surface. Nevertheless, on average, an 18 % increase in the width of the thin walls was observed compared to single weld deposition tracks. Although the width of the melt pool was increased for the thin walls, it was still subject to the same behavioural trend depending on the process parameters as the weld depositions (Fig 6.6).

Due to the accumulation of heat in the material by remelting, the value of the energy density for printing a stable weld deposition (thin wall) was reduced from 7 J·mm^{-2} to 4.5 J·mm^{-2}.

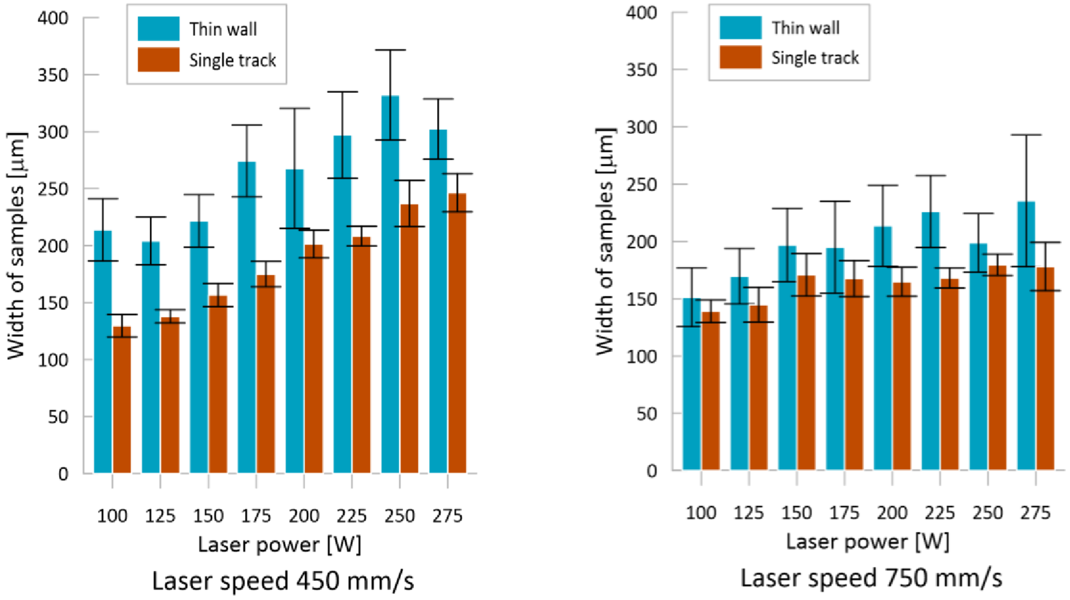

(a) (b)

Fig 6.6 Development of the difference in the width of thin walls and weld depositions depending on the laser power and selected scanning speeds: Ls 450 mm·s^{-1} (a) and Ls 750 mm·s^{-1} (b).

6.1.4 Printing of the volumetric samples

The design of process parameters for printing of volumetric samples was based on the defined areas of the weld deposition and thin wall test. In the first phase, several series of volumetric samples were produced with different combinations of process parameters. The porosity and defects in the material were monitored on the cuts of these samples. Thanks to this, it was possible to evaluate the influence of the monitored process parameters on the behaviour of the material. However, printing of volumetric samples was accompanied by several problems.

One of them was a relatively large number of process emissions that appeared during the print. The used filtration system did not manage to sufficiently remove the generated vapours, which led to the accumulation of black smoke in the process chamber of the 3D printer. Many of the samples produced contained defects observable with the naked eye (Fig 6.7). Other samples, despite a porosity value above 99 %, contained cracks that resulted in low strength values during loading. Unfused powder particles and, occasionally, also lack of fusion formed at the interface of the individual printed layers, were also found in the structure of the material. The increasing value of the volume density of energy led to a reduction of the mentioned defects in the samples. The lowest porosity rates (0.2 %) were achieved with Lp = 250 W, Ls = 450 mm·s^{-1} and Hd = 80 µm. However, the structure of this sample still contained a number of defects

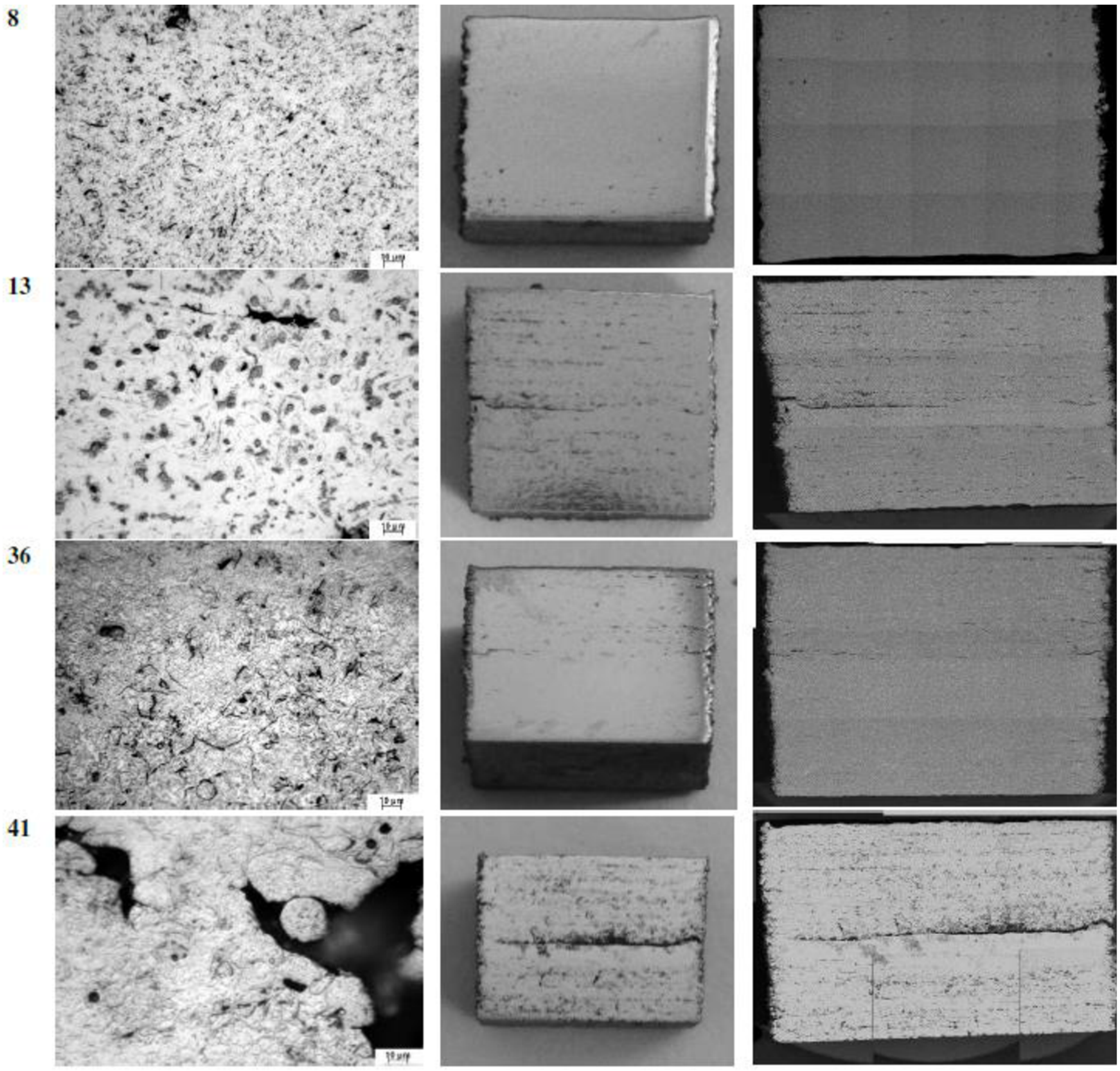

Fig 6.7 Macrostructural studies of selected samples containing a number of defects (8 – Lp=250 W, Ls=450 mm·s^{-1}, Hd=80 µm; 13 – Lp=250 W, Ls=700 mm·s^{-1}, Hd=80 µm; 36 – Lp=275 W, Ls=450 mm·s^{-1}, Hd=90 µm; 41 – Lp=275 W, Ls=700 mm·s^{-1}, Hd=90 µm).

The samples thus produced were selected to measure hardness and compressive strength. The obtained results did not show a significant effect of process parameters on the hardness of the material, which is mainly due to the high temperature gradient during the printing process.

Porosity in the material proved to be a significant factor influencing the compressive strength (Fig 6.8). By reaching the value above 1 %, the material lost much of its strength. The measured data prove the dependence of the samples on defects in their microstructure. The best strength values were achieved in a sample with a porosity of 0.2 %, while the worst ones were achieved in a sample with a porosity of 3.5 %. The overall testing results are summarized in the final table (**Tab 6.1**). The results of this chapter are incorporated in Article B.

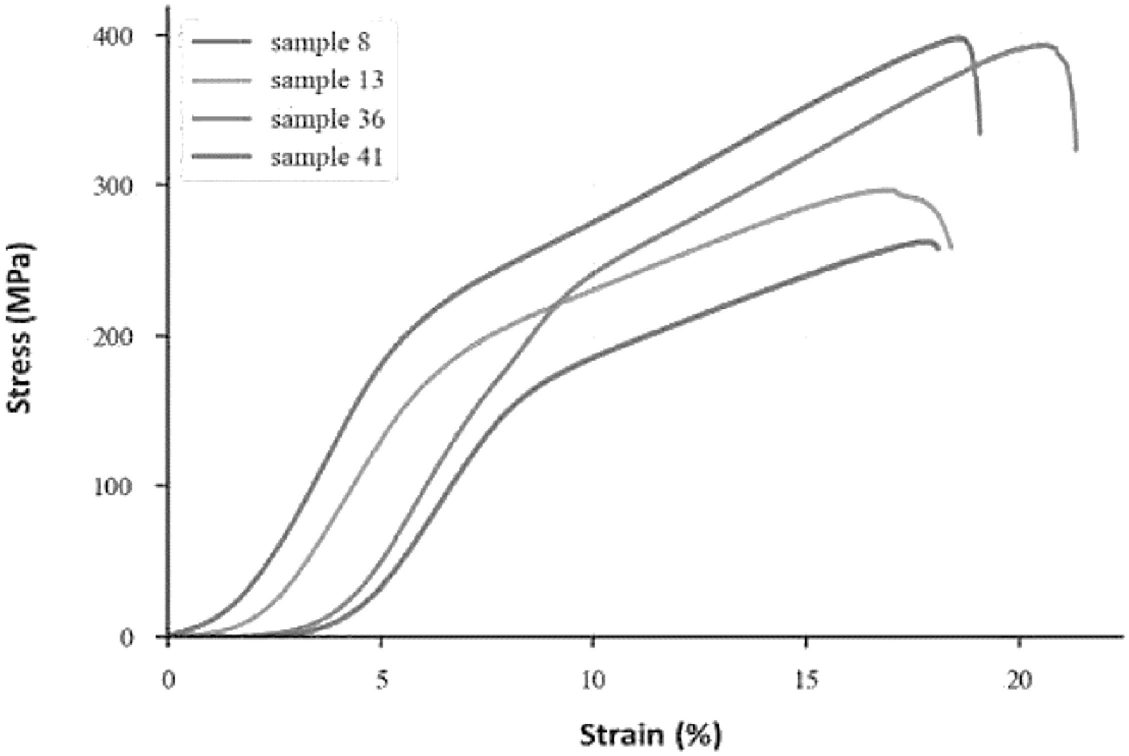

Fig 6.8 Record of compression test measurements of 3D printed material WE43.

Tab 6.1 Summary of results from initial measurements of hardness and compressive strength of volumetric samples.

Sample	**8**	**13**	**36**	**41**
Laser power [W]	250	250	275	275
Scanning speed [mm·s^{-1}]	450	700	450	700
Hatch distance [µm]	80	80	90	90
Porosity [%]	0.2	1.5	1.0	3.5
HV0.1	88±6	85±6	86±6	81±7
Compressive yield strength [MPa]	208	175	220	165
Ultimate commpressive strength [MPa]	395	296	386	261

6.1.5 Internal structure of 3D printed material and its mechanical properties

The samples with the highest relative density were divided, embedded in resin and subjected to metallographic grinding. The resulting cuts were subsequently observed with an electron microscope. Samples of cast and extruded material were prepared and evaluated in the same way. By comparing the results, differences in the microstructure of the material caused by different production methods were revealed (Fig 6.9).

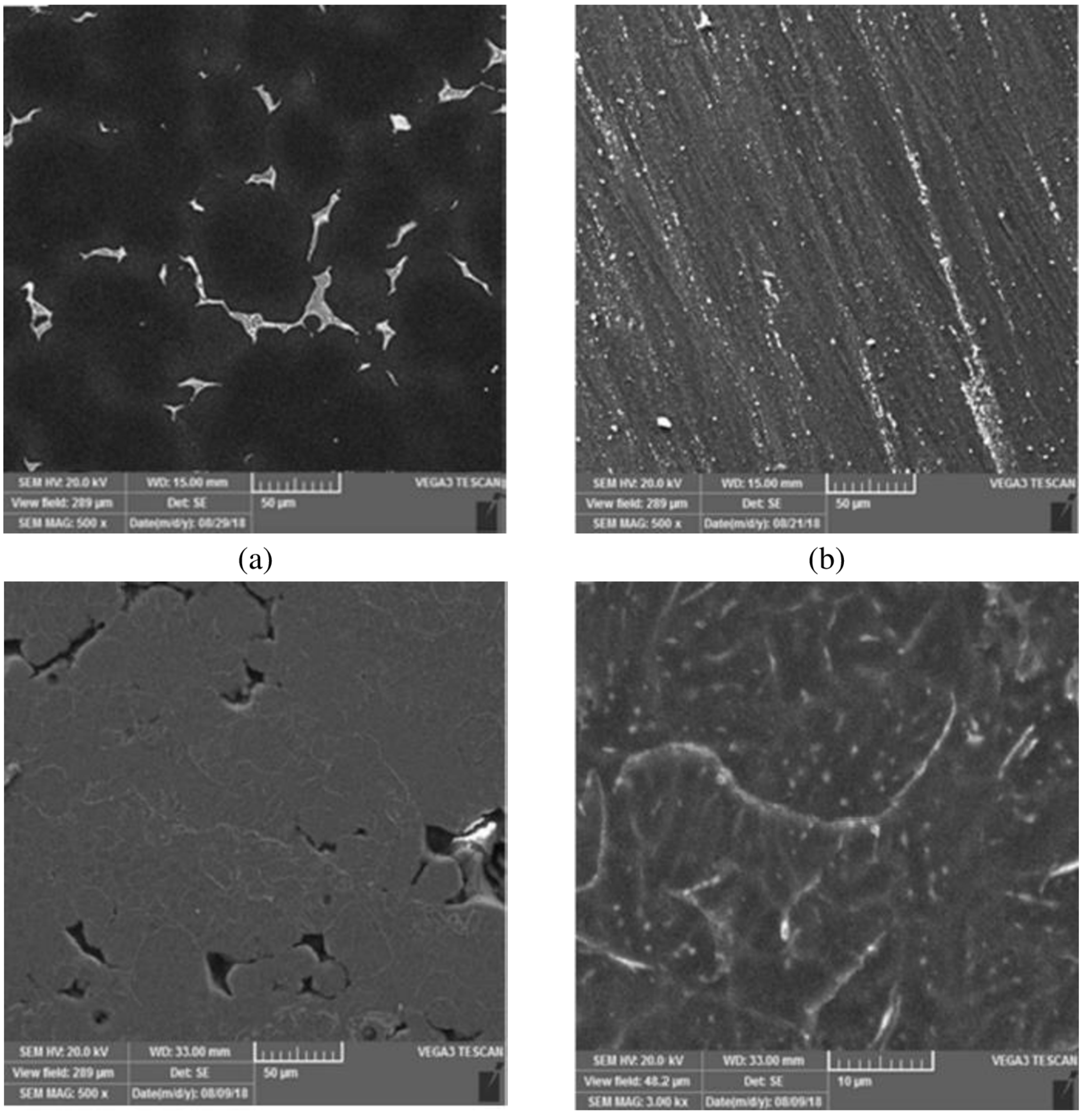

(a) (b)

(c) (d)

Fig 6.9 SEM images of WE43 magnesium alloy cuts: (a) cast state; (b) extruded state; (c, d) 3D printed state.

The cast material consisted mainly of a solid α-Mg solution and discontinuous interdendritic eutectic phases. The method of cooling the material in the cast state made it possible to achieve interdendritic phases with an average width of up to 50 µm. The dendritic phases contained Mg–Nd–Y compounds. The same compounds were observed in the extruded state. However, they did not reach such dimensions as they were disrupted by extrusion and pulverized into fine particles. The directivity corresponding to the direction of extrusion was evident on the particles. The microstructure of the 3D printed material consisted of α–Mg and interdendritic phases. Due to the rapid cooling process, the microstructure was very fine and the interdendritic phases reached an average width of only 3 µm. The microstructure of the 3D processed material was the finest of the examined states. However, the processed material contained a number of defects. Cut – outs of spherical particles were observable, at the interface of which discontinuities were formed with the remaining material; these were reflected in the overall porosity of the material.

EDS mapping of cuts revealed a high richness of eutectic phases on RE elements and oxygen. The 3D printed material contained significantly more bound oxygen in the α – Mg matrix compared to the cast and extruded state. Oxygen in the 3D printed material was bound mainly in the area of pores and welds (Fig 6.10). In the matrix of the material, oxygen was also excreted in the form of flakes, which were probably the remnants of the surface layer of oxides on the input material. This corresponds to the identified chemical composition on the surface of unfused particles inside the material. An example of such a chemical composition is given in **Tab 6.2**.

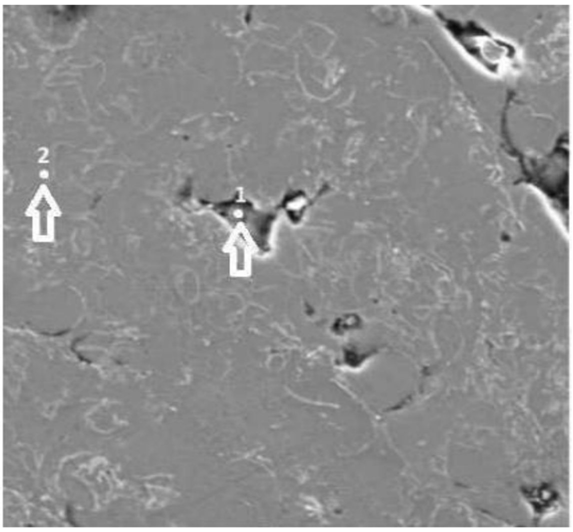

Fig 6.10 EDS microstructure mapping of 3D printed WE43.

Tab 6.2 Chemical composition (wt.%) of selected areas from Fig 6.10.

Element	O	Mg	Y	Nd
Point 1	11.62	65.56	2.86	3.51
Point 2	0.25	94.96	2.31	2.48

The obtained findings were used in the production of a new set of volumetric samples. Due to the large volume of vapours during the printing of the previous set, the number of samples on the build plate was reduced. At the same time, the laser power was reduced by 25 W to 225 W, even despite the obvious lack of energy density in the previous volumetric test. It was assumed that the insufficient energy density was due to a cloud of vaporized material that blurred the laser beam thus reducing its efficiency. By reducing the number of samples on the build plate and the laser power, the first steps were taken to reduce the volume of vapours generated during the printing process.

Along with the 3D printed samples, a new set of cast samples was also produced. These, in turn, were used to compare and identify differences from the 3D printed state.

The microstructural description of the 3D printed and cast samples corresponded to the previous findings (Fig 6.11). The microstructure of the 3D printed material contained fine grains with eutectic phases with a width of about 3 µm. More detailed EDS mapping revealed a dispersion of fine oxide particles randomly distributed in the microstructure. Due to this and the oxide shells of unfused powder particles, 3D printed material showed a significantly higher O_2 value than the cast material. Compared to previous testing, the material contained a lower number of defects. The resulting defects most often took the form of lack of fusion rich in O_2.

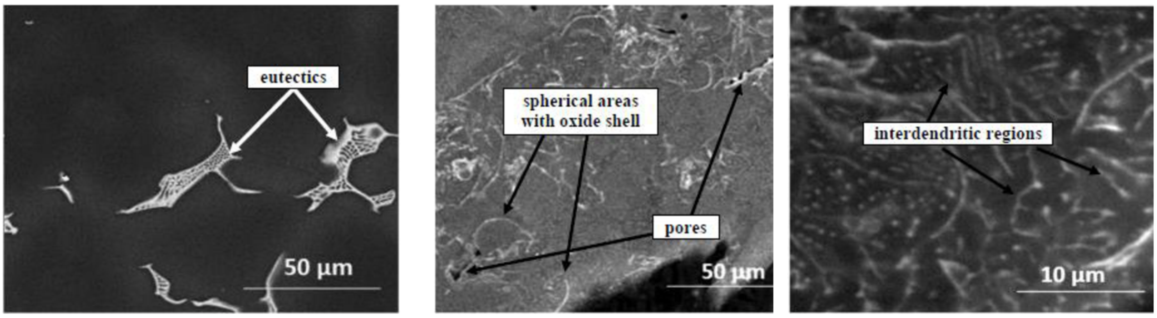

(a) (b) (c)

Fig 6.11 SEM images of WE43 material cuts: (a) in cast state and (b, c) in 3D printed state.

The microhardness test of the produced samples revealed a clear influence of the microstructure on the mechanical properties of the material. The test results are shown in a summary table (

Tab 6.3).

Furthermore, the samples were subjected to compression and three-point bending tests. In both tests, the 3D printed material achieved higher ultimate strength values (by 30 MPa more than the cast state), but at the expense of deformation properties, as can be seen from the graphs (Fig 6.12). The resulting compressive and three-point bending strengths are given in the summary table (

Tab 6.3). The results of this chapter are incorporated in Article D.

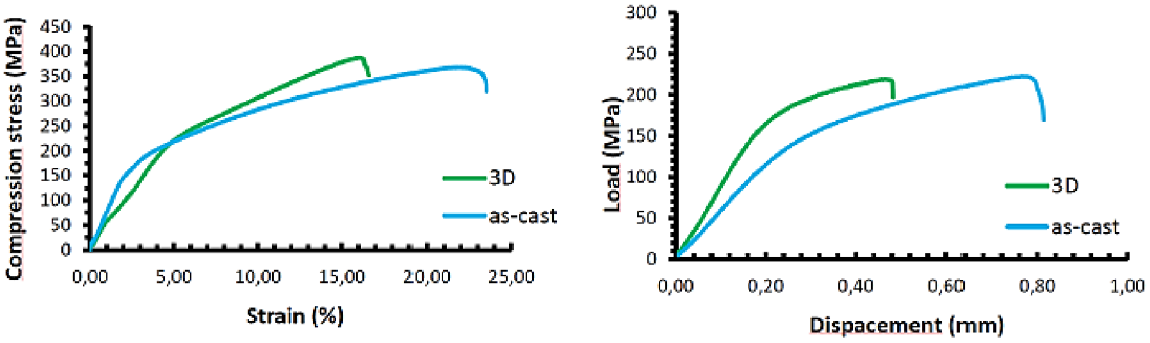

(a) (b)

Fig 6.12 Record of WE43 behaviour under mechanical loading: (a) in compression and (b) in three-point bending.

Tab 6.3 Comparison of selected mechanical properties of WE43 alloy in cast and 3D printed state.

Mechanical properties	**Casting**	**3D printing**
Compressive yield strenght [MPa]	204±34	229±20
Ultimate compressive strenght [MPa]	387±26	416±40
Flexural yield strenght [MPa]	119±2	145±8
Flexural strenght [MPa]	208±20	212±9

6.1.6 Modification of the inert atmosphere circuit

For reasons of safety, machine protection and increased vapour release, the circuit in a 3D metal printer which distributed and filtered the inert atmosphere was modified. The reason for this was the large number of vapours that were generated during the printing of the WE43 magnesium alloy and negatively affected the printing process. The resulting vapours had an adverse effect on printing repeatability, which was probably due to blurring of the laser beam. The resulting vapours also adhered to the protective glass of the laser, which could damage it (Fig 6.13).

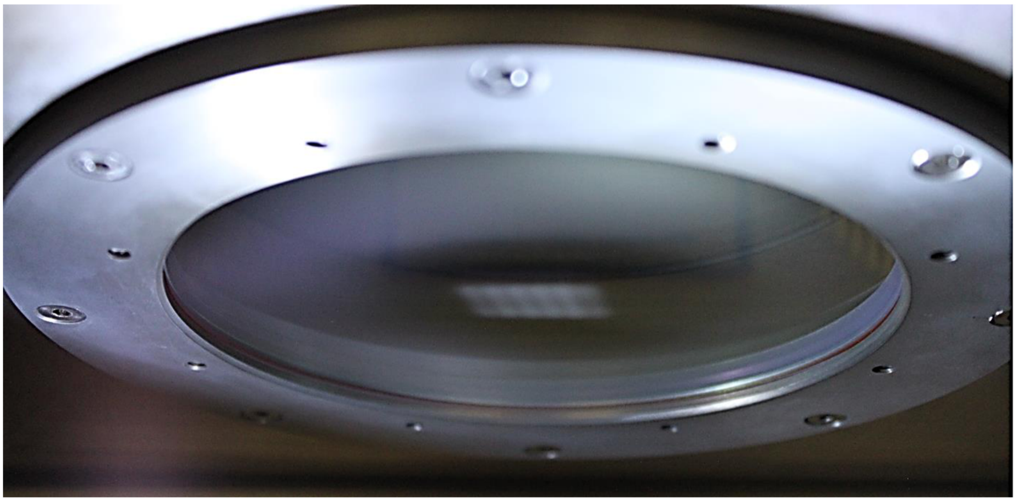

Fig 6.13 Deposition of evaporated powder on the protective glass of the laser when printing a large number of samples.

The first modification was to add another filter to the inert atmosphere circuit. Multi-stage filtration made it possible to capture the powdered condensate in several places and prevent it from accumulating in a single filter. The modification was designed so that in the case of ignition of one of the filters it could close its circuit and thus separate it from the process chamber with the magnesium powder. At the same time, the first filter had a higher permeability and served to capture only larger powder particles. The second filter was used to purify and capture the finest fraction of the powder. It was thus possible to keep the particularly highly reactive condensate (second filter) separated from a larger amount of condensate (first filter), which would feed the flame in the event of a fire.

The current output of the pump was not sufficient for the perfect extraction of vapours from the production space of the machine; it was necessary to add a more powerful pump into the inert atmosphere circuit (Fig 6.14). This made it possible to achieve greater pressure in the chamber and to remove the vapours more efficiently.

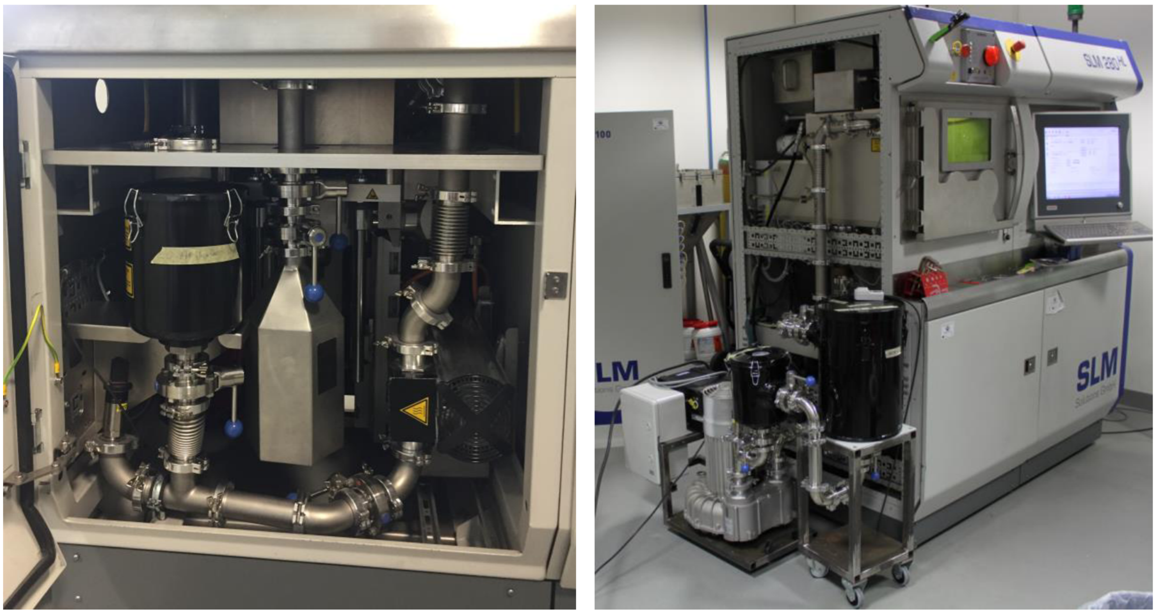

(a) (b)

Fig 6.14 The original single-stage filtration system housed in the machine space (a) and a modified variant of the two-stage filtration system with a more powerful pump and process emissions extraction from the upper part of the production chamber (b).

However, even this solution was not sufficient. By increasing the pump output above 35 %, the powder was entrained from the deposited layer. In addition, in the area of extraction, the vapours accumulated and rolled back into the process chamber along the side wall of the chamber. For this reason, a diffuser was added to the upper part of the chamber, which led the rolling vapours back into the filtration system (Fig 6.15). These adjustments helped to remove the vapours, but failed to remove them completely.

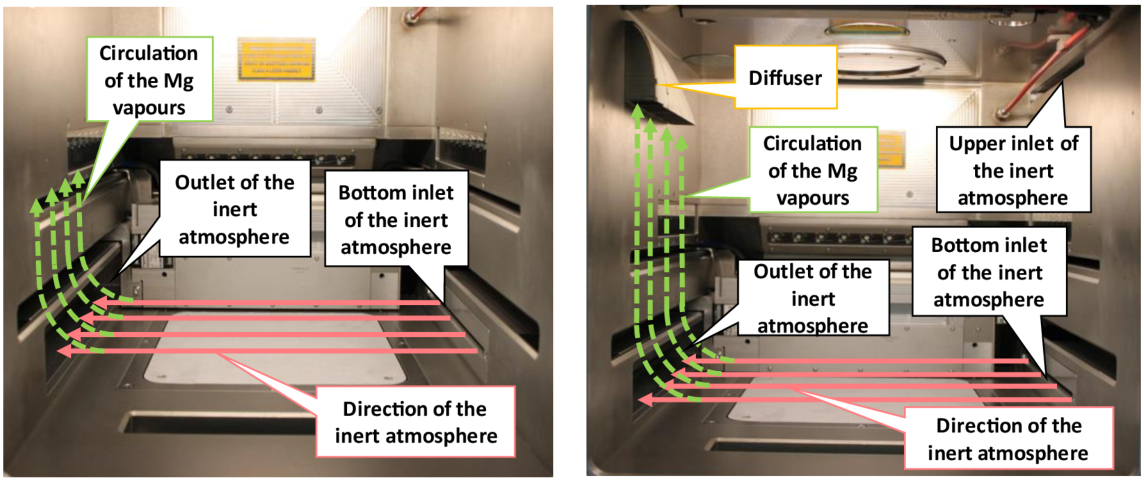

(a) (b)

Fig 6.15 Scheme of inert atmosphere flow and rolling of magnesium vapours (a) and process emissions extraction by diffuser (b).

6.1.7 Optimization of printing strategy

In order to further reduce the formation of vapours, the process parameters for printing volumetric samples were corrected. The observations showed that the amount of vapour generated was directly proportional to the volumetric energy density for printing the samples. Therefore, the aim of the test was to reduce the number of vapours generated while maintaining the relative density of the samples above 99 %. After releasing most of the vapours from the production chamber, a sample production began to deal with uneven porosity distribution. The porosity in the part increased with increasing distance from the build plate (Fig 6.16). The shape of the pores was predominantly spherical, indicating the printing of a high energy density sample. The occurrence of porosity in the more distant regions from the build plate was related to deteriorating heat dissipation from the fused layer. To achieve constant temperature conditions for each produced layer, a time delay of 100s was included between the production of individual samples in order to prevent the accumulation of thermal energy in the samples and the removal of residual vapours in the production chamber. This modification of the production process led to an even distribution of porosity in the samples.

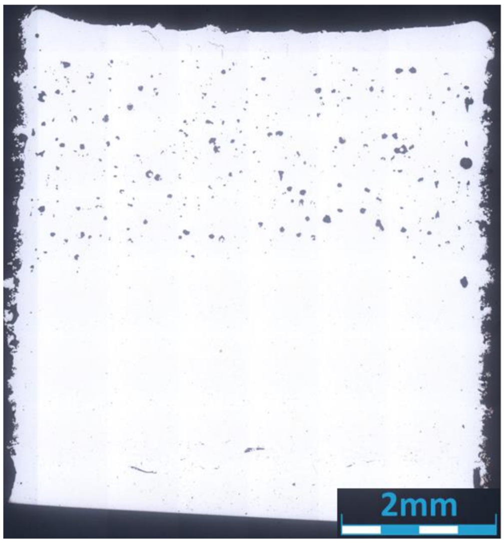

Fig 6.16 Porosity distribution in the sample (Lp = 250 W; Ls = 450 mm·s^{-1}; Hd = 90 µm) after modification of the inert atmosphere circuit.

Based on previous findings, laser power has been identified as the parameter that most affects the manufacturing process and was therefore likely to need to be reduced. In order to have enough energy in the melt pool to melt the powder, it was necessary to increase the energy value in a way other than through laser power. Thus, a series of thin walls was produced, on which the development of their width was monitored in relation to the change of process parameters (Fig 6.17). From the obtained results, a constant distance of weld deposition hatches was designed for printing volumes so that their overlap was always at least 50 %.

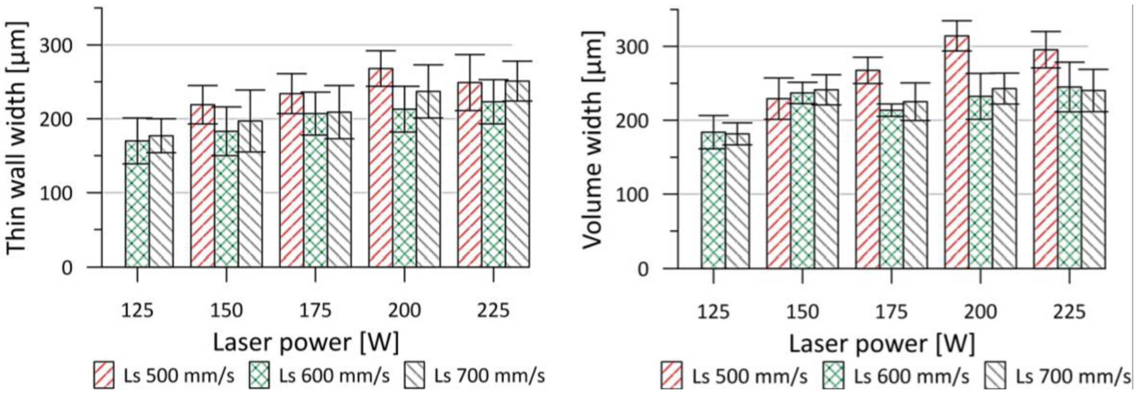

(a) (b)

Fig 6.17 Development of weld deposition width depending on laser power and scanning speed: (a) in thin-walled and (b) volumetric samples.

With such a fixed hatch distance, a porosity test was designed in the range of laser power of 125–255 W and scanning speed of 500-700 mm·s^{-1}. The observed value in the samples was the porosity in the plane perpendicular to the build plate (X–Z). Observations of etched metallographic cuts revealed an average weld deposition depth of 0.48-0.8 mm. This corresponded to the remelting of 9-16 already solidified layers. This method of printing led to the formation of mostly key-hole porosity in the roots of weld depositions (Fig 6.18). By gradually reducing the volumetric energy density, the relative density of the samples reached 99.48% (Fig 6.19). The results of this chapter are incorporated in Article E.

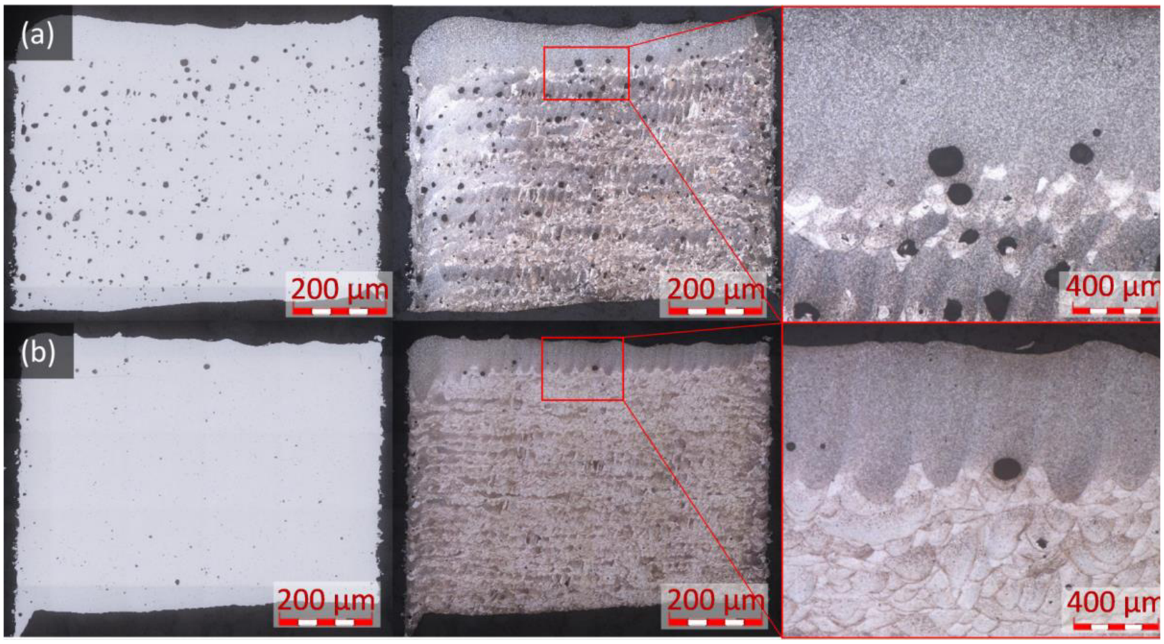

Fig 6.18 Porosity in the structure of the samples in the plane perpendicular to the build plate (X–Z):
(a) Lp=225 W; Ls=600 mm·s^{-1}; E$_v$= 83.3 J·mm^{-3}, pause in printing 100 s, relative density 96.29 %;
(b) Lp=175 W; Ls=700 mm·s^{-1}; E$_v$= 55.5 J·mm^{-3}, pause in printing 100 s, relative density 99.48 %.

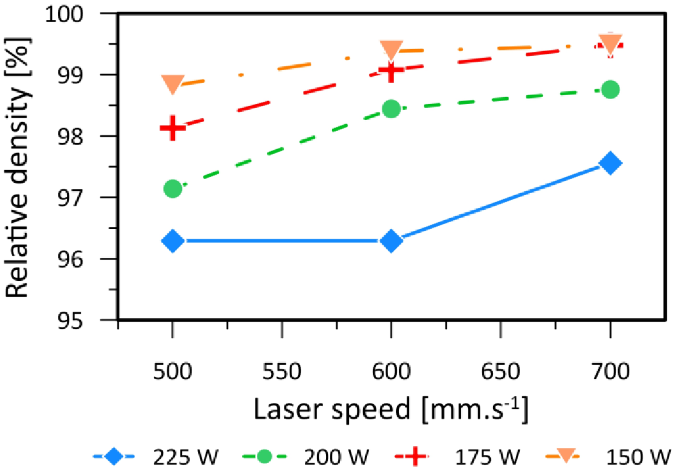

Fig 6.19 Dependence of relative sample density on laser power and scanning speed.

6.2 Corrosion behaviour of material in simulated human body environment

6.2.1 Microstructural analysis

The first step in this part of the work was to determine how much the process parameters influence the microstructure of the samples. For this purpose, volumetric samples from different test phases and combinations of process parameters were selected. EDS and EBSD analyses were performed on the cuts of samples, which served as a basis for comparison of the examined samples.

The microstructure of the samples consisted mainly of an α-Mg matrix. Randomly distributed particles of various shapes (floccules, needles, spherical,…) occurred in the microstructure. These particles were rich in RE elements (Fig 6.20). Their composition corresponded to the chemical composition of the WE43 alloy. The most commonly found oxides were Y and Nd compounds. The observed particles did not exceed a size of 5 μm. However, several particles appeared in the microstructure, the chemical composition of which could not be determined due to their size.

Directionality was also monitored in the material using EBSD (Fig 6.21). It was not found due to the chosen meander printing strategy with a rotation of 67 ° on each layer. Grain size was also observed (Fig 6.22). In the structure of the material, both large grains formed by the constant remelting of already solidified layers of powder and small grains around the boundaries of the weld depositions were found. The acicular shape of these grains indicates the direction of solidification from the centre of the weld deposition to its boundaries. By comparing the findings from previous tests, it can be stated that the microstructure of the samples was practically the same in terms of chemical composition, shape, size and distribution of particles. The only significant difference was in the relative density of the samples, the shape and the occurrence of defects. However, after reducing the amount of vapour during printing and reaching a relative density of 99.48 %, the samples behaved practically the same in terms of selected analyses and did not show sensitivity to changes in process parameters. The results of this chapter are incorporated in Articles C and E.

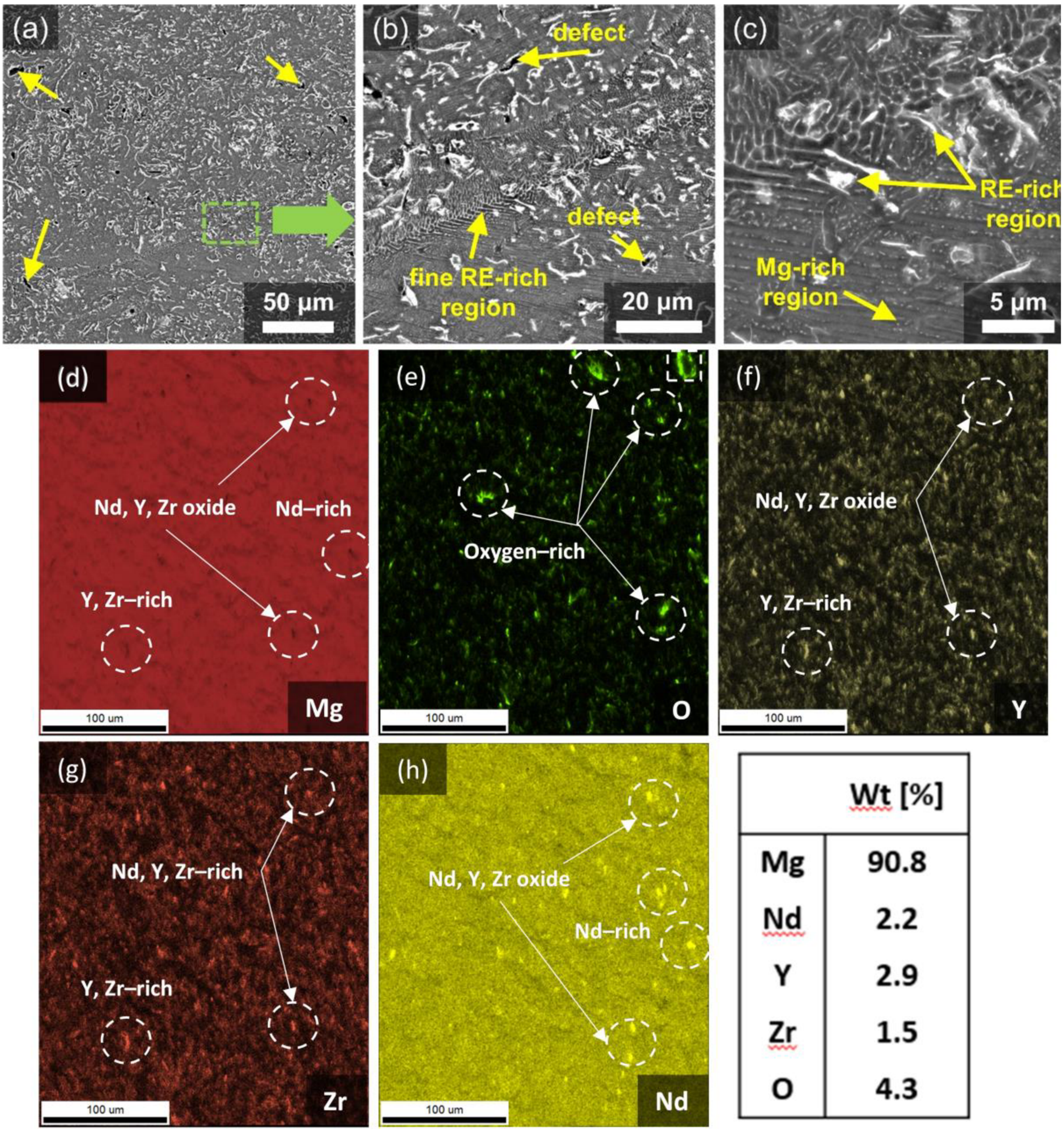

	Wt [%]
Mg	90.8
Nd	2.2
Y	2.9
Zr	1.5
O	4.3

Fig 6.20 EDS description of the microstructure of WE43 alloy in the direction perpendicular to the build plate. The as-built sample was tested before the immersion test: (a) overview; (b, c) detail (SEM-BSE); (d–h) EDS mapping of the selected region.

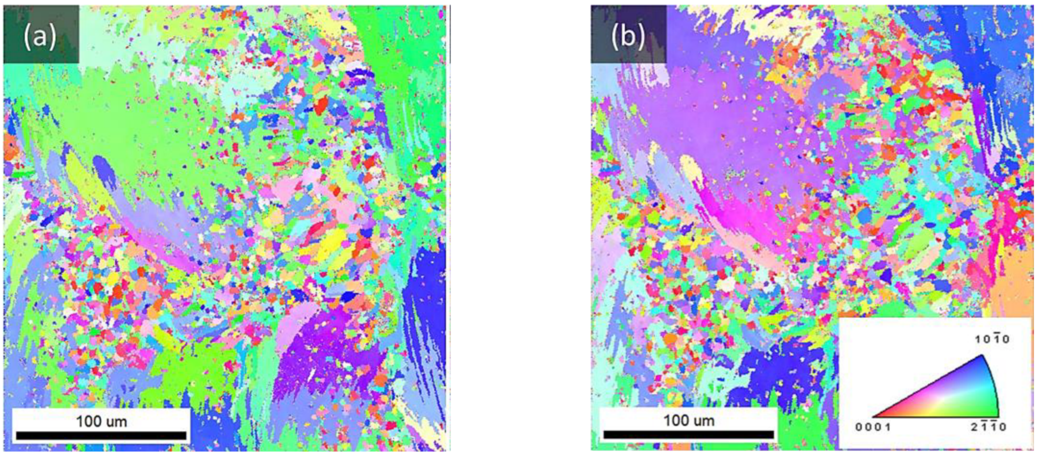

Fig 6.21 IPF map: (a) direction of powder application and (b) normal direction.

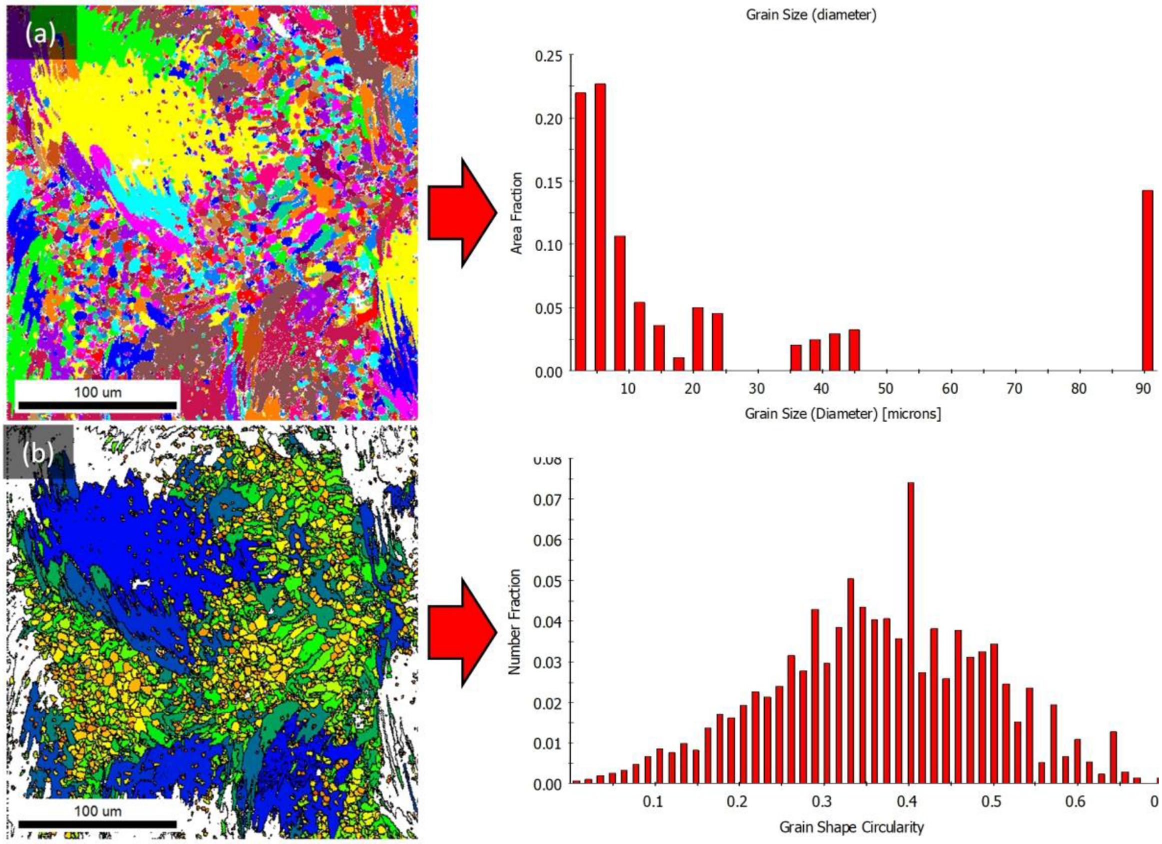

Fig 6.22 Example of selected properties of material grains: (a) grain size and (b) circularity and highlighting of grain boundaries.

6.2.2 Measurement of surface roughness of thin walls

The second step was to clarify the influence of process parameters on the surface quality of the printed material. This behaviour was observed on thin walls produced with different combinations of laser power and scanning speed.

The amount of fused powder significantly reduced the surface quality and locally prevented the surface from being scanned with an optical profilometer. The obtained topological data had to be interpolated with a 5th degree polynomial to obtain a complete description of the surface. The obtained data were plotted against the laser power and scanning speed to explain their effect on the surface quality (Fig 6.23). It was clear from the observations that the increase in linear energy density led to an increase in the surface roughness. Again, it was confirmed that the laser power has a greater effect on the result than the scanning speed. The surface roughness Ra ranged from 34.2 to 61.3 μm. The lowest surface roughness was achieved by a combination of 100 W laser power parameters and a scanning speed of 500 $mm \cdot s^{-1}$. From the given data, an equation was calculated to describe the observed surface behaviour (6.1), while its coefficient of determination was 97.68 %. The results of this chapter are incorporated in Article A.

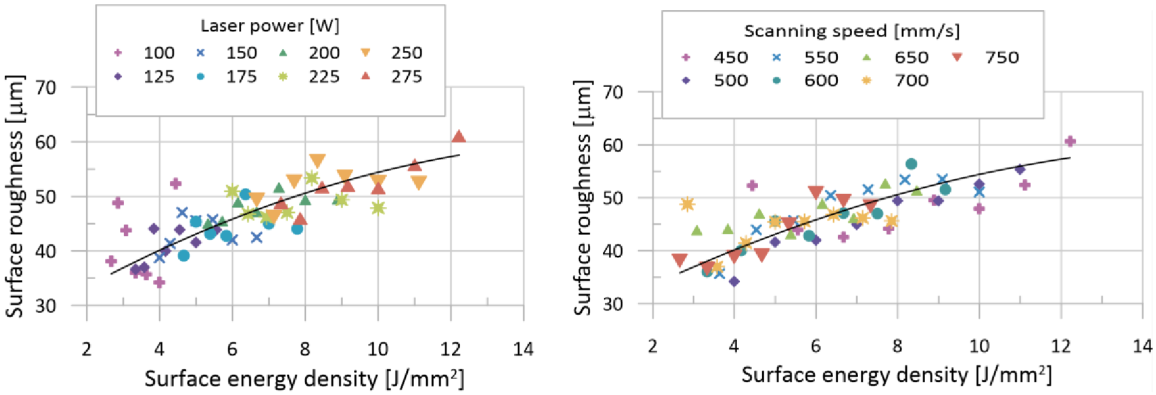

(a) (b)

Fig 6.23 Arithmetic dependence of the surface depending on: (a) laser power, (b) scanning speed.

$$Y = 25.8767 + 4.062x - 0.1181x^2 \tag{6.1}$$

6.2.3 Immersion test

Findings from previous analyses showed a significant sensitivity of surface quality to process parameters. On the contrary, the microstructure of the material, and thus the shape and size of the cathodic phases, hardly changed with the change of process parameters. Due to the ability to significantly control the surface quality by changing the process parameters, the sensitivity of the corrosion rate to the surface quality was monitored during the immersion test.

The test itself was performed on several sets of volumetric samples. Prior to immersion in the corrosion solution, the surface roughness of all sample sets was measured: as-built (Ra 51.02), SiC120 (Ra 3.84), SiC500 (Ra 1.02) and SiC4000 (Ra 0.11). The Ra value was determined as the average of three measurements. Each set was tested for 168 h (7 days) (Fig 6.24). At the beginning of the test, an electrolyte appeared in all cross-sections sets between the sample surface and the aqueous solution, which increased the corrosion rate after the first 2 hours of testing. After another 7 hours, the corrosion rate gradually decreased. The as-built set, on the other hand, showed a different behaviour. Its corrosion rate accelerated slowly. However, after 21hours of testing, the corrosion rate started to increase rapidly. This was matched by a large weight loss in the set. The average pH in the solution was 9.3, which confirmed the release of hydrogen due to alkalinization of the medium to form Mg (OH_2).

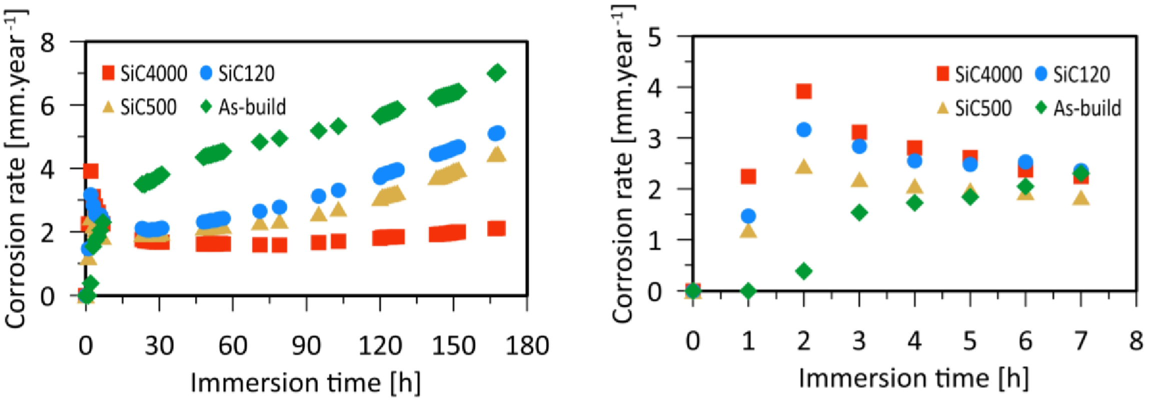

(a) (b)

Fig 6.24 Corrosion rate of WE43 magnesium alloy in HBSS at 37 °C calculated from hydrogen released during testing for: (a) 168 h and (b) 7 h. The curves were obtained as the average of three measurements.

The as-built set was chosen for detailed corrosion layer testing due to the largest weight loss. The phase composition of these samples was monitored by XRD before and after the corrosion test (Fig 6.25). The test revealed mainly the phases of RE elements and Mg (OH_2) in the samples that passed the corrosion test. A detailed analysis of the corrosion layer was performed by SEM (Fig 6.26). Regions where the samples corroded faster were identified, which led to pitting. Cracks were also found in the investigated passivation layer, which allowed for further corrosion propagation. Its EDS analysis revealed the presence of elements such as Mg, O, Y, Nd, P, Cl, Na and Ca. The results of this chapter are incorporated in Article E.

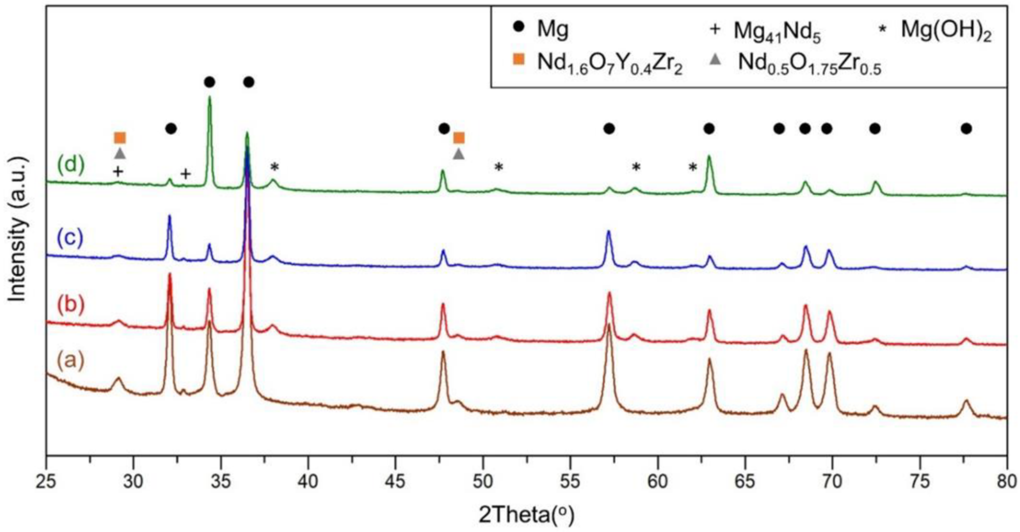

Fig 6.25 X-ray diffraction field: (a) As-built sample before corrosion test and (b–d) As-built sample after corrosion testing in HBSS.

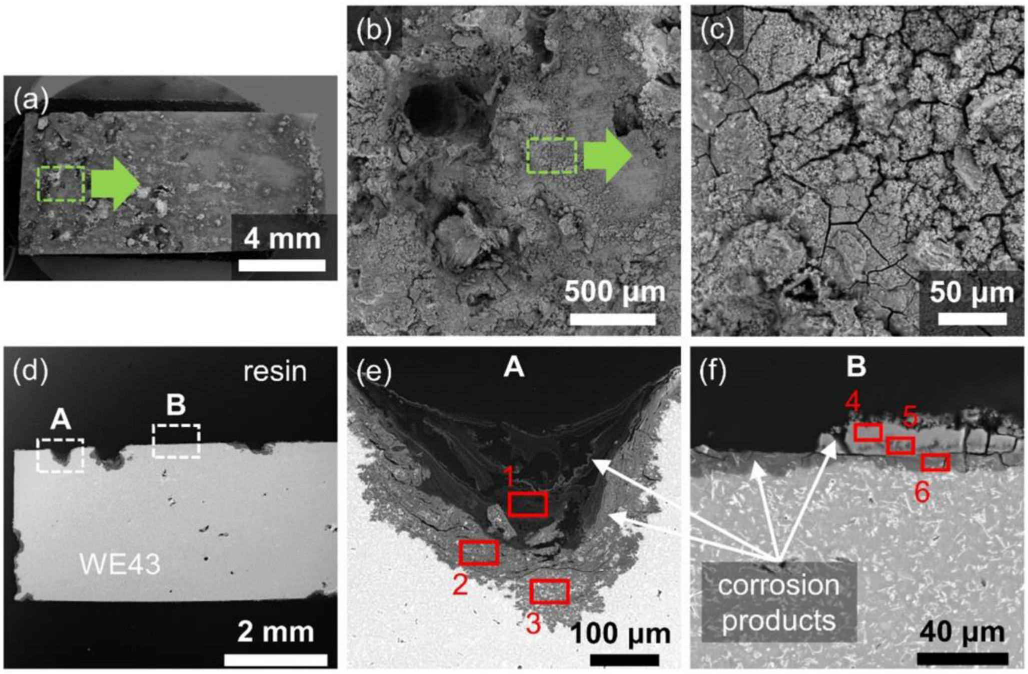

(g)

Position	Element (wt.%)								
	Mg	O	Y	Nd	Si	P	Cl	Na	Ca
1	47.8	45.1	-	-	1.2	1.0	4.4	-	0.5
2	46.0	50.5	2.3	1.2	-	-	-	-	
3	43.3	49.6	4.2	1.7	0.5	-	-	-	0.7
4	5.5	50.1	-	-	-	17.3	-	0.6	26.5
5	12.9	51.8	-	1.4	-	15.2	-	1.0	17.7
6	34.6	51.1	4.8	3.5	-	2.7	1.2	0.7	1.4

Fig 6.26 Appearance of as-built sample after immersion corrosion test in HBSS: (a-c) sample morphology; (d-f) cross section of the sample and (g) table of local chemical composition.

7 DISCUSSION

7.1 Achieving the required mechanical properties of 3D printed material WE43

7.1.1 Analysis of the shape and continuity of weld deposition tracks

The aim of the test was to define the value of linear energy with which the weld depositions had a continuous track with suitable ratios between their main dimensions. Based on the obtained results, a process map (Fig 6.1) was developed in a similar way as was used for weld depositions from other studies [81, 82].

The minimum linear energy for printing of continuous weld depositions was 5.5 $J \cdot mm^{-2}$. By using smaller values of linear energy, the melt pool became unstable. Its collapse was due to surface tension. As a result, separate regions were formed where the melt existed but did not bond, as mentioned here [81, 83]. This led to an intermittent weld deposition track and a non-bonding of the molten material to the build plate. This phenomenon was observed on the weld deposits in the form of a balling effect.

In the linear energy range of 5.5–15 $J \cdot mm^{-2}$, the weld depositions became continuous and uninterrupted. With increasing value of linear energy density, the depth of weld depositions increased to values of 300 μm and more. By increasing the energy above 15 $J \cdot mm^{-2}$, the magnesium material began to evaporate, forming a black mist, which has already been observed in other publications [84–86]. Laser blur due to vapours, the penetration of very deep weld depositions with root porosity and an unstable melt pool made this region unsuitable for further processing.

The occurrence of vapours was possible due to the very close melting point (545–640 °C) and vapour (1090 °C) of magnesium alloys, and, conversely, due to the high melting points of oxides that occur on the surface of the atomized powder (Fig 7.1). Upon reaching the temperature of the melt pool to dissolve the passivation layer covering the powder, the magnesium matrix had already begun to gradually evaporate. Despite the low melting point of magnesium, it may be necessary to use higher energy values to melt oxides. Thus, a higher relative density of the samples is achieved by gradual remelting of the already solidified layers. A similar principle is used for aluminium alloys (melting point 550-600 °C) due to their high reflectivity [87]. However, increasing the energy density also leads to an increase in magnesium vapours and it is necessary to find a suitable limit at which the material can be processed.

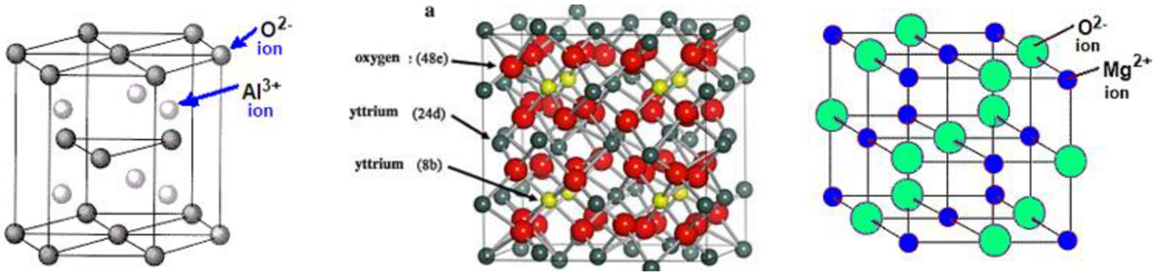

(a) (b) (c)

Fig 7.1 Crystal lattices of oxides and their melting points (T): (a) Al2O3, T=2 072 °C; (b) Y2O3, T=2 425 °C; (c) MgO, T=2 852 °C.

By comparing the results from the thin wall test with the weld deposition test, several differences were found. The width of thin walls and weld depositions was on average by 18 % larger. In addition, it was possible to print a stable thin wall with a linear energy density by 1 $J \cdot mm^{-2}$ lower than in the case of weld depositions. These observations were possible due to the accumulation of thermal energy in the thin walls. The depths of the weld depositions corresponded to 3-6 deposited layers of powder, which results in constant remelting of already solidified layers. Thus, it is not necessary to supply the thermal energy captured in the material with a laser, but to replace it by changing other main process parameters. It would probably then be possible to print the material at a lower energy density, which should have a positive effect on the amount of magnesium vapour generated. Although the measured values of the thin walls were shifted, the trends of their changes corresponded to the findings from the weld deposition test.

Major findings:

- Alloy process window diagram identified on linear samples.
- Dominant effect of laser power on the shape of weld depositions.
- Increase in the thickness of thin walls compared to weld depositions on average by 18 %.
- The depth of the weld depositions corresponded to 3-6 deposited layers of powder.

7.1.2 Chemical composition and microhardness of weld depositions

In the microhardness test, no significant differences were found between the microhardness of samples produced with different linear energy densities and laser powers. The reason was practically the same microstructure of weld depositions. The microhardness of the weld depositions depended mainly on the grain size.

The microstructure of the welds was composed mainly of α-Mg eutectics and intermetallic phases eliminated mostly at the weld deposition boundaries. The low incidence of intermetallic phases may be considered undesirable. The low content of intermetallic phases can result in an increase in the internal stress of the material and can lead to its cracking. However, the test did not show any dependence of microhardness and chemical composition on laser power. As a result, it was possible to drastically reduce the laser power during the tests.

Major findings:

- The change in laser power and energy density did not affect the chemical composition of the weld depositions and their microhardness.

7.1.3 Defects in volumetric samples

The limits of the investigated process parameters for the printing of volumetric samples were designed on the basis of the process window defined in the weld deposition test. The volumetric samples contained a relatively large number of defects related to insufficient energy density. This created lack of fusion in the material leading to delamination of the samples and other macroscopic defects. However, the lack of fusion showed directionality. They were formed due to the non-bonding of the individual deposited layers of powder. The layers of material could not be fused together for two reasons. The first one was the presence of oxides, typical of RE alloys on the surface of already solidified material. Thus, the complete fusion of the new material to the previous layer occurred only when the surface layer of oxides melted. However, due to the rapid solidification, the oxide layer did not have to be melted, but only disrupted by the thermal expansion of the material. Fine particles of not fully melted oxides, broken off from the surface of the material, then formed lack of fusion in the material. The second cause could be the presence of vapours in the production chamber. Their presence could blur the laser beam; it did not have to have the required energy density when it hit the surface of the material. This hypothesis was also confirmed by the increasing rate of defects in the material in the last printed samples, when the vapours had already accumulated in the production chamber. The formation of lack of fusion probably occurred through a combination of both phenomena.

The resulting defects in the material did not have a significant effect on the hardness of the material, which indicates a stable microstructure throughout the sample. However, the porosity value in the material affected its compressive strength. Defects along the deposited layers related to their non-bonding mainly contributed to the porosity of up to 1 %. By increasing the porosity above 1 %, larger defects have already begun to appear in the material. Porosity up to 1 % had no significant effect on the compressive strength of the test material. The reason was probably the orientation of the samples during the pressure test. As the samples were loaded perpendicular to the lack of fusion, the cracks caused by them did not tend to open, but rather close. Even a large number of lack of fusion, which had a rather elongated shape, only slightly penetrated into the relative density of the material, in contrast to shrinkage and unfused powder particles. After that the samples, which contained a large number of lack of fusion but had a low porosity value, achieved higher values of compressive strength in contrast to the samples, which contained a relatively smaller number of defects but contributed more to the porosity value.

The occurrence of lack of fusion also corresponds to the behaviour of energy density. Its increase made it possible to better melt the oxidized surface of the powder and thus fuse the material more consistently together. At the same time, the value of the energy density at the point of impact of the laser was increased, despite the blurring of the laser beam. However, the increase in energy density also led to an increase in the amount of evaporated material; therefore, the process chamber was filled with black smoke more quickly. When the amount of vapour became critical, the laser beam had already been blurred to such an extent that the manufacturing process was not possible. This confirmed the assumption that the amount of evaporated magnesium had to be reduced. The parameter that most affected the manufacturing process and the presence of Mg matrix evaporation was laser power.

Major findings:

- Delamination of samples due to non-bonding of deposited powder layers.
- By increasing the energy density, the material can only be partially fused together, as the higher input energy corresponded to a more massive evaporation of magnesium, which subsequently defocused the laser beam.
- The directionality of lack of fusion did not show so much in the pressure test and the hardness of the material.

7.1.4 Reducting the amount of vapour

When printing the samples, their number was reduced to a minimum due to the accumulation of magnesium vapours in the production chamber thus avoiding a gradually increasing number of defects. However, despite the reduction in the number of samples, a considerable amount of smoke was released and started to accumulate again in the production chamber of the machine during printing. Nevertheless, in total, the amount of evaporated magnesium was less than in previous tests, which resulted in fewer defects in the material. The reduction in the amount of vapour did not have a significant effect on the shape or chemical composition of the resulting phases in the material. A lot of oxides still appeared in the 3D printed material, which was missing in the WE43 cast material. The size of the grains and phases corresponded to previous findings. The chemical composition of the phases in the 3D printed material was the same as in the cast material. The only difference was in the size and distribution of the particles. The reason was a different process of cooling the material and the way of supplying thermal energy. The distribution of particles in the 3D printed material was linked to the laser hatches, whereas, in the case of the cast material, a solidifying front was evident.

The fine grain and a relatively homogeneous distribution of intermetallic phases in the 3D printed material was the reason for its higher strength and hardness. However, the 3D printed material suffered a relatively low deformation value compared to the cast material. One of the reasons was the fine-grained structure of the 3D printed material. However, as the grain size in the material increases, so does its toughness, which is directly related to the amount of deformation the material can withstand. Another reason was probably the binding of a large amount of oxygen to the 3D printed material. The formed oxides are characterized by their hardness, strength but, on the contrary, by their fragile behaviour. Their presence in the material probably increased the already low deformation properties of the material.

Despite the presence of defects in the material and their directivity related to lack of fusion between the deposited layers of powder, the three-point bending strength was higher for the 3D printed material. The reason was probably the fine-grained structure, which better resists the propagation of cracks and dislocations in the material. Therefore, the resulting crack in the 3D printed material needs a higher initiation stress for its propagation than in the case of a cast material. However, if the required initiation stress is reached, the crack will become brittle due to the low toughness of the 3D material.

Major findings:

- By reducing the amount of generated vapour, no differences in the chemical composition of the 3D printed material were achieved.
- A significantly higher proportion of MgO appeared in the 3D printed material compared to the cast material.
- A satisfactory reduction in the amount of vapour could not be achieved only by changing the process parameters

7.1.5 Modification of the inert atmosphere circuit

In order to generate a large amount of magnesium vapour in the production chamber, an inert atmosphere circuit was modified. Due to a more efficient flue gas extraction, a stronger pump was added to in the circuit. However, during its testing, limits related to other components in the circuit were found. Although the increase in pump output significantly helped to remove vapours, several phenomena occurred.

The first of these was related to the entrainment of powder from the deposited layer. This led to a change in the layer thickness during printing, a change in the energy density with which the samples were printed. The inert atmosphere entered the production chamber through two openings (Fig 6.15). Most of the inert atmosphere flow entered the production chamber through the lower diffuser. The upper diffuser provided more mixing of the atmosphere in the chamber. The reason for the powder entrainment was the shape of the lower diffuser, which determined the direction in which the inert gas would be distributed to the production chamber. The shape of the diffuser entrained the inert atmosphere to the bottom plate of the chamber where layers of powder were deposited. Modifying this element could significantly help to reduce the powder entrainment and increase the pump output. Another modification that could help would be to add throttle valves to both inlets of the inert atmosphere. They could be used to control how the inert gas would enter the production chamber.

The increase in pump output also revealed shortcomings in the inert atmosphere outlet from the production chamber. The diameter of the pipe and its sharp transition at the outlet of the chamber led to the accumulation of vapours and their rolling along the side wall back into the chamber. For this reason, a second branch of the pipeline was built to extract vapours that began to roll along the side wall of the chamber. This branch was connected to the original pipeline before entering the filtration (Fig 6.14). By adding a diffuser to the second branch of the atmosphere outlet from the chamber, the efficiency of this branch was increased, but it was obvious that most of the vapours are discharged by the original branch. However, the process emissions in the process chamber have been reduced.

Parallel integration of the second filter into a circuit with an inert atmosphere increased the circuit safety. The first filter had a higher permeability and served to capture the largest condensate particles. The second filter was designed to purge the inert atmosphere flow. Thanks to the parallel connection, there was no accumulation of condensate in the space of one filter. At the same time, the fine, more reactive condensate was separated from the coarser one, i.e. if the condensate ignites, the magnesium flame will not be saturated with other material. Both filters can be closed separately using valves and can thus be separated from the inert atmosphere circuit in the event of a fire. Two-stage filtration also made it possible to increase the life of both filters, due to the capture of condensate in two places. The parallel integration of the filters resulted in a higher pressure loss in the circuit, which had to be compensated by an increase in the pump output.

Increasing the flow efficiency in the inert atmosphere circuit would be possible by straightening the individual branches. Replacing the pipes with stainless steel bellows would reduce pressure losses and increase the efficiency of the upper branches of the circuit. Another adjustment could be to filter the upper and lower output branches separately. This would prevent turbulence in the pipeline. The upper and lower branches would be connected immediately before the pump, which allows for the connection of even larger pipe diameters than those currently used in the circuit.

Major findings:

- Increased device safety.
- Increased extraction of process emissions from the production chamber.

7.1.6 Optimization of printing strategy

By improving the process emissions extraction, the use of existing process parameters in the samples began to reveal an uneven porosity distribution. The reason was the low heat transfer coefficient of the WE43 alloy, which was only 51.3 $W \cdot m^{-1} \cdot K^{-1}$, which is about half (96 $W \cdot m^{-1} \cdot K^{-1}$) compared with aluminium. Gradual printing of the samples increased the distance of the melt pool from the build plate through which the material was cooled, and moreover, thermal energy accumulated in the material due to constant remelting. These two factors led to a gradual decrease in the temperature gradient and heat accumulation in the above layers of the sample. The spherical shape of the pores in the sample also corresponded to this finding.

The accumulation of vapours in the production chamber worked against this phenomenon. With the printing of above layers, the amount of vapour in the chamber increased. They could not be fully discharged into the filtration system and the printing of higher layers took place at higher energy densities. As a result, the printing of higher layers generated a larger amount of vapour, and thus blurred the laser beam more, or a film of vapours began to form on the protective glass of the laser. Due to this and the large number of defects in the sample, the porosity appeared to be homogeneously distributed. After the integration of a new filtration system, the sample was no longer shielded by vapours, which resulted in an inhomogeneous pore distribution. This was solved by a time delay between printing the individual samples. The duration of this pause was 100s. but it did not undergo detailed optimization. This pause allowed for the material to be given the time needed to homogenize its temperature through the entire sample. In addition, the excess vapours were extracted during the time delay not creating a film of vapours on the protective glass of the laser.

By observing the cross-section of samples, it was found out that 9–16 already solidified layers were melted during laser printing. In addition, the porosity that appeared in the samples was located mainly in the roots of the weld deposits. This phenomenon corresponded to a high density of volumetric energy [77, 88]. A gradual reduction in the energy density increased the density of the samples up to 99.46 %. The energy density was regulated mainly by reducing the laser power, because, from among the process parameters, it had the greatest influence on the production process [89].

Also, the difference was defined in the width of the weld depositions when printing thin walls and volumetric samples. These findings can be effectively used to optimize the laser path overlap when creating the printing strategy of volumetric samples.

Major findings:

- Print repeatability is ensured.
- Relative density of processed material is 99.5 %.

7.2 Corrosion behaviour of the material in the simulated human body environment

7.2.1 Microstructural analysis

A microstructural analysis revealed significant differences in the cast, extruded and 3D printed material. The 3D printed material contained the finest grain. This was possible due to the high temperature gradient during the SLM process. As a result, the cathodic phases were present in the material only in the form of a fine dispersion of particles rich in RE elements. These were homogeneously distributed in the material. The material also contained a number of defects, the origin of which was explained in previous chapters.

The EDS analysis revealed a passivation layer of oxides along the boundary of lack of fusion, presumably preventing the material from bonding. The same layer was observed on the surface of unfused powder particles trapped in the structure of the 3D printed material. This indicates an oxidized surface of the input material from the earlier atomization process. In addition to the boundaries of the lack of fusion and the surface of the powder, small oxide particles were also abundant in α-Mg eutectics. This significantly increased the amount of oxygen trapped in the 3D printed material compared to conventional processing methods. Small oxygen particles probably served as nuclei during melt solidification, as has been observed earlier [38]. This corresponds to the size of oxides (up to 5 µm) and their random distribution in α – Mg. This behaviour, together with the high temperature gradient, probably prevented the formation of large Mg-Y-Nd intermetallic phases as in the case of the cast material.

The microstructure of the 3D printed material consisted mainly of a solid solution of α – Mg, eutectic phase of MgO and randomly distributed floccules rich in RE elements. The phase that was most contained in the microstructure was MgO and its occurrence can be explained in two ways. The first one is the presence of residual oxygen in the printer's production chamber due to the purity of the inert gas [65]. The second one was related to the release of residual oxygen from the passivation layer of the powder material. It is known that the solubility of O_2 in pure Mg is below 1 at %. Oxygen is released from the powder during the manufacturing process as part of the vapours of the magnesium matrix. However, previous findings [63], reported that the combustion reaction is not sufficiently fast to prevent magnesium-rich vapours from reaching the surface and, subsequently, diffusing into the material. The oversaturated solid Mg – $O_{solution}$ on the surface of the material precipitated according to the following equation (7.1).

$$Mg - O_{Solution} = Mg + MgO \tag{7.1}$$

Oxygen that was not burned or diffused into the surface of the material was extracted via a circuit of inert atmosphere. For this reason, the oxygen content in the chamber increased during printing and had to be corrected by a constant flow of argon atmosphere. The MgO compact film could not be formed because the material underwent repeated remelting, which divided the compact film into small particles distributed in the microstructure of the material.

Alloys rich in RE elements form strong intermetallic phases with cathodic behaviour, which significantly increase their corrosion rate [56]. However, in the case of 3D printed material, they occur in much smaller sizes and thus contribute to galvanic corrosion of the material to a lesser extent. The material also contained fine needles, which were located at the boundaries of the weld depositions and corresponded to the direction of melt solidification. SiO_2 particles were also found in the material, which could increase the corrosion rate of the tested samples, although X-ray diffraction did not reveal the presence of Mg_2Si phase. Probably, Si has already entered the samples with the input powder.

Major findings:

- The reason for the increased amount of enclosed oxygen in the structure of the 3D printed material has been clarified.
- The average size of the intermetallic phases in the material was up to 5 µm.

7.2.2 Surface quality analysis

The surface roughness of the measured thin walls was affected by several factors. One of them was the balling effect, which occurred in the samples printed in the energy range of 2–4 $J \cdot mm^{-2}$. This region could be easily avoided by changing the process parameters. The other factor was the amount of powder fused to the surface of thin walls. From the obtained data, it was evident that the printing with a high energy density led to the enlargement of the melt pool, which affected a larger amount of the surrounding powder that was subsequently fused to the surface of the sample. Similar findings were observed with the titanium alloy Ti6Al4V [90]. On the contrary, reducing the energy density to a minimum so that the balling effect has not yet started to appear has proved to be a way of how to achieve the lowest Ra values. The last significant effect on the surface quality was the oxidation of WE43 alloy. Despite keeping the oxygen value in the production chamber below 0.1 % with a constant flow of Ar 5.0, it was not possible to prevent the oxidation of the melt; this has already been stated by many authors [32, 40–42]. The formed oxides adhered to the surface of the samples in the form of tiny balls, which negatively affected the surface roughness.

From the graphs (Fig 6.23) it was evident that the surface roughness can be significantly affected by the choice of process parameters. After creating a strategy for printing volumetric samples, it would be possible to use the obtained data and to include a printing of the contours in the printing strategy. The process parameters of contours have been to be different from the volume. For example, the sample surface can be printed with lower energy density to achieve a better surface without any post-processing operations.

Major findings:

- The surface quality of the material can be significantly influenced by the choice of process and technological parameters, of which the laser power has the greatest impact.

- Reduction of surface roughness from Ra 61.3 to Ra 34.3 using laser power of 100 W and scanning speed of 500 mm·s^{-1}.

7.2.3 Immersion test in HBSS

During the immersion test, a different behaviour was observed in the as-built set compared to the ground sets. The difference was due to the surface quality and the different passivation layer, which was different at the beginning of the test in the compared sets. While the surface of the ground sets contained predominantly MgO, because the ground samples were only in contact with dry air, only a few hours before the beginning of the immersion test. A film was formed on the surface of the samples which did not exceed 3 nm in thickness (according to the Mg–Al binary diagram) and could be easily damaged by corrosion. This corresponded to the observed rapid increase in corrosion rate in the first two hours of the test. Subsequently, the rate increase slowed down and stabilized due to the formation of a new passivation film.

In contrast, the as-built passivation film probably contained Mg $(OH)_2$ because the samples were exposed to atmospheric moisture during post-processing. The Mg $(OH)_2$ film forms a more compact layer than MgO [91]. Thus, at the beginning of the immersion test, the samples were more protected from corrosion by a more robust passivation film; therefore, the increase in corrosion rate was slower. However, these compounds are metastable and do not provide full passivation of the alloy [92]. Therefore, after overcoming the initial passivation layer, the corrosion rate began to increase rapidly in direct proportion to the surface quality of the samples. A significant increase in the corrosion rate after overcoming the initial passivation layer was caused by splitting the fused powder particles from the surface of the samples. This was reflected in the weight loss of the samples, from which the corrosion rate was calculated.

The maximum corrosion rate of biodegradable implants was set at 0.5 mm·year^{-1} [93]. Therefore, it is clear from the obtained results that it is not yet possible to achieve the required corrosion rate by simply changing the process parameters, although they can significantly affect the overall corrosion behaviour of the alloy. To achieve a lower corrosion rate of the 3D printed material, it would be necessary to use post-processing operations. For example, a reduction in corrosion rate below 0.5 mm·year^{-1} can be achieved by surface treatment by plasma electrolytic oxidation (PEO) [69].

8 CONCLUSION

The presented PhD thesis deals with the processing of magnesium alloy WE43 by SLM technology with the main goal to clarify the influence of process parameters on the corrosion behaviour of 3D printed material. The proposed goal was chosen with regard to the currently solved problems related to the application of biodegradable implants and it has been achieved.

The PhD thesis summarizes the most important results from previous studies dealing with the oxidation and processing of magnesium alloys using laser technologies, especially SLM technology. From the mentioned studies, hitherto undescribed places were defined and the main issues related to this topic were described. The objectives of the presented work were compiled from the above findings. To meet the main goal of the thesis, scientific questions were asked and hypotheses were developed for testing. The thesis was divided into two main parts; the results were published in several scientific articles. The thesis is a compilation of the author's published results. The first part of the thesis was devoted to the material with a relative density close to 100 % and its mechanical properties are similar to human bones. To this end, a number of tests were performed. The first one was the definition of a process map of the WE43 magnesium alloy, which showed the behaviour of the weld deposition tracks depending on the laser power, scanning speed and linear density of energy. Geometry, stability and continuity were monitored on weld deposition and thin-walled samples. Furthermore, an initial test of the chemical composition of the weld deposition track and the sensitivity of its microhardness to changes in laser power was performed. Phenomena arising from samples due to changes in process parameters have been described, substantiated and placed in the context of other publications. This part of the tests was published in the journal Materials (MDPI, IF 3.623). A summary of the most important results can be referred to in several points:

- Linear energy for printing stable weld depositions was defined in the range of 5.5–12 $J \cdot mm^2$ (Fig 6.1).
- Layering weld depositions on top of each other increases their width by 15-17 %, which can be used effectively when setting the overlay of weld depositions in printing the volumes.
- Layering weld depositions on top of each other decreases the linear energy necessary to print stable weld depositions of ca. 1 $J \cdot mm^2$, the reason is accumulation of thermal energy in the sample due to remelting
- A change in laser power and scanning speed did not affect the microhardness and chemical composition of the weld depositions (Fig 6.4).

The goal of the second test was a transition from linear to volumetric samples. The results of the influence of process parameters on the formation of defects in volumetric samples, the microstructure of 3D printed material and its basic mechanical properties were gradually presented in scientific articles.

The first results were related to the number of defects in the produced volumetric samples. Their origin was related to the used combination of process parameters, the change of which significantly changed the relative density of the material. In addition, the impact of some defects seemed to be more dominant than others. This was verified by a hardness and compressive strength test. The results were published in Manufacturing Technology (Elsevier, SJR 0.254) and can summarized as follows:

- The choice of process parameters significantly affects the relative density of the samples.
- During printing, there appears a large amount of vapour that fills the production chamber.
- Due to the type of testing, the defects in the material did not fully manifest themselves.

The second results were achieved in the microstructural analysis. We managed to create a basic microstructural description of 3D printed material and compare it with the cast and extruded material. The differences were discussed. The largest differences were found in grain size and intermetallic phases in the material. There was also a difference in the distribution of phases in the structure of the material, which corresponded to the technologies used. A significantly higher proportion of captured oxygen in the form of MgO was also found in the microstructure of the 3D printed material. The results were published in Manufacturing Technology (Elsevier, SJR 0.254) and are summarised as follows:

- The 3D printed material has the finest grain from among the above-mentioned states.
- Significantly more O_2 was bound in the structure of the 3D printed material compared to other states.
- The chemical composition of the intermetallic phases remained unchanged. Only their size and layout have changed.

The third series of results related the results from the microstructural analysis and mechanical testing. The 3D printed material contained discontinuities between the layers of deposited powder and unfused powder particles. The formation of defects was caused by insufficient energy density to melt the surface layer of oxides on the input powder. In addition, the increase in energy density led to a massive evaporation of magnesium, which blurred the laser beam. An oxide layer was found both at the boundaries of the lack of fusion and on the surface of the unfused particles. However, despite these defects, the 3D printed material achieved higher compressive and three point bending strength than the cast material. The reason was a very fine microstructure of the 3D printed material. Nevertheless, the fine-grained structure significantly reduced the possibility of deformation properties of the 3D printed material due to the large number of grain boundaries that prevent the movement of dislocations. The results were published in the Defect and Diffusion Forum (ScientificNet, SJR 0.240). The results can be summarized as follows:

- Defects in the material were caused by massive evaporation of Mg during printing and a passivation layer on the surface of the input powder.
- 3D printed material achieved higher compressive and three-point bending strength than cast material due to fine-grained microstructure.

From previous results, it was clear that the quality of the production process is severely limited by the evaporation of magnesium. This led to a number of defects in the 3D printed material and variance in the repeatability of the results. In these respects, the existing inert atmosphere circuit has been improved to be able to better take the process emissions away from the 3D printer's production chamber. Improvements included a multi-stage filtration, the creation of a new exhaust branch fitted with a diffuser for more efficient vapour collection, and the integration of a more powerful pump in the circuit. The improvement of the circuit reduced the amount of process emissions accumulated in the production chamber. However, after several tests of the new circuit, several new ideas arose of how to further improve the circuit. The current solution and its further improvement were discussed. The reduction in the amount of process emissions in the production chamber led to a new behaviour of the produced samples; therefore, the production process had to undergo further optimization.

The third and final series of tests in this section dealt with the optimization of the production of volumetric samples and the corrosion behaviour of 3D printed material. Due to the low heat transfer coefficient of the WE43 alloy, there was an uneven distribution of porosity in the samples. Thus, a time delay in the production process allowed to homogenize the temperature conditions inside the sample. As the laser beam was no longer blurred by vapours, the energy density for printing the samples was gradually reduced. The energy density level to melt the powder has so far been maintained mainly by laser power. As part of the optimization, the laser power was significantly reduced and its role was partially taken over by the increase in the overlap of the weld depositions. The reason was the different influence of process parameters on the production process, which was described in the first part of the thesis. These changes resulted in a sample relative density of 99.46 % with very good repeatability. Some of the results were published in the Journal of Manufacturing Processes (Elsevier, IF 5.01) and can be summarized as follows:

- A change in the width of a single weld deposition compared to the weld deposition in the volumetric sample has been defined (Fig 6.17). This laid the foundation for optimizing the overlap of weld depositions when designing a strategy for printing volumetric samples.
- A relative density of volumetric samples close to 99.5 % was achieved with very good repeatability (Fig 6.19).

Thanks to the achieved findings, it is possible to formulate an answer to the first scientific question and verify or falsify the proposed hypothesis:

Q1. Magnesium evaporation during the printing process is a natural phenomenon related to the physical properties of magnesium. The biggest problem preventing the achievement of the material with a relative density close to 100 % are the newly formed magnesium vapours, which blur the laser beam and complicate the process. The evaporation process cannot be completely avoided, but it can be limited to a tolerable level.

Low energy density printing is an important factor. With its increasing value, the evaporation becomes more intense. Due to the different weight of the process parameters in the energy equation (5.3), it is necessary to increase its value by increasing the hatch overlap rather than increasing the laser power. The energy delivered to the melting site is then not concentrated in one short peak, which causes intense evaporation.

Since the magnesium alloy printing process will always generate a certain amount of vapour, it is necessary to adjust the inert atmosphere circuit so that it is sufficient to entrain vapours and not allow them to accumulate in the production chamber. This can be partially offset by a post-sample time delay, which will replace the imperfect exhaust during printing, but will significantly prolong the manufacturing process. Hypothesis H1 was thus confirmed.

The second part of the PhD thesis dealt with the corrosion behaviour of 3D printed material with the aim to determine what impact the parameters have on the corrosion rate of the processed material. The corrosion acting on the magnesium alloy was divided into two parts. The first one was related to the behaviour, distribution and size of the cathodic phases within the material, and operated on a galvanic principle. The second one was related to the overall surface of the material; i.e., the surface that could be subject to atmospheric corrosion. From this point of view, the tests were divided into two groups. The first one dealt with the sensitivity of the microstructure of the 3D processed material to the changes in the main process parameters while the second one examined the sensitivity of the surface quality also to the changes in the process parameters.

In the first phase, the microstructure of the 3D printed material was described. The results were related to the microstructure of the cast and extruded material. This helped to reveal the most important differences typical of all three processing methods. The microstructure of the 3D printed material contained very fine grains associated with a high temperature gradient during the printing process. The main component of the microstructure was the α–Mg eutectics and randomly distributed flocculation phases rich in RE elements. Their size was up to 5 μm. Compared to other states, a significantly larger amount of trapped O_2 also appeared in the material, most often in the form of MgO. The reasons for O_2 presence were analysed and explained. No sensitivity of the microstructure to process parameters was observed during the tests. Although their significant change was evident in the microstructure as the boundaries of the paths of laser passes, they did not affect the size or number of intermetallic phases. There was no difference in the hardness test of materials processed with different combinations of process parameters. Some of the results were published in the Journal of Manufacturing Processes (Elsevier, IF 5.01) and Manufacturing Technology (Elsevier, SJR 0.254) and can be summarized as follows:

- The reason for the increased O_2 content in the microstructure of the 3D printed material and the reason for its accumulation in the production chamber during production were explained.
- Low sensitivity of the microstructure to the changes in process parameters

The second phase dealt with the dependence of the surface quality of the material on the change of process parameters. The test was performed on a series of thin-walled samples where the laser power and scanning speed varied. The results plotted in the graph show a significant impact of process parameters on the amount of powder fused to the surface. The obtained results showed the dominant effect of laser power on the production process. The obtained results were summarized in the equation describing the achieved surface roughness Ra for the specified laser power and scanning speed with a coefficient of determination of 97 %. These results were published in the journal Materials (MDPI, IF 3.623) and can be summarized as follows:

- A significant dependence of the surface quality of the magnesium alloy on the change of process parameters, mainly laser power, was found.

- An equation has been defined for estimating the surface roughness depending on the process parameters used (6.1).

The last phase of the work focused on corrosion testing of a 3D printed alloy in a simulated human body environment. The corrosion rates of the alloy were determined for different surface qualities to clarify the effect of surface quality on the resulting corrosion rate. Based on the previous results, it is possible to estimate how the corrosion rate of the processed material changes with a change in the laser power and scanning speed. Compared to the original surface quality ranging between Ra 50–60, its improvement below Ra 40 showed a decrease by ca 30 %. At the same time, the passivation layer was analysed in detail, which provided the basis for explaining the corrosion behaviour of the alloy. The results were published in the Journal of Manufacturing Processes (Elsevier, IF5.01) and can be summarized as follows:

- The corrosion rate for different surface roughness was determined (Fig 6.24).
- The principle of disturbing the passivation layer in connection with the observed corrosion behaviour was explained.

Thanks to the achieved findings, it is possible to formulate an answer to the first scientific question and verify or falsify the proposed hypothesis:

Q2. When an excessive amount of energy density is used, the melt pool begins to widen and affects a wider environment. This leads to the fusion of a larger amount of surrounding powder to the surface of the samples and increases the roughness of their surface. Increasing the laser power contributes significantly to this phenomenon. Conversely, increasing the scanning speed makes the melt pool smaller, which reduces the amount of affected surrounding powder and reduces surface roughness. The results are graphically summarized (Fig 6.23). The corrosion rate of the material is directly proportional to the surface quality. By interpolating the curves from the graph (Fig 6.24) it is possible to predict a change in the corrosion rate for the observed controllable range Ra by a value close to 30 %. The second hypothesis (H2) was also confirmed. It was observed that the better the surface quality achieved, the more effectively it reduced the corrosion rate. However, even with a surface roughness of Ra 0.11 (ground surface), a corrosion rate of 2.11 mm·year^{-1} was achieved and it is still necessary to use post-processing operations such as PEO for biodegradable implants.

The presented PhD thesis focused mainly on the flawless processing of magnesium alloy WE43 and its corrosion behaviour. The reactions of the processed alloy to the changes in the main process and technological parameters were clarified. Furthermore, the higher occurrence of the MgO phase in the 3D printed material compared to conventional processing methods was explained. A different weight of process parameters in the energy equation was proved, the modification of which reduced the amount of vapour produced during printing. The influence of the surface quality on the corrosion rate of the 3D processed material was also proportionally expressed. The corrosion rate of the material was determined for different surface qualities and the way in which the material corrodes was explained in detail.

The topic closely related to the topic of the thesis is a detailed description of the influence of cathodic phases in the microstructure of the material. However, in the thesis, this topic has not been dealt with in detail. The original estimates assumed that the corrosion rate would be reached at the level of the extruded material, which was not confirmed during testing. The difference is probably due to the significantly higher amount of oxygen bound in the 3D printed material in the metastable MgO phase and the distribution of the above - mentioned cathodic phases. Here the author sees an opportunity to build on the submitted PhD thesis.

Articles published in journals with an impact factor

Suchy J, Horynová M, Klakurková L, Palousek D, Koutny D, Celko L. Effect of laser parameters on processing of biodegradable magnesium alloy WE43 via selective laser melting method. Materials (Basel). 2020;13(11).

- *Materials, MPDI – IF 3.623, Q2*

Suchy J, Pantelejev L, Palousek D, Koutny D, Kaiser J. Processing of AlSi9Cu3 alloy by selective laser melting. Powder Metall. 2020;63(3):197–211.

- *Powder Metallurgy, Taylor & Francis – IF 1.911, Q2*

Suchý J, Klakurková L, Man O, Remešová M, Horynová M, Vojtěch D, et al. Corrosion behaviour of WE43 magnesium alloy printed using selective laser melting in simulation body fluid solution. 2021;69(June):556–66.

- *Journal of Manufacturing Processes, Elsevier – IF 5.01, Q2*

Articles published in peer-reviewed journals (WoS or Scopus)

Skřivánková, V.; Vlašic, F.; **Suchý**, J.; Paloušek, D.; Mazal, P. Study of fatigue loading of the SLM and cast material by acoustic emission method. In Metal 2018 - 27th Internation Conference on Metallurgy and Materials, Conference Proceedings. Ostrava-Zabreh: Tanger LTD., 2018. s. 1345-1350. ISBN: 9788087294840.

Krištofová P, Roudnická M, Kubásek J, Paloušek D, **Suchý** J, Vojtěch D. Influence of Production Parameters on the Properties of 3D Printed Magnesium Alloy Mg-4Y-3RE-Zr (WE43). Manuf Technol. 2019 Oct 24;19:613–8.

Krištofová P, Kubásek J, Vojtěch D, Paloušek D, **Suchý** J. Microstructure of the Mg-4Y-3RE-Zr (WE43) magnesium alloy produced by 3D Printing. Manuf Technol [Internet]. 2019;19(1):89–94.

Krištofová P, Roudnická M, Kubásek J, Michalcová A, Vojtěch D, **Suchý** J, et al. Magnesium alloy we43 produced by 3d printing (Slm). Defect Diffus Forum. 2020;405 DDF:345–50.

Krištofová P, Kubásek J, Roudnická M, Michalcová A, **Suchý** J, Paloušek D, et al. Structure and properties of additively manufactured WE43 magnesium alloy. In: 28th International conference on Metallurgy and Materials. Brno; 2019. p. 1578–82.

9 BIBLIOGRAPHY

[1] VAN BAEL, S., Y. C. CHAI, S. TRUSCELLO, M. MOESEN, G. KERCKHOFS, H. VAN OOSTERWYCK, J. P. KRUTH a J. SCHROOTEN. The effect of pore geometry on the in vitro biological behavior of human periosteum-derived cells seeded on selective laser-melted Ti6Al4V bone scaffolds. *Acta Biomaterialia* [online]. 2012, **8**(7), 2824–2834. ISSN 17427061. Dostupné z: doi:10.1016/j.actbio.2012.04.001

[2] BAUMGARTNER, R. Die Osteosynthesen von Lambotte zwischen 1895 und 1907. In: *Geschichte operativer Verfahren an den Bewegungsorganen* [online]. Heidelberg: Steinkopff, 2000, s. 21–29. Dostupné z: doi:10.1007/978-3-642-57709-3_3

[3] SARIS, Nils Erik L., Eero MERVAALA, Heikki KARPPANEN, Jahangir A. KHAWAJA a Andrzei LEWENSTAM. Magnesium: An update on physiological, clinical and analytical aspects. *Clinica Chimica Acta* [online]. 2000, **294**(1–2), 1–26. ISSN 00098981. Dostupné z: doi:10.1016/S0009-8981(99)00258-2

[4] OKUMA, Toshitada. Magnesium and bone strength. *Nutrition* [online]. 2001, **17**(7–8), 679–680. ISSN 08999007. Dostupné z: doi:10.1016/S0899-9007(01)00551-2

[5] HARTWIG, Andrea. Role of magnesium in genomic stability. *Micronutrients and Genomic Stability* [online]. 2001, **475**(1–2), 113–121. ISSN 0027-5107. Dostupné z: doi:10.1016/S0027-5107(01)00074-4

[6] STAIGER, Mark P., Alexis M. PIETAK, Jerawala HUADMAI a George DIAS. Magnesium and its alloys as orthopedic biomaterials: A review. *Biomaterials* [online]. 2006, **27**(9), 1728–1734. ISSN 01429612. Dostupné z: doi:10.1016/j.biomaterials.2005.10.003

[7] REVELL, Peter A., Elsie DAMIEN, X.S. ZHANG, P. EVANS a C. Rolfe HOWLETT. The Effect of Magnesium Ions on Bone Bonding to Hydroxyapatite Coating on Titanium Alloy Implants. *Key Engineering Materials* [online]. 2004, **254–256**, 447–450. ISSN 1662-9795. Dostupné z: doi:10.4028/www.scientific.net/KEM.254-256.447

[8] ZREIQAT, H., C. R. HOWLETT, A. ZANNETTINO, P. EVANS, G. SCHULZE-TANZIL, C. KNABE a M. SHAKIBAEI. Mechanisms of magnesium-stimulated adhesion of osteoblastic cells to commonly used orthopaedic implants. *Journal of Biomedical Materials Research* [online]. 2002, **62**(2), 175–184. ISSN 00219304. Dostupné z: doi:10.1002/jbm.10270

[9] YAMASAKI, Y., Y. YOSHIDA, M. OKAZAKI, A. SHIMAZU, T. KUBO, Y. AKAGAWA a T. UCHIDA. Action of FGMgCO3Ap-collagen composite in promoting bone formation. *Biomaterials* [online]. 2003, **24**(27), 4913–4920. ISSN 01429612. Dostupné z: doi:10.1016/S0142-9612(03)00414-9

[10] LEVOROVA, Jitka, Jaroslava DUSKOVA, Milan DRAHOS, Radka VRBOVA, D VOJTECH, Jiri KUBASEK, Martin BARTOS, Lenka DUGOVA, Dan ULMANN a Rene FOLTAN. In vivo study on biodegradable magnesium alloys: Bone healing around WE43 screws. *Journal of Biomaterials Applications* [online]. 2018, **32**(7), 886–895. ISSN 0885-3282. Dostupné z: doi:10.1177/0885328217743321

[11] MANAKARI, Vyasaraj, Gururaj PARANDE a Manoj GUPTA. *Selective Laser Melting of Magnesium and Magnesium Alloy Powders: A Review* [online]. 2016. ISBN 6565166358. Dostupné z: doi:10.3390/met7010002

[12] SIETSEMA, W. K. Animal models of cortical porosity. *Bone* [online]. 1995, **17**(4 SUPPL.), 297–305. ISSN 87563282. Dostupné z: doi:10.1016/8756-3282(95)00307-Y

[13] ZARDIACKAS, Lyle D., Douglas E. PARSELL, Lance D. DILLON, Darrell W. MITCHELL, Laura A. NUNNERY a Robert POGGIE. Structure, metallurgy, and mechanical properties of a porous tantalum foam. *Journal of Biomedical Materials Research* [online]. 2001, **58**(2), 180–187. ISSN 00219304. Dostupné z: doi:10.1002/1097-4636(2001)58:2<180::AID-JBM1005>3.0.CO;2-5

[14] HOLLISTER, Scott J. Scaffold design and manufacturing: From concept to clinic. *Advanced Materials* [online]. 2009, **21**(32–33), 3330–3342. ISSN 09359648. Dostupné z: doi:10.1002/adma.200802977

[15] HUTMACHER, Dietmar Werner, Jan Thorsten SCHANTZ, Christofer Xu Fu LAM, Kim Cheng TAN a Thiam Chye LIM. State of the art and future directions of scaffold-based bone engineering from a biomaterials perspective. *Journal of Tissue Engineering and Regenerative Medicine* [online]. 2007, **1**(June), 245–260. ISSN 15654753. Dostupné z: doi:10.1002/term

[16] HUTMACHER, Dietmar W. Scaffolds in tissue engineering bone and cartilage. *The Biomaterials: Silver Jubilee Compendium* [online]. 2000, **21**, 2529–2543. Dostupné z: doi:10.1016/B978-008045154-1.50021-6

[17] LEFEBVRE, Louis Philippe, John BANHART a David C. DUNAND. Porous metals and metallic foams: Current status and recent developments. *Advanced Engineering Materials* [online]. 2008, **10**(9), 775–787. ISSN 14381656. Dostupné z: doi:10.1002/adem.200800241

[18] NAKAJIMA, Hideo. Fabrication, properties and application of porous metals with directional pores. *Progress in Materials Science* [online]. 2007, **52**(7), 1091–1173. ISSN 00796425. Dostupné z: doi:10.1016/j.pmatsci.2006.09.001

[19] EVANS, A. G., J. W. HUTCHINSON, N. A. FLECK, M. F. ASHBY a H. N.G. WADLEY. The topological design of multifunctional cellular metals. *Progress in Materials Science* [online]. 2001, **46**(3–4), 309–327. ISSN 00796425. Dostupné z: doi:10.1016/S0079-6425(00)00016-5

[20] ALVAREZ, Kelly a Hideo NAKAJIMA. Metallic scaffolds for bone regeneration. *Materials* [online]. 2009, **2**(3), 790–832. ISSN 19961944. Dostupné z: doi:10.3390/ma2030790

[21] HOLLISTER, Scott J. Porous scaffold design for tissue engineering. *Nature Materials* [online]. 2005, **4**(7), 518–524. ISSN 1476-4660. Dostupné z: doi:10.1038/nmat1421

[22] SACHLOS, E., J. T. CZERNUSZKA, S. GOGOLEWSKI a M. DALBY. Making tissue engineering scaffolds work. Review on the application ofsolid freeform fabrication technology to the production of tissue engineeringscaffolds. *European Cells and Materials* [online]. 2003, **5**, 29–40. ISSN 14732262. Dostupné z: doi:10.22203/eCM.v005a03

[23] RIZA, S.H., S.H. MASOOD a C. WEN. Laser-Assisted Additive Manufacturing for Metallic Biomedical Scaffolds. In: *Comprehensive Materials Processing* [online]. B.m.: Elsevier, 2014 [vid. 2018-05-25], s. 285–301. ISBN 9780080965338. Dostupné z: doi:10.1016/B978-0-08-096532-1.01017-7

[24] YAP, C. Y., C. K. CHUA, Z. L. DONG, Z. H. LIU, D. Q. ZHANG, L. E. LOH a S. L. SING. Review of selective laser melting: Materials and applications. *Applied Physics Reviews* [online]. 2015, **2**(4). ISSN 19319401. Dostupné z: doi:10.1063/1.4935926

[25] GU, D D, W MEINERS, K WISSENBACH a R POPRAWE. Laser additive manufacturing of metallic components: materials, processes and mechanisms. *International Materials Reviews* [online]. 2012, **57**(3), 133–164. ISSN 0950-6608. Dostupné z: doi:10.1179/1743280411Y.0000000014

[26] GUILLEN, Donna P., Janelle P. WHARRY a David W. GANDY. Neutron irradiation of nuclear structural materials fabricated by powder metallurgy with hot isostatic pressing. *Transactions of the American Nuclear Society*. 2017, **116**(June), 392–393. ISSN 0003018X.

[27] YASA, Evren, Jan DECKERS a Jean Pierre KRUTH. The investigation of the influence of laser re-melting on density, surface quality and microstructure of selective laser melting parts. *Rapid Prototyping Journal* [online]. 2011, **17**(5), 312–327. ISSN 13552546. Dostupné z: doi:10.1108/13552541111156450

[28] GU, Dongdong. *Laser Additive Manufacturing of High-Performance Materials* [online]. Berlin, Heidelberg: Springer Berlin Heidelberg, 2015. ISBN 978-3-662-46088-7. Dostupné z: doi:10.1007/978-3-662-46089-4

[29] SUCHY, Jan, Libor PANTELEJEV, David PALOUSEK, Daniel KOUTNY a Jozef KAISER. Processing of AlSi9Cu3 alloy by selective laser melting. *Powder Metallurgy* [online]. 2020, **63**(3), 197–211. ISSN 17432901. Dostupné z: doi:10.1080/00325899.2020.1792675

[30] ZHANG, Baicheng, Hanlin LIAO a Christian CODDET. Effects of processing parameters on properties of selective laser melting Mg–9%Al powder mixture. *Materials & Design* [online]. 2012, **34**, 753–758. ISSN 02613069. Dostupné z: doi:10.1016/j.matdes.2011.06.061

[31] PAWLAK, Andrzej, Maria ROSIENKIEWICZ a Edward CHLEBUS. Design of experiments approach in AZ31 powder selective laser melting process optimization. *Archives of Civil and Mechanical Engineering* [online]. 2017, **17**(1), 9–18. ISSN 16449665. Dostupné z: doi:10.1016/j.acme.2016.07.007

[32] SAVALANI, Monica Mahesh a Jorge Martinez PIZARRO. Effect of preheat and layer thickness on selective laser melting (SLM) of magnesium. *Rapid Prototyping Journal* [online]. 2016, **22**(1), 115–122. ISSN 1355-2546. Dostupné z: doi:10.1108/RPJ-07-2013-0076

[33] TANDON, Rajiv, Todd PALMER, Matthias GIESEKE a Christian NOELKE. Additive Manufacturing of Magnesium Alloy Powders: Investigations Into Process Development Using Elektron®MAP+43 Via Laser Powder Bed Fusion and Directed Energy Deposition. *Euro PM2016*. 2016, **91**, 4–9.

[34] SCHMID, Dominik, Johanna RENZA, Michael F. ZAEH a Johannes GLASSCHROEDER. Process influences on laser-beam melting of the magnesium alloy AZ91. *Physics Procedia* [online]. 2016, **83**, 927–936. ISSN 18753892. Dostupné z: doi:10.1016/j.phpro.2016.08.097

[35] HASMUNI, Noreriyanti, Mustaffa IBRAHIM, Azli Amin RAUS, Md Saidin WAHAB a Khairu KAMARUDIN. Porosity effects of AlSi10mg parts produced by selective laser melting. *Journal of Mechanical Engineering*. 2018, **5**(Specialissue4), 246–255. ISSN 2550164X.

[36] WEI, Kaiwen, Zemin WANG a Xiaoyan ZENG. Influence of element vaporization on formability, composition, microstructure, and mechanical performance of the selective laser melted Mg-Zn-Zr components. *Materials Letters* [online]. 2015, **156**, 187–190. ISSN 18734979. Dostupné z: doi:10.1016/j.matlet.2015.05.074

[37] LOUVIS, Eleftherios, Peter FOX a Christopher J. SUTCLIFFE. Selective laser melting of aluminium components. *Journal of Materials Processing Technology* [online]. 2011, **211**(2), 275–284. ISSN 09240136. Dostupné z: doi:10.1016/j.jmatprotec.2010.09.019

[38] ZUMDICK, Naemi A., Lucas JAUER, Lisa C. KERSTING, Tatiana N. KUTZ, Johannes H. SCHLEIFENBAUM a Daniela ZANDER. Additive manufactured WE43 magnesium: A comparative study of the microstructure and mechanical properties with those of powder extruded and as-cast WE43. *Materials Characterization* [online]. 2019, **147**(August 2018), 384–397. ISSN 10445803. Dostupné z: doi:10.1016/j.matchar.2018.11.011

[39] SAVALANI, M.M., L. HAO, P.M. DICKENS, Y. ZHANG, K.E. TANNER a R.A. HARRIS. The effects and interactions of fabrication parameters on the properties of selective laser sintered hydroxyapatite polyamide composite biomaterials. *Rapid Prototyping Journal* [online]. 2012, **18**(1), 16–27. ISSN 1355-2546. Dostupné z: doi:10.1108/13552541211193467

[40] NG, C. C., M. M. SAVALANI, H. C. MAN a I. GIBSON. Layer manufacturing of magnesium and its alloy structures for future applications. *Virtual and Physical Prototyping* [online]. 2010, **5**(1), 13–19. ISSN 17452759. Dostupné z: doi:10.1080/17452751003718629

[41] CHUNG NG, Chi, Monica SAVALANI a Hau CHUNG MAN. Fabrication of magnesium using selective laser melting technique. *Rapid Prototyping Journal* [online]. 2011, **17**(6), 479–490. ISSN 1355-2546. Dostupné z: doi:10.1108/13552541111184206

[42] NG, C. C., M. M. SAVALANI, M. L. LAU a H. C. MAN. Microstructure and mechanical properties of selective laser melted magnesium. *Applied Surface Science* [online]. 2011, **257**(17), 7447–7454. ISSN 01694332. Dostupné z: doi:10.1016/j.apsusc.2011.03.004

[43] HU, Dong, Yong WANG, Dingfei ZHANG, Liang HAO, Junjie JIANG, Zhonghua LI a Yitao CHEN. Experimental Investigation on Selective Laser Melting of Bulk Net-Shape Pure Magnesium. *Materials and Manufacturing Processes* [online]. 2015, **30**(11), 1298–1304. ISSN 15322475. Dostupné z: doi:10.1080/10426914.2015.1025963

[44] WEI, Kaiwen, Ming GAO, Zemin WANG a Xiaoyan ZENG. Effect of energy input on formability, microstructure and mechanical properties of selective laser melted AZ91D magnesium alloy. *Materials Science and Engineering A* [online]. 2014, **611**, 212–222. ISSN 09215093. Dostupné z: doi:10.1016/j.msea.2014.05.092

[45] JAUER, Lucas, Wilhelm MEINERS, Simon VERVOORT, Christoph GAYER, Naemi A. ZUMDICK a Daniela ZANDER. Selective laser melting of magnesium alloys. In: *World PM 2016 Congress and Exhibition*. B.m.: European Powder Metallurgy Association (EPMA), 2016. ISBN 9781899072484.

[46] BÄR, Florian, Leopold BERGER, Lucas JAUER, Güven KURTULDU, Robin SCHÄUBLIN, Johannes H. SCHLEIFENBAUM a Jörg F. LÖFFLER. Laser additive manufacturing of biodegradable magnesium alloy WE43: A detailed microstructure analysis. *Acta Biomaterialia* [online]. 2019, (xxxx). ISSN 18787568. Dostupné z: doi:10.1016/j.actbio.2019.05.056

[47] ESMAILY, M., Z. ZENG, A. N. MORTAZAVI, A. GULLINO, S. CHOUDHARY, T. DERRA, F. BENN, F. D'ELIA, M. MÜTHER, S. THOMAS, A. HUANG, A. ALLANORE, A. KOPP a N. BIRBILIS. A detailed microstructural and corrosion analysis of magnesium alloy WE43 manufactured by selective laser melting. *Additive Manufacturing* [online]. 2020, **35**(April), 101321. ISSN 22148604. Dostupné z: doi:10.1016/j.addma.2020.101321

[48] HYER, Holden, Le ZHOU, George BENSON, Brandon MCWILLIAMS, Kyu CHO a Yongho SOHN. Additive Manufacturing of Dense WE43 Mg Alloy by Laser Powder Bed Fusion. *Additive Manufacturing* [online]. 2020, **33**(February), 101123. ISSN 22148604. Dostupné z: doi:10.1016/j.addma.2020.101123

[49] ALCOCK, C B, V P ITKIN a M K HORRIGAN. Vapour Pressure Equations for the Metallic Elements: 298–2500K. *Canadian Metallurgical Quarterly* [online]. 1984, **23**(3), 309–313. ISSN 0008-4433. Dostupné z: doi:10.1179/cmq.1984.23.3.309

[50] IHSAN, Barin. Thermochemical data of pure substances. *and*. 1995, **934**, 587.

[51] GHALI, Edward, Wolfgang DIETZEL a Karl Ulrich KAINER. Testing of general and localized corrosion of magnesium alloys: A critical review. *Journal of Materials Engineering and Performance* [online]. 2004, **13**(5), 517–529. ISSN 10599495. Dostupné z: doi:10.1361/10599490420665

[52] SONG, Guang Ling a Andrej ATRENS. Corrosion mechanisms of magnesium alloys. *Advanced Engineering Materials* [online]. 1999, **1**(1), 11–33. ISSN 14381656. Dostupné z: doi:10.1002/(SICI)1527-2648(199909)1:1<11::AID-ADEM11>3.0.CO;2-N

[53] GUSIEVA, K., C. H. J. DAVIES, J. R. SCULLY a N. BIRBILIS. Corrosion of magnesium alloys: the role of alloying. *International Materials Reviews* [online]. 2015, **60**(3), 169–194. ISSN 0950-6608. Dostupné z: doi:10.1179/1743280414Y.0000000046

[54] LI, X P, K M O DONNELL a T B SERCOMBE. Selective laser melting of Al-12Si alloy : Enhanced densification via powder drying [online]. 2016, **10**, 10–14. Dostupné z: doi:10.1016/j.addma.2016.01.003

[55] POLMEAR, I J, IJP a I J POLMEAR. Light Alloys. In: I J POLMEAR, ed. *Light Alloys (Fourth Edition)* [online]. Fourth Edi. Oxford: Butterworth-Heinemann, 2005, s. 413. ISBN 978-0-7506-6371-7. Dostupné z: doi:https://doi.org/10.1016/B978-075066371-7/50006-2

[56] SÜDHOLZ, A. D., N. T. KIRKLAND, R. G. BUCHHEIT a N. BIRBILIS. Electrochemical Properties of Intermetallic Phases and Common Impurity Elements in Magnesium Alloys. *Electrochemical and Solid-State Letters* [online]. 2011, **14**(2), C5. ISSN 10990062. Dostupné z: doi:10.1149/1.3523229

[57] RALSTON, K. D., G. WILLIAMS a N. BIRBILIS. Effect of pH on the Grain Size Dependence of Magnesium Corrosion. *CORROSION* [online]. 2012, **68**(6), 507–517. ISSN 0010-9312. Dostupné z: doi:10.5006/i0010-9312-68-6-507

[58] AVEDESIAN, M. M. a Hugh. BAKER. *Magnesium and magnesium alloys*. Ohio: USA: ASM Internationa, 1999. ISBN 0871706571.

[59] SINGH, Ashish a Sandip P. HARIMKAR. Laser surface engineering of magnesium alloys: A review. *Jom* [online]. 2012, **64**(6), 716–733. ISSN 10474838. Dostupné z: doi:10.1007/s11837-012-0340-2

[60] GUAN, Y. C., W. ZHOU, H. Y. ZHENG a Z. L. LI. Solidification microstructure of AZ91D Mg alloy after laser surface melting. *Applied Physics A: Materials Science and Processing* [online]. 2010, **101**(2), 339–344. ISSN 09478396. Dostupné z: doi:10.1007/s00339-010-5880-0

[61] LIU, Cancan, Qingbiao LI, Jun LIANG, Jiansong ZHOU a Lingqian WANG. Microstructure and corrosion behaviour of laser surface melting treated WE43 magnesium alloy. *RSC Adv.* [online]. 2016, **6**(36), 30642–30651. ISSN 2046-2069. Dostupné z: doi:10.1039/C5RA27010C

[62] CZERWINSKI, F. The oxidation behaviour of an AZ91D magnesium alloy at high temperatures [online]. 2002, **50**, 2639–2654. Dostupné z: https://www.sciencedirect.com/science/article/pii/S1359645402000940

[63] DREIZIN, Edward L., Charles H. BERMAN a Edward P. VICENZI. Condensed-phase modifications in magnesium particle combustion in air. *Combustion and Flame* [online]. 2000, **122**(1–2), 30–42. ISSN 00102180. Dostupné z: doi:10.1016/S0010-2180(00)00101-2

[64] PRASAD, Arvind, Zhiming SHI a Andrej ATRENS. Influence of Al and Y on the ignition and flammability of Mg alloys. *Corrosion Science* [online]. 2012, **55**, 153–163. ISSN 0010938X. Dostupné z: doi:10.1016/j.corsci.2011.10.014

[65] SALEHI, Mojtaba, Saeed MALEKSAEEDI, Hamidreza FARNOUSH, Mui Ling Sharon NAI, Ganesh Kumar MEENASHISUNDARAM a Manoj GUPTA. An investigation into interaction between magnesium powder and Ar gas: Implications for selective laser melting of magnesium. *Powder Technology* [online]. 2018, **333**, 252–261. ISSN 1873328X. Dostupné z: doi:10.1016/j.powtec.2018.04.026

[66] ZONG, Fujian, Chunzhan MENG, Zhiming GUO, Feng JI, Hongdi XIAO, Xijian ZHANG, Jin MA a Honglei MA. Synthesis and characterization of magnesium nitride powder formed by Mg direct reaction with N2. *Journal of Alloys and Compounds* [online]. 2010, **508**(1), 172–176. ISSN 09258388. Dostupné z: doi:10.1016/j.jallcom.2010.07.224

[67] ABEL, Arvid, Yvonne WESSARGES, Stefan JULMI, Christian HOFF, Jörg HERMSDORF, Christian KLOSE, Hans Jürgen MAIER, Stefan KAIERLE a Ludger OVERMEYER. Laser powder bed fusion of WE43 in hydrogen-argon-gas atmosphere. *Procedia CIRP* [online]. 2020, **94**, 21–24. ISSN 22128271. Dostupné z: doi:10.1016/j.procir.2020.09.005

[68] LI, Y., J. ZHOU, P. PAVANRAM, M. A. LEEFLANG, L. I. FOCKAERT, B. POURAN, N. TÜMER, K. U. SCHRÖDER, J. M.C. MOL, H. WEINANS, H. JAHR a A. A. ZADPOOR. Additively manufactured biodegradable porous magnesium. *Acta Biomaterialia* [online]. 2018, **67**, 378–392. ISSN 18787568. Dostupné z: doi:10.1016/j.actbio.2017.12.008

[69] KOPP, Alexander, Thomas DERRA, Max MÜTHER, Lucas JAUER, Johannes H. SCHLEIFENBAUM, Maximilian VOSHAGE, Ole JUNG, Ralf SMEETS a Nadja KRÖGER. Influence of design and postprocessing parameters on the degradation behavior and mechanical properties of additively manufactured magnesium scaffolds. *Acta Biomaterialia* [online]. 2019, (xxxx). ISSN 18787568. Dostupné z: doi:10.1016/j.actbio.2019.04.012

[70] SUDHOLZ, A. D., K. GUSIEVA, X. B. CHEN, B. C. MUDDLE, M. A. GIBSON a N. BIRBILIS. Electrochemical behaviour and corrosion of Mg-Y alloys. *Corrosion Science* [online]. 2011, **53**(6), 2277–2282. ISSN 0010938X. Dostupné z: doi:10.1016/j.corsci.2011.03.010

[71] DAVENPORT, Alison J., Cristiano PADOVANI, Brian J. CONNOLLY, Nicholas P.C. STEVENS, Thomas A.W. BEALE, Amela GROSO a Marco STAMPANONI. Synchrotron X-ray microtomography study of the role of y in corrosion of magnesium alloy WE43. *Electrochemical and Solid-State Letters* [online]. 2007, **10**(2), 4–8. ISSN 10990062. Dostupné z: doi:10.1149/1.2400727

[72] WANG, X. M., X. Q. ZENG, G. S. WU a S. S. YAO. Yttrium ion implantation on the surface properties of magnesium. *Applied Surface Science* [online]. 2006, **253**(5), 2437–2442. ISSN 01694332. Dostupné z: doi:10.1016/j.apsusc.2006.04.066

[73] WANG, X.M., X.Q. ZENG, G.S. WU, S.S. YAO a L.B. LI. Surface oxidation behavior of MgNd alloys. *Applied Surface Science* [online]. 2007, **253**(22), 9017–9023. ISSN 01694332. Dostupné z: doi:10.1016/j.apsusc.2007.05.023

[74] JAUER, L, B JÜLICH, M VOSHAGE a W MEINERS. Selective Laser Melting of magnesium alloys. 2015, **30**(page 1), 824682.

[75] GANGIREDDY, Sindhura, Bharat GWALANI, Kaimiao LIU, Eric J. FAIERSON a Rajiv S. MISHRA. Microstructure and mechanical behavior of an additive manufactured (AM) WE43-Mg alloy. *Additive Manufacturing* [online]. 2019, **26**(September 2018), 53–64. ISSN 22148604. Dostupné z: doi:10.1016/j.addma.2018.12.015

[76] LI, Y, J ZHOU, P PAVANRAM, M A LEEFLANG, L I FOCKAERT, B POURAN, N TÜMER, K SCHRÖDER, J M C MOL, H WEINANS, H JAHR a A A ZADPOOR. Additively manufactured biodegradable porous magnesium. *Acta Biomaterialia* [online]. 2018, **67**, 378–392. Dostupné z: doi:10.1016/j.actbio.2017.12.008

[77] SCIPIONI BERTOLI, Umberto, Alexander J. WOLFER, Manyalibo J. MATTHEWS, Jean Pierre R. DELPLANQUE a Julie M. SCHOENUNG. On the limitations of Volumetric Energy Density as a design parameter for Selective Laser Melting. *Materials and Design* [online]. 2017, **113**, 331–340. ISSN 18734197. Dostupné z: doi:10.1016/j.matdes.2016.10.037

[78] SONG, Guangling, Andrej ATRENS a David STJOHN. An Hydrogen Evolution Method for the Estimation of the Corrosion Rate of Magnesium Alloys. In: *Essential Readings in Magnesium Technology* [online]. Cham: Springer International Publishing, 2016, s. 565–572. Dostupné z: doi:10.1007/978-3-319-48099-2_90

[79] SONG, G.-L. Corrosion behavior and prevention strategies for magnesium (Mg) alloys. In: *Corrosion Prevention of Magnesium Alloys* [online]. B.m.: Elsevier, 2013, s. 3–37. Dostupné z: doi:10.1533/9780857098962.1.3

[80] ATRENS, Andrej, Guang Ling SONG, Ming LIU, Zhiming SHI, Fuyong CAO a Matthew S. DARGUSCH. Review of recent developments in the field of magnesium corrosion. *Advanced Engineering Materials* [online]. 2015, **17**(4), 400–453. ISSN 15272648. Dostupné z: doi:10.1002/adem.201400434

[81] GUO, Yueling, Lina JIA, Bin KONG, Na WANG a Hu ZHANG. Single track and single layer formation in selective laser melting of niobium solid solution alloy. *Chinese Journal of Aeronautics* [online]. 2018, **31**(4), 860–866. ISSN 10009361. Dostupné z: doi:10.1016/j.cja.2017.08.019

[82] KEMPEN, K., W. Verheecke L. THIJS , E. YASA, M. BADROSSAMAY a Department J.-P. KRUTH. Process Optimization and Microstructural Analysis for Selective Laser Melting of AlSi10Mg. In: . 2011, s. 484–495.

[83] LI, Ruidi, Jinhui LIU, Yusheng SHI, Li WANG a Wei JIANG. Balling behavior of stainless steel and nickel powder during selective laser melting process. *International Journal of Advanced Manufacturing Technology* [online]. 2012, **59**(9–12), 1025–1035. ISSN 02683768. Dostupné z: doi:10.1007/s00170-011-3566-1

[84] CZERWINSKI, Frank. Controlling the ignition and flammability of magnesium for aerospace applications. *Corrosion Science* [online]. 2014, **86**, 1–16. ISSN 0010938X. Dostupné z: doi:10.1016/j.corsci.2014.04.047

[85] TEKUMALLA, Sravya a Manoj GUPTA. An insight into ignition factors and mechanisms of magnesium based materials: A review. *Materials and Design* [online]. 2017, **113**, 84–98. ISSN 18734197. Dostupné z: doi:10.1016/j.matdes.2016.09.103

[86] ZHAN, Xiaohong, Jicheng CHEN, Junjie LIU, Yanhong WEI, Junjie ZHOU a Yao MENG. Microstructure and magnesium burning loss behavior of AA6061 electron beam welding joints. *Materials and Design* [online]. 2016, **99**, 449–458. ISSN 18734197. Dostupné z: doi:10.1016/j.matdes.2016.03.058

[87] SERCOMBE, T B, X LI, T B SERCOMBE a X LI. Selective laser melting of aluminium and aluminium metal matrix composites : review Selective laser melting of aluminium and aluminium metal matrix composites : review [online]. 2016, **7857**. Dostupné z: doi:10.1080/10667857.2016.1161147

[88] NAHMANY, Moshe, Idan ROSENTHAL, Isgav BENISHTI, Nachum FRAGE a Adin STERN. Electron beam welding of AlSi10Mg workpieces produced by selected laser melting additive manufacturing technology. *Additive Manufacturing* [online]. 2015, **8**, 63–70. ISSN 22148604. Dostupné z: doi:10.1016/j.addma.2015.08.002

[89] SUCHY, Jan, Miroslava HORYNOVÁ, Lenka KLAKURKOVÁ, David PALOUSEK, Daniel KOUTNY a Ladislav CELKO. Effect of laser parameters on processing of biodegradable magnesium alloy WE43 via selective laser melting method. *Materials* [online]. 2020, **13**(11). ISSN 19961944. Dostupné z: doi:10.3390/ma13112623

[90] KRÓL, M. a T. TASKI. Surface quality research for selective laser melting of TI-6AL-4V alloy. *Archives of Metallurgy and Materials* [online]. 2016, **61**(3), 945–950. ISSN 17333490. Dostupné z: doi:10.1515/amm-2016-0213

[91] TAHERI, M. a J. R. KISH. Nature of Surface Film Formed on Mg Exposed to 1 M NaOH. *Journal of The Electrochemical Society* [online]. 2013, **160**(1), C36–C41. ISSN 0013-4651. Dostupné z: doi:10.1149/2.018302jes

[92] LI, Zijian, Xunan GU, Siquan LOU a Yufeng ZHENG. The development of binary Mg-Ca alloys for use as biodegradable materials within bone. *Biomaterials* [online]. 2008, **29**(10), 1329–1344. ISSN 01429612. Dostupné z: doi:10.1016/j.biomaterials.2007.12.021

[93] DING, Wenjiang. Opportunities and challenges for the biodegradable magnesium alloys as next-generation biomaterials. *Regenerative Biomaterials* [online]. 2016, **3**(2), 79–86. ISSN 20563426. Dostupné z: doi:10.1093/RB/RBW003

10 LIST OF FIGURES AND TABLES

List of figures

Fig 1.1 Comparison of basic mechanical properties of bone implants designed by additive manufacturing with the structure of real bones. 14

Fig 2.1 (a) Metal powder atomization scheme [26] and (b) SLM method scheme [27]. .. 16

Fig 2.2 (a) Process window diagram with designation of processable and (b) definition of main process parameters [35]. 18

Fig 2.3 (a) Identification of the minimum amount of energy density for the formation of weld deposits from pure Mg and (b) the effect of energy density on the saturation of the surface of the weld deposit with oxygen [41]... 19

Fig 2.4 Volumetric samples of pure magnesium using powders with a distribution of (a) 26 µm and (b) 43 µm [43]... 20

Fig 2.5 Process map diagram for printing volumetric samples from Mg-9% Al alloy [30]. 21

Fig 2.6 Porous microstructure in material (a) and dependence of sample hardness on energy density (b) [30]. 21

Fig 2.7 Process map describing the behaviour of AZ91D alloy depending on the energy density [44]. 22

Fig 2.8 Influence of laser power and scanning speed on the shape of weld depositions made of AZ91D alloy [34]... 23

Fig 2.9 Surface of the volumetric sample produced by gradually increasing the overlap of the weld tracks [34]. 23

Fig 2.10 Recording of vapours during the AZ91D alloy printing process: (a) without modification of the inert atmosphere circuit; (b) with a modified inert atmosphere circuit [45].. 24

Fig 2.11 Comparison of the use of conventional production strategy (a) and remelting of layers (b) [33]. 25

Fig 2.12 Recording of the tensile test at room temperature: (a) the entire course of the test; (b) detail of the transition from yield strength to ultimate strength; and (c) scheme of formation of superheated areas in the sample contour [38]. 25

Fig 2.13 EBSD map of the last solidified layer of material around the melt pool [46]. 26

Fig 2.14 Vapor pressure (a) and Ellingham diagram (b) for the main alloying elements of WE43 alloy [49, 50]. 27

Fig 2.15 (a) Pourbaix diagram for Mg (H_2O_3, 25 °C) [59] and (b) effect of additive elements on Mg corrosion in 3 % NaCl solution [58]. 29

Fig 2.16 (a) Influence of ambient temperature on the corrosion rate of AZ91magnesium alloys and (b) detail of the first hour of test [62]. 30

Fig 2.17 (a) Lattice structures exposed to the corrosion solution for 28 days and records of hydrogen release (b) and concentrations of selected elements in the solution during the corrosion test (c) [68]. 32

Fig 2.18 Comparison of the produced lattice structure before chemical etching (a) and after its application (b) [69]. 33

Fig 2.19 Hydrogen evolved during a corrosion test in a salt solution lasting 24 hours for different types of samples [47]. 34

Fig 5.1 Powder distribution for 3D printing (a) and SEM photographs of particle shape (b). 52

Fig 5.2 Scheme for determining the depth of the weld deposition from the metallographic cut (a) and a record of the measurement of the width and height of the weld deposition by the profilometer (b). In the upper left corner, see the build plate with inserted slices for printing the weld depositions. 54

Fig 5.3 Example of scanned region and its evaluation (a) with ContourGT-X measuring device (b). 55

Fig 5.4 Measurement of local chemical composition using EDS (a) and setting of measuring apparatus for EBSD method (b). 55

Fig 5.5 Development of defects in the material depending on the change of process parameters: (a) temperature cracks caused by a high temperature gradient; (b) porosity in the material caused by trapping superheated gas particles; (c) a sample with a relative density of 99.8 %.. 57

Fig 5.6 HSBF (b) Schematic representation of the capture of released hydrogen during the immersion test (a) and HSBF chemical composition table (b). 58

Fig 6.1 WE43 magnesium alloy process window diagram based on the behaviour of weld deposition tracks. 60

Fig 6.2 Dependence of the width of the weld depositions on the change of laser power and scanning speed. 60

Fig 6.3 Key-hole porosity at the root of the weld deposition and smaller spherical pores along the weld deposition boundary (Lp 200 W, Ls 100 mm·s^{-1}) (a) and unstable weld deposition (Lp 125 W, Ls 150 150 mm·s^{-1}) caused by melt spraying and its subsequent solidification. 61

Fig 6.4 Example of measurement of microhardness of weld depositions with highlighted weld deposition boundary (a) and plotted dependence of average value of microhardness on selected process parameters. 62

Fig 6.5 Internal structure of the weld deposition (Lp = 325 W, Ls = 650 mm·s^{-1}): (a) macro view and (b) agglomeration detail in the upper left corner of the sample. 63

Fig 6.6 Development of the difference in the width of thin walls and weld depositions depending on the laser power and selected scanning speeds: Ls 450 mm·s^{-1} (a) and Ls 750 mm·s^{-1} (b). 64

Fig 6.7 Macrostructural studies of selected samples containing a number of defects (8 – Lp=250 W, Ls=450 mm·s^{-1}, Hd=80 μm; 13 – Lp=250 W, Ls=700 mm·s^{-1}, Hd=80 μm; 36 – Lp=275 W, Ls=450 mm·s^{-1}, Hd=90 μm; 41 – Lp=275 W, Ls=700 mm·s^{-1}, Hd=90 μm). . 65

Fig 6.8 Record of compression test measurements of 3D printed material WE43. 66

Fig 6.9 SEM images of WE43 magnesium alloy cuts: (a) cast state; (b) extruded state; (c, d) 3D printed state. 67

Fig 6.10 EDS microstructure mapping of 3D printed WE43. 68

Fig 6.11 SEM images of WE43 material cuts: (a) in cast state and (b, c) in 3D printed state. 69

Fig 6.12 Record of WE43 behaviour under mechanical loading: (a) in compression and (b) in three-point bending. 70

Fig 6.13 Deposition of evaporated powder on the protective glass of the laser when printing a large number of samples. 70

Fig 6.14 The original single-stage filtration system housed in the machine space (a) and a modified variant of the two-stage filtration system with a more powerful pump and process emissions extraction from the upper part of the production chamber (b). 71

Fig 6.15 Scheme of inert atmosphere flow and rolling of magnesium vapours (a) and process emissions extraction by diffuser (b). 72

Fig 6.16 Porosity distribution in the sample (Lp = 250 W; Ls = 450 mm·s^{-1}; Hd = 90 μm) after modification of the inert atmosphere circuit. 73

Fig 6.17 Development of weld deposition width depending on laser power and scanning speed: (a) in thin-walled and (b) volumetric samples. 73

Fig 6.18 Porosity in the structure of the samples in the plane perpendicular to the build plate (X–Z): 74

Fig 6.19 Dependence of relative sample density on laser power and scanning speed. 74

Fig 6.20 EDS description of the microstructure of WE43 alloy in the direction perpendicular to the build plate. The as-built sample was tested before the immersion test: (a) overview; (b, c) detail (SEM-BSE); (d–h) EDS mapping of the selected region. 76

Fig 6.21 IPF map: (a) direction of powder application and (b) normal direction............ 77

Fig 6.22 Example of selected properties of material grains: (a) grain size and (b) circularity and highlighting of grain boundaries. 77

Fig 6.23 Arithmetic dependence of the surface depending on: (a) laser power, (b) scanning speed. 78

Fig 6.24 Corrosion rate of WE43 magnesium alloy in HBSS at 37 °C calculated from hydrogen released during testing for: (a) 168 h and (b) 7 h. The curves were obtained as the average of three measurements. 79

Fig 6.25 X-ray diffraction field: (a) As-built sample before corrosion test and (b–d) As-built sample after corrosion testing in HBSS. 80

Fig 6.26 Appearance of as-built sample after immersion corrosion test in HBSS: (a-c) sample morphology; (d-f) cross section of the sample and (g) table of local chemical composition. 80

Fig 7.1 Crystal lattices of oxides and their melting points (T): (a) Al2O3, T=2 072 °C; (b) Y2O3, T=2 425 °C; (c) MgO, T=2 852 °C. 82

Seznam tabulek

Tab 3.1 Overview of the ranges of process parameters used. 39

Tab 6.1 Summary of results from initial measurements of hardness and compressive strength of volumetric samples. 66

Tab 6.2 Chemical composition (wt.%) of selected areas from Fig 6.10. 68

Tab 6.3 Comparison of selected mechanical properties of WE43 alloy in cast and 3D printed state. 70

11 LIST OF SYMBOLS AND UNITS

A	mm^2	Total sample area
CAD		Computer Aided Design
D	$g \cdot mm^{-3}$	Density of alloy WE43
E	$J \cdot mm^{-3}$	Energy density
EBM		Electron Beam Melting
EBSD		Electron Backscatter Diffraction
EDS		Energy dispersive spectroscopy
E_l	$J \cdot mm^{-2}$	Linear Energy Density
E_v	$J \cdot mm^{-2}$	Volume Energy Density
H_2	ml	Amount of Hydrogen released
H_d	µm	Hatch Distance
HIP		Heat Isostatic Pressing
HV		Vickers Hardness
ICP-OES		Inductively Coupled Plasma Optical Emission Spectrometry
i_g	$mm \cdot year^{-1}$	Corrosion Rate
L_p	W	Laser Power
L_s	$mm \cdot s^{-1}$	Laser Scanning speed
L_t	µm	Layer Thickness
Mr_{H2}	$g \cdot mol^{-1}$	Molar Weight of Hydrogen
Mr_{Mg}	$g \cdot mol^{-1}$	Molar Weight of Magnesium
PEO		Plasma Electrolytic Oxidation
Ra	µm	Surface Roughness
RE		Rare Earth Elements
SEM		Scanning Electron Microscope
SLM		Selective Laser Melting
t	year	Time of exposure
XRD		X-Ray Diffraction
YRL		Ytterbium Fiber Laser